**Title**
Fast and efficient transducers for microwave-optical quantum communication

**Author**
Peairs, Gregory

**Publication Date**
2019

UNIVERSITY of CALIFORNIA
Santa Barbara

# Fast and efficient transducers for microwave-optical quantum communication

A dissertation submitted in partial satisfaction of the
requirements for the degree of

Doctor of Philosophy

in

Physics

by

Gregory Alexander Peairs

Committee in charge:

Professor Andrew N. Cleland, Chair

Professor David M. Weld

Professor Chetan Nayak

September 2019

The dissertation of Gregory Alexander Peairs is approved.

Professor David M. Weld

Professor Chetan Nayak

Professor Andrew N. Cleland, Chair

August 2019

# Acknowledgements

This work was made possible with the contributions of many people along the way, to whom I am deeply grateful. I foremost want to thank my advisor, Andrew Cleland, for his expertise and guidance, as well as the challenge and opportunity of building the lab and group back up after moving to Chicago.

My years at UCSB and in Chicago would not have been the same without Kevin Satzinger—your company on this journey has meant a great deal to me.

Amit Vainsencher and Joerg Bochmann welcomed us into the lab and laid the foundation for future generations of electro-optomechanical transducers. I owe them much insight, technical and otherwise. Amit also visited us in Chicago to assemble an optical setup, which was invaluable in keeping the experiment moving forward.

In Chicago, we were joined by a new cohort of highly capable students. Ming-Han Chou and Rhys Povey became my comrades in optomechanics. Before long, Ming-Han picked up the reins on our demanding fabrication process, dedicating many hours in the PNF and at Argonne to the devices described in this thesis. Rhys has taken on his own ambitious project, and I hope to reflect his insight and thoroughness in my work. More recently, Chris Conner has set his sights on a quantum transducer. I have great confidence in the three of you.

My time and work in Chicago has also felt the presence of Youpeng Zhong, Hung-Shen Chang, and Joel Grebel, all of whom it has been a pleasure to work beside. Youpeng set up the electronics for our lab's qubit experiments, which we adapted for our time-domain measurements, with advice also from Hung-Shen; Joel has been infinitely reliable in assistance of all kinds. And our wonderful Chicago postdocs, Étienne Dumur and Audrey Bienfait, have always been able to find the right questions. I thank them for many fruitful discussions, and am excited to see them making traveling-wave quantum acoustics happen.

Finally, I want to express my appreciation for the many people beyond our lab, at UCSB, UChicago, and elsewhere, who have shaped my path for the better, and to offer special thanks to my teachers, family, and friends who prepared me for this experience and shared a piece of theirs with me.

# Curriculum Vitæ

Gregory Alexander Peairs

## Education

| | |
|---|---|
| 2019 | Ph.D., Physics, University of California, Santa Barbara |
| 2012 | B.S., Honors with Distinction, Physics, Stanford University |

## Professional Experience

| | |
|---|---|
| 2015–2019 | Visiting graduate student researcher, Institute for Molecular Engineering, University of Chicago |
| 2012–2015 | Graduate student researcher, Department of Physics, University of California, Santa Barbara |
| 2011–2012 | Research assistant, Physics, Stanford University |
| 2011–2012 | Teaching assistant, Physics, Stanford University |

## Selected Publications

"Efficient continuous and time-domain transduction between microwave and optical frequencies," Gregory A. Peairs et al. (in preparation)

"Unidirectional distributed acoustic wave transducers for quantum applications," É. Dumur, K. J. Satzinger, G. A. Peairs, M.-H. Chou, A. Bienfait, H.-S. Chang, C. R. Conner, J. Grebel, R. G. Povey, Y. P. Zhong, A. N. Cleland, *Applied Physics Letters* 114, 223501 (2019)

"Quantum control of surface acoustic-wave phonons," K. J. Satzinger, Y. P. Zhong, H.-S. Chang, G. A. Peairs, A. Bienfait, M.-H. Chou, A. Y. Cleland, C. R. Conner, É. Dumur, J. Grebel, I. Gutierrez, B. H. November, R. G. Povey, S. J. Whiteley, D. D. Awschalom, D. I. Schuster, A. N. Cleland, *Nature* 563, 661–665 (2018)

"Bi-directional conversion between microwave and optical frequencies in a piezoelectric optomechanical device," A. Vainsencher, K. J. Satzinger, G. A. Peairs, A. N. Cleland, *Applied Physics Letters* 109, 033107 (2016)

# Abstract

### Fast and efficient transducers for microwave-optical quantum communication

by

Gregory Alexander Peairs

A quantum network consisting of computational nodes connected by high-fidelity communication channels could expand information-processing capabilities beyond those of classical networks. Superconducting qubits hold promise for scalable quantum computation at microwave frequencies, but must operate in an isolated cryogenic environment; meanwhile, quantum communication over long distances has been demonstrated with optical photons. A fast, quantum-coherent interface between the two would be a key element of a large-scale quantum network or distributed quantum computer.

In this thesis, we describe the theoretical basis as well as the practical design and development of a device incorporating a silicon optomechanical nanobeam and an aluminum-nitride-based electromechanical transducer. We find that this class of device has the potential to approach ideal quantum microwave-optical transduction. Finally, we experimentally demonstrate classical, continuous-wave operation of such a device with external conversion efficiencies of $\eta_{\text{ext}} = (2.5 \pm 0.4) \times 10^{-5}$ (microwave to optical) and $\eta_{\text{ext}} = (3.8 \pm 0.4) \times 10^{-5}$ (optical to microwave), corresponding to internal efficiencies of 2.4% and 3.75%. This device also has a larger bandwidth than previous efficient

microwave-optical transducers, allowing us to operate in the time domain with 20 ns pulses.

# Contents

# Chapter 1

# Quantum information processing

The work described in this thesis is directed toward the efficient and quantum-coherent conversion of signals between microwave and optical frequencies. The chief motivation for building such a device is in its potential for scaling up a quantum computer or network by allowing quantum information to be shared between distant nodes.

Systems that require quantum mechanical descriptions—ranging from those provided by nature like individual atoms or ions to engineered systems like quantum dots or superconducting circuits—can be used for information-processing tasks like computation and communication. While classical computers encode information as separable “bits” taking on values of 0 or 1, a quantum two-state system or “qubit” can be in a superposition of its two states and quantum-mechanically entangled with any number of other qubits. Taking advantage of the rules of quantum mechanics may offer an expansion of information processing capabilities over what is practically possible with classical computers.

For example, researchers have found quantum algorithms that have better asymptotic scaling properties than the known classical algorithms for a number of problems, including the factoring of large numbers and simulation of quantum systems. A sufficiently large quantum computer could efficiently solve instances of these problems that are large enough to be effectively intractable to known classical algorithms.

## 1.1 Superconducting qubits

Experiments so far have only demonstrated quantum control and readout of a small number of qubits. Scaling those experiments to a many-qubit fault-tolerant computer remains a challenge. Among other candidates, superconducting quantum circuits have attracted interest as a potentially scalable platform for quantum information processing [62]. Superconducting qubits operate at microwave frequencies, with $|0\rangle$ and $|1\rangle$ states separated by a typical energy difference around $h \times 6\,\mathrm{GHz}$, where $h$ is the Planck constant and $hf$ is the energy of a single field quantum (a photon, for electromagnetic fields) at frequency $f$. To prevent errors due to thermal fluctuations in the environment driving the transition from $|0\rangle$ to $|1\rangle$, devices at this frequency must be operated at temperatures $T \ll hf/k_B \approx 300\,\mathrm{mK}$, where the Boltzmann constant $k_B$ relates the temperature to the energy in microscopic degrees of freedom at that temperature. In practice, a dilution refrigerator is used to cool these systems to below $10\,\mathrm{mK}$.

Superconducting qubits on the same chip can be tunably coupled using superconducting circuit elements. Communication between remote qubits (for example, at different ends of a microwave cable or long on-chip transmission line) has also been demonstrated, with recently achieved benchmarks for quantum communication including deterministic bidirectional single-photon transfer and entanglement generation [33], as well as Bell-inequality violation [68]. Coupling qubits in separate refrigerators presents further difficulties, since a microwave communication channel at room temperature will be noisy, with thermal fluctuations overwhelming a single-photon signal.

## 1.2 Quantum networks

Quantum communication channels may have applications in cryptography, perhaps most famously in quantum key distribution, as well as in distributed quantum computation. In the latter, remote quantum processors would share an entangled state, effectively creating a larger quantum computer than the largest modular quantum processor possible at a given stage of development [30]. It would accordingly be valuable to combine a qubit platform suitable for scalable computation with a long-distance communication channel.

Transmitting quantum information over long distances is a challenge, as quantum states are vulnerable to loss in transmission or disturbance by the environment. While there exist protocols for quantum error correction or purification, these require a minimum fidelity as a starting point.

Optical photons are better suited than microwave photons for long-distance quantum communication, since the energy carried by an optical photon is much greater than that of thermal fluctuations in a room-temperature environment. For example, at the

1550 nm telecommunications wavelength ($f \approx 193\,\mathrm{THz}$, near-infrared), the energy of a photon is $hf \approx k_B(9000\,\mathrm{K})$. Modern telecommunications technologies, including lasers and optical fiber, are also well developed. Experiments have demonstrated quantum teleportation (a fundamental building block of quantum communication protocols) of information encoded in optical photons over distances up to 1400 km in free-space ground-to-satellite communication [44], and 100 km in optical fiber [56].

Extending quantum communication beyond that scale becomes more difficult, as even small but unavoidable transmission losses mount. Classical networks can reach arbitrary distances using repeaters positioned throughout the network. These devices receive a signal and re-transmit it, amplifying and correcting the signal to account for loss or errors accumulated in transmission. The classical approach cannot be directly extended to quantum signals. For example, error correction by simply measuring redundant copies of the quantum state locally and then reconstructing the result would destroy any entanglement with the source node. More broadly, the quantum no-cloning theorem forbids the amplification of arbitrary quantum states without some disturbance [65].

A quantum repeater protocol could be used to overcome this limitation [10]. It would be desirable to implement a repeater using qubits suitable for computation, with fast, high-fidelity operation scalable to hundreds of qubits. In this sense superconducting qubits may be attractive for this purpose. A quantum repeater does, however, also require efficient coupling of traveling photons to the qubits of the repeater node. The prospect of using superconducting qubits as a platform for quantum repeaters thus further motivates the development of a quantum microwave-optical transducer [40].

## 1.3 Microwave-optical transduction

An ideal quantum microwave-optical transducer would coherently and bidirectionally exchange one microwave photon for one photon in the optical signal. The extra energy of up- or down-conversion would come from an optical "pump" or "carrier" tone (that is, for up-conversion, the energy of the microwave photon is added to a carrier photon to create a signal photon). This exchange would also ideally be performed without adding noise to the quantum state, requiring cryogenic operation to freeze out microwave thermal noise.

Classical radio- and microwave-frequency signals are routinely transmitted over an optical carrier in research and communications applications. This can be accomplished, for example, with phase modulation of the carrier by the signal, typically using the electro-optic effect in a crystal like lithium niobate, resulting in optical sidebands separated from the carrier by the signal frequency.

That is, given an optical input amplitude $\alpha_0 e^{-2\pi i f_c t}$ (with power $|\alpha_0|^2$) at carrier frequency $f_c$, modulated at microwave frequency $f_m$ with modulation depth $M$, phase modulation produces the output field

$$\begin{aligned}\alpha(t) &= \alpha_0 e^{-2\pi i f_c t} e^{-iM sin(2\pi f_m t)} \\ &= \sum_{n=-\infty}^{\infty} \alpha_0 J_n(M) e^{-2\pi i (f_c + n f_m) t} \qquad (1.1)\end{aligned}$$

expanded in Bessel functions of the first kind $J_n$. For weak modulation ($M \ll 1$), the carrier is not depleted ($J_0(M) \approx 1$), and the higher-order sidebands ($|n| > 1$) can be ignored.

On the simplest level, something like the commercial broadband electro-optic modulator we use in our lab would be far too inefficient for quantum transduction, and cannot practically be used for optical-to-microwave conversion at all.[1] Typically the efficiency of electro-optic modulation in a phase modulator is described indirectly using the half-wave voltage $V_\pi$, defined such that the electro-optic phase shift due to a voltage $V(t)$ is $\Delta\phi = \pi V(t)/V_\pi$. It is a useful exercise to convert this to a ratio of average output sideband photon rate to average input microwave photon rate, since this is the sort of calculation underlying the efficiencies computed later in this thesis.

For a microwave input power $P_{\text{in}} = V_{\text{rms}}^2/Z_0$ with $V_{\text{rms}} \ll V_\pi$ incident on the electro-optic modulator (impedance matched to $Z_0 = 50\,\Omega$), we can calculate the output power in the optical sidebands

$$\begin{aligned} P_{\text{sb}} &= 2\left|\alpha_0 J_1(M)\right|^2 = 2\left|\alpha_0\right|^2 \left|J_1(\pi\sqrt{2}V_{\text{rms}}/V_\pi)\right|^2 \\ &\approx 2\left|\alpha_0\right|^2 \left|\frac{1}{2}\pi\sqrt{2}V_{\text{rms}}/V_\pi\right|^2 \\ &= \left|\alpha_0\right|^2 \left(\frac{\pi V_{\text{rms}}}{V_\pi}\right)^2. \end{aligned} \tag{1.2}$$

The respective microwave and optical average photon rates are $P_{\text{in}}/hf_m$ and $P_{\text{sb}}/hf_c$.

---

[1] Meanwhile, a classical microwave-frequency signal can be recovered from an optical carrier and sideband using a high-speed amplified photodetector with bandwidth sufficient to see the beat between the sideband and carrier, but this will not preserve quantum coherence.

Then the efficiency is

$$\frac{P_{\mathrm{sb}} f_m}{P_{\mathrm{in}} f_c} = \frac{f_m \left|\alpha_0\right|^2 \pi^2 Z_0}{f_c V_\pi^2}. \tag{1.3}$$

For our microwave frequency $f_m = 5\,\mathrm{GHz}$, near-infrared carrier frequency $f_c = 193\,\mathrm{THz}$, and a typical $V_\pi = 5\,\mathrm{V}$, this is $\left|\alpha_0\right|^2 / 2\,\mathrm{kW}$. That is, (incorrectly) extrapolating the linear performance implies that kilowatts of carrier power would be required to reach unit photon efficiency (and this power would instead destroy the device first). In a cryogenic environment, peak power could be limited to microwatts in order to prevent heating (particularly in the vicinity of superconducting electrodes), giving efficiency of order $10^{-9}$. Quantum transduction seems to require a different approach.

## 1.4 Towards quantum transduction

One possibility is to enhance the electro-optic interaction by using resonant optical and electrical modes. This is the approach taken by Fan et al. [18], where two optical modes of an aluminum nitride ring resonator are matched to the electric field of a capacitor in a microwave-frequency superconducting inductor-capacitor ($LC$) resonator. The authors achieve a total bidirectional efficiency of 2.05% (internal efficiency 25.9%). The experiment uses relatively high optical pump powers, with over $3 \times 10^7$ photons in the pump mode, and requires the device be immersed in superfluid helium to promote thermalization to the cryogenic environment [55].

Another approach is to create a common interface between the two frequencies with some third component. The system demonstrated in Ref. [1] uses a mechanically compliant membrane for this purpose. One portion of the membrane couples to an $LC$ resonator, while another couples to a resonance of an optical mirror cavity. Vibrational motion involving the entire membrane thus couples the microwave and optical electromagnetic modes. One potential drawback is that the mechanical resonance used is around 1 MHz, meaning that even if the membrane is thermalized to a 10 mK cryogenic environment, there will be substantial thermal mechanical motion adding noise to the transduction process; the conversion bandwidth will also be limited by the relatively low mechanical frequency. In Ref. [24], such a system was operated with 47% conversion efficiency and 12 kHz bandwidth, also demonstrating the reduction of added noise by a feed-forward protocol.

Meanwhile, optomechanical crystal devices (Fig. 1.1) provide an on-chip platform for coupling optics to microwave-frequency mechanical modes [50]. Devices made from silicon have been operated in the quantum regime [46, 47, 37, 26] and with very high mechanical quality factor corresponding to phonon lifetime above 1 second [35]. If an electromechanical element is included in such a device, a path can be created between optical and microwave-frequency electromagnetic signals. The use of microwave-frequency mechanics is particularly attractive for quantum transduction, as the mechanical resonator will be near its quantum ground state in a cryogenic environment. Transduction can also be performed with a relatively high bandwidth, which is relevant for fast operation with

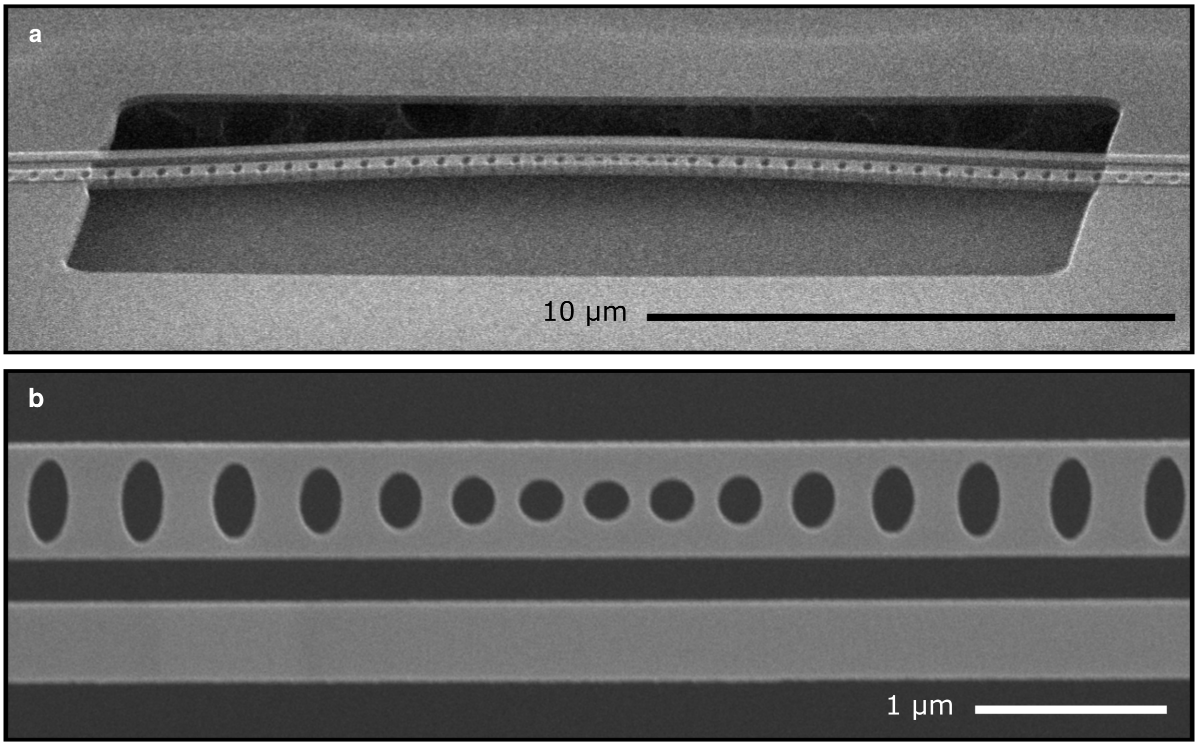

Figure 1.1: **Silicon optomechanical nanobeam and coupling waveguide.** Optomechanical crystal devices are described in Chapter 3. **a,** Angled scanning electron micrograph showing mechanical release of nanobeam from the substrate. **b,** Optomechanical "defect" at the center of the nanobeam.

superconducting qubits that may have lifetimes in the tens of microseconds [62].

Silicon does not provide a convenient means for strong electromechanical coupling. Other work has used gallium arsenide, which is optically similar to silicon while also exhibiting a piezoelectric effect, for electro-optomechanical transduction from microwaves to optics [6, 5], most recently demonstrating conversion with less than one thermal phonon in the mechanical resonator [19]. The work described in this thesis instead uses aluminum nitride, which has a considerably stronger piezoelectric effect and can be deposited in a thin film, allowing it to be used together with silicon optomechanics.

In a predecessor to the experiment described in Chapter 5, unidirectional microwave-to-optical transduction was demonstrated using an optomechanical nanobeam fabricated in thin-film aluminum nitride [8]. The mechanics were driven electrically using the piezoelectric effect in aluminum nitride, with electrodes patterned on the top and bottom surfaces of the nanobeam some distance from the optomechanical resonator. This allowed phase-sensitive optical readout of coherent excitations of the mechanical mode near the level of a single phonon.

For a subsequent experiment building on those results, we developed a design and fabrication process for an interdigital acoustic-wave transducer on an aluminum nitride membrane (Fig. 1.2). This allowed mode matching of the acoustic wave coupled out of the nanobeam in the experiment described in Ref. [57], which demonstrated bidirectional conversion of signals between microwave and optical frequencies with external amplitude scattering matrix elements $S_{oe,\mathrm{ext}} = (1.4 \pm 0.6) \times 10^{-4}$ (electrical to optical) and $S_{eo,\mathrm{ext}} = (3.0 \pm 0.9) \times 10^{-4}$ (optical to electrical). In the terminology of this thesis, these are on-chip photon efficiencies $\eta_{\mathrm{GHz}\to\mathrm{opt}} = 1.4 \times 10^{-7}$ and $\eta_{\mathrm{opt}\to\mathrm{GHz}} = 6.6 \times 10^{-7}$ (the squares of the scattering matrix elements, where the 13.8% grating-coupler efficiency for getting light on and off chip has been divided out; see Chapter 2).

A major factor limiting performance in the above experiment was the achievable optomechanical coupling strength in an aluminum-nitride device. Silicon exhibits a much stronger photoelastic effect. Combining a silicon optomechanical platform with an aluminum-nitride-based electromechanical element (Fig. 1.3), together with revisiting

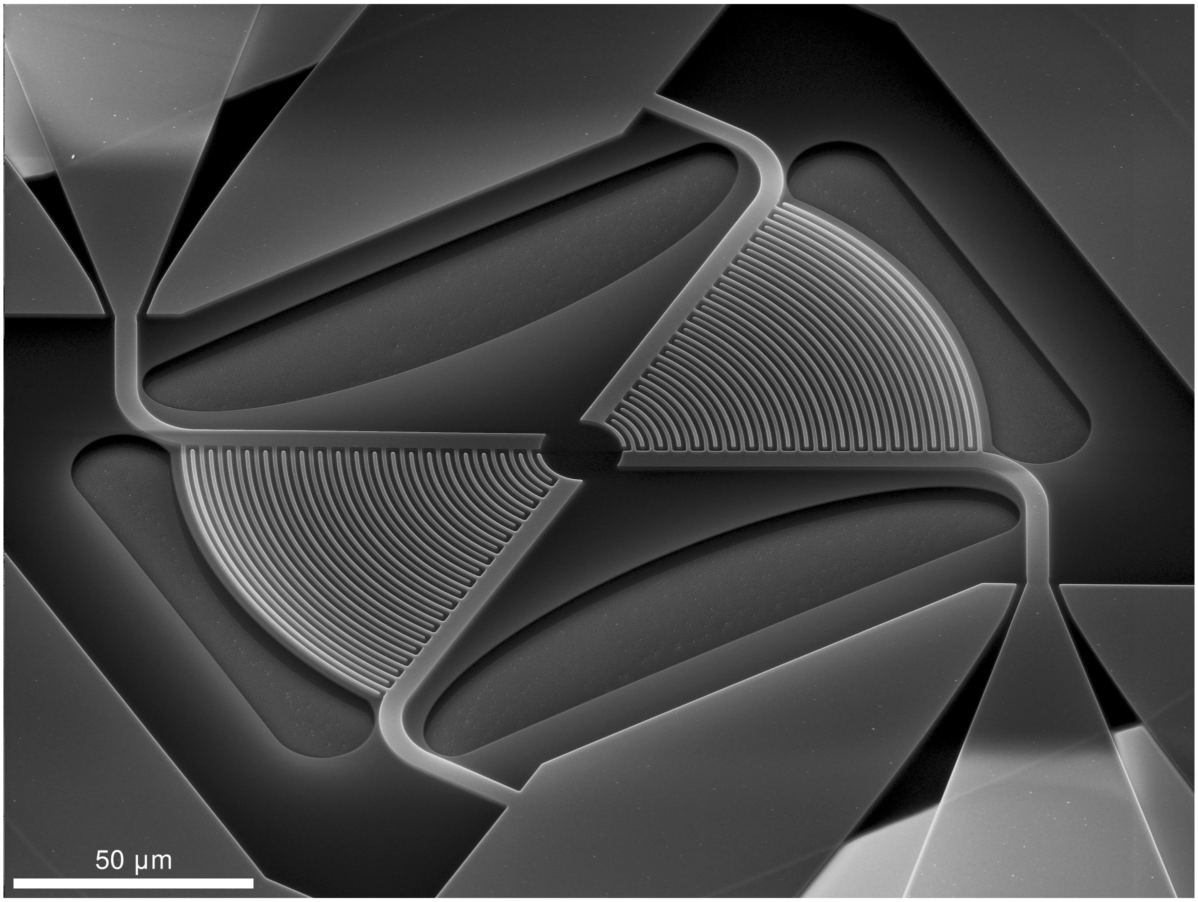

Figure 1.2: **Membrane acoustic wave transducer.** This device, which uses interdigital electrodes to excite and detect resonant acoustic waves on a piezoelectric aluminum nitride (AlN) membrane, was part of the development of an all-AlN electro-optomechanical transducer [57]. Membrane acoustic wave devices are described in Chapter 4.

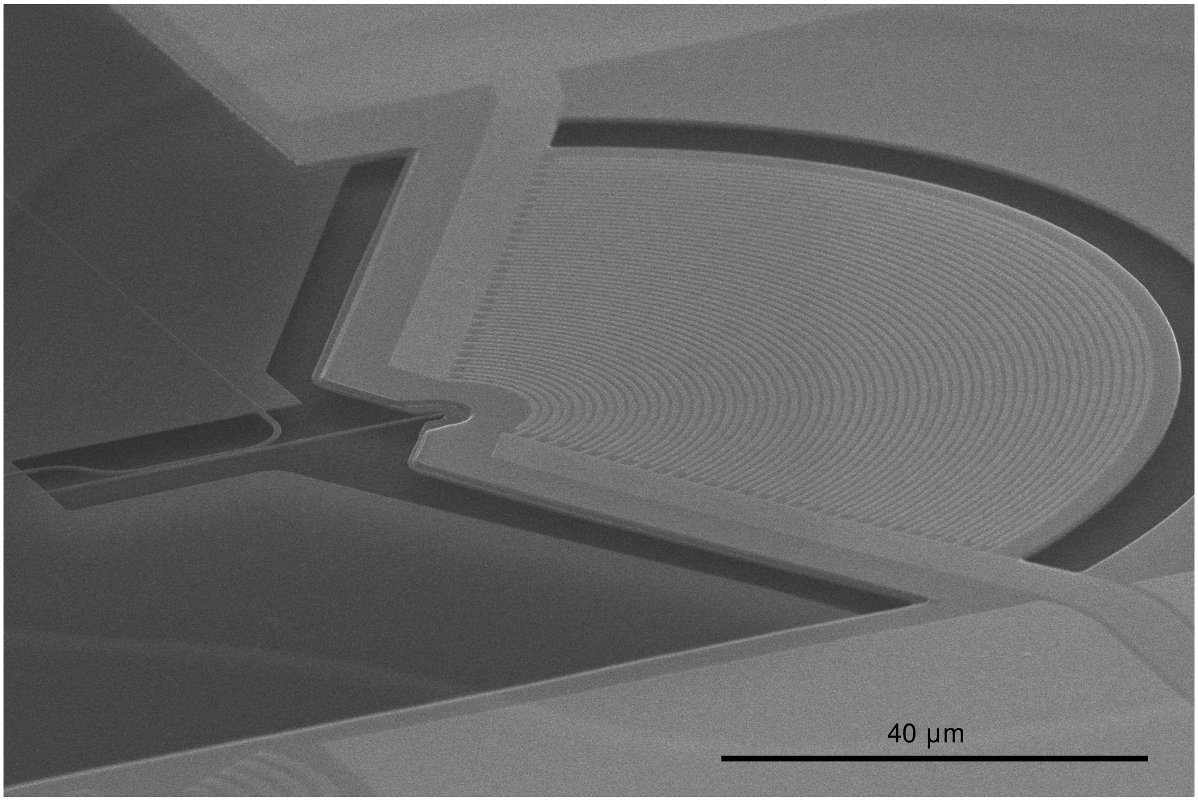

Figure 1.3: **Electro-optomechanical transducer.** A silicon optomechanical nanobeam is connected to an acoustic wave transducer on a piezoelectric bilayer membrane. Experimental results using this device are described in Chapter 5.

and optimizing each part of the design, has the potential to enable transduction with near unit efficiency. In the following chapters, we present a theoretical model for such a device, the design and analysis of the optomechanical and electromechanical components, and the experimental results of continuous and time-domain operation of the device.

# Chapter 2

# Theory of electro-optomechanical transduction

In this chapter we build up a model of a hybrid electromechanical-optomechanical system. The system consists of a mechanical mode coupled to both a microwave-frequency electromechanical mode and an optical mode, allowing transfer of electromagnetic signals between microwave and optical frequencies.

Similar three-mode models of state transfer are described in Refs. [1, 24] and [66]. In all of these the electromechanical mode is replaced by a microwave-frequency *LC* resonator, while the mechanical mode is considered as a single mode with two loci, each coupled to either the microwave or optical mode. In the first pair of experiments, the mechanical mode is at a lower frequency and the microwave-mechanical coupling is an optomechanical coupling.[1] In the device proposed in the third reference, there is really

---

[1] For fixed microwave pump strength, when red detuned and sideband resolved, this system approx-

a pair of hybridized mechanical-electromechanical modes, as in our device, but only one is considered. The microwave and mechanical modes are also assumed to be frequency matched, and the analysis is performed with an equivalent circuit model. Finally, Wang and Clerk [61, 60] theoretically describe transfer protocols in three-mode systems using time-domain control of both couplings, taking advantage of mechanically dark modes to optimize transfer in the presence of strong mechanical dissipation.

We first present the standard optomechanical Hamiltonian before adding in the electromechanical mode, after which we discuss transduction efficiency, bandwidth, and added noise in the three-mode system.

## 2.1 Optomechanics

A number of diverse systems exhibit interactions between electromagnetic fields and mechanical motion. A review of cavity optomechanics can be found in Ref. [3].

The basic optomechanical Hamiltonian describes an optical mode whose frequency is modulated by the displacement of a mechanical mode. Writing the optical annihilation operator $\hat{a}$ and mechanical displacement $\hat{x} = x_{\mathrm{zpf}}(\hat{b} + \hat{b}^\dagger)$ (with zero point displacement

---

imately reproduces our Hamiltonian of Eqn. 2.12 below, but the low-frequency mechanical mode leads to significant differences in operating bandwidth and added noise; see §2.3.1 and §2.4 below.

$x_{\mathrm{zpf}})^2$ the Hamiltonian is

$$\hat{H}_{\mathrm{om}} = \hbar\hat{a}^\dagger\hat{a}\left(\omega(\hat{x})\right) + \hbar\Omega_{\mathrm{m}}\hat{b}^\dagger\hat{b}. \tag{2.1}$$

with optical and mechanical frequencies $\omega(\hat{x})$ and $\Omega_{\mathrm{m}}$.

The classic example is an optical cavity with one fixed mirror and one mirror on a spring (considering only one cavity mode and one vibrational mode). The optical resonance frequency is inversely proportional to the cavity length $L + \hat{x}$ and can be expanded as a function of $\hat{x}$:

$$\omega(\hat{x}) = \omega_{\mathrm{opt}}\left(1 - \frac{\hat{x}}{L} + \cdots\right). \tag{2.2}$$

Then the optomechanical Hamiltonian is

$$\hat{H}_{\mathrm{om}} = \hbar\hat{a}^\dagger\hat{a}\left(\omega_{\mathrm{opt}} + g_0(\hat{b} + \hat{b}^\dagger)\right) + \hbar\Omega_{\mathrm{m}}\hat{b}^\dagger\hat{b}, \tag{2.3}$$

where we have identified $-\omega_{\mathrm{opt}}x_{\mathrm{zpf}}/L$ as the "single-photon" (or sometimes "vacuum") optomechanical coupling $g_0$, so called because the energy shift is $\hbar g_0$ per photon in the cavity at the mechanical zero-point fluctuation amplitude.

---

[2] The zero point displacement is the amplitude of displacement fluctuations in the mechanical ground state, meaning $m\Omega_{\mathrm{m}}^2 x_{\mathrm{zpf}}^2/2 = p_{\mathrm{zpf}}^2/2m = \hbar\Omega_{\mathrm{m}}/4$, or $x_{\mathrm{zpf}} = \sqrt{\hbar/2m\Omega_{\mathrm{m}}}$, for a mode with effective mass $m$. For modes where the physical displacement is a spatially varying vector $\mathbf{u}$, we can parameterize it as $\mathbf{u} = x\mathbf{q}$. By convention we choose the scalar $x$ to describe some characteristic displacement, typically evaluated at the spatial maximum of $|\mathbf{u}|$. Then the potential energy $m\Omega_{\mathrm{m}}^2 x^2/2$ of the parameterized oscillator can be related to the actual strain potential energy associated with $\mathbf{u}$, fixing $m$, after which $x_{\mathrm{zpf}}$ can be calculated.

The optomechanical nanobeam devices discussed in this thesis are described by this mirror-on-a-spring Hamiltonian with coupling linear in $\hat{x}$. In other systems, it is possible to obtain a coupling where the quadratic term dominates in the expansion of $\omega(\hat{x})$; this is known as "membrane-in-the-middle" optomechanics, since it arises when a vibrational mode of a membrane interacts with two cavity modes on either side, causing zero variation in optical energy to first order in displacement.

We are interested in the system when driven (or "pumped") with a laser at frequency $\omega_L$. It is convenient to switch to the frame rotating at $\omega_L$, and define $\Delta \equiv \omega_{\mathrm{opt}} - \omega_L \ll \omega_{\mathrm{opt}}$ as the frequency of the cavity mode in that frame. Note that $\Delta > 0$ corresponds to a pump that is red-detuned (that is, at a lower or "redder" frequency than the cavity). Then the Hamiltonian becomes

$$\hat{H}_{\mathrm{om}} \approx \hbar\Delta\hat{a}^\dagger\hat{a} + \hbar\Omega_{\mathrm{m}}\hat{b}^\dagger\hat{b} + \hbar g_0\left(\hat{a}^\dagger\hat{a}\right)\left(\hat{b} + \hat{b}^\dagger\right) \tag{2.4}$$

Here we have made the rotating wave approximation, dropping terms rotating at $\omega_L + \omega_{\mathrm{opt}}$, since dynamics on that timescale average to zero on the timescales of interest.

We can write the optical cavity field as a small fluctuation around a mean coherent amplitude $\alpha$:

$$\hat{a} = \alpha + \delta\hat{a}. \tag{2.5}$$

This allows us to "linearize" the optomechanical interaction as[3]

$$\hat{H}_{\text{int,om}} \approx \hbar g_0 \left(\alpha^* \delta\hat{a} + \alpha \delta\hat{a}^\dagger\right)(\hat{b} + \hat{b}^\dagger). \tag{2.6}$$

We can also identify the "driven" or "pumped" optomechanical coupling $G_{\text{om}} \equiv \alpha g_0$, observing that the effective coupling strength can be controlled by modulating the pump strength.

With a pump red detuned by the mechanical frequency, the $\delta\hat{a}^\dagger\hat{b}$ and $\delta\hat{a}\hat{b}^\dagger$ terms are resonant (describing energy-conserving processes that would survive another rotating wave approximation), respectively denoting the destruction of a phonon for the creation of a cavity photon from the pump and the reverse process. These processes can be used for state transfer or cooling of the mechanical mode. For a blue detuned pump, the resonant terms involve $\delta\hat{a}^\dagger\hat{b}^\dagger$ and $\delta\hat{a}\hat{b}$ (the simultaneous creation or destruction of one photon and one phonon) which describe two-mode squeezing or mechanical self-amplification.

### 2.1.1 Origin of the optomechanical coupling

The optomechanical coupling in our devices arises from a combination of the photoelastic effect and the moving dielectric boundary seen by the optical mode.[4] The optical fre-

---

[3] Here and elsewhere in this thesis, we ignore terms in the Hamiltonian like an additional $|\alpha|^2 \hbar g_0(\hat{b}+\hat{b}^\dagger)$ from displacement coupling to the constant coherent amplitude of the optical mode; this amounts to a small shift in the equilibrium displacement and does not affect the dynamics, allowing us to slightly redefine $\hat{x}$ to eliminate that term. Likewise for the much smaller coupling to the zero-point energy of the optical mode, which could have been included in Eqn. 2.1. The linearization also ignores the terms quadratic in $\delta\hat{a}$, which has been assumed to be small.

[4] For another perspective on optomechanical coupling, see the literature on stimulated Brillouin scattering (SBS), which deals with traveling waves rather than localized cavity modes [17]. The coupling is usually described as originating from electrostriction and radiation pressure—that is, the respective

quency shifts due to these effects can be derived using perturbation theory; this discussion follows Refs. [27, 28, 11].

The photoelastic effect describes the modulation of the optical permittivity $\varepsilon$ by mechanical strain $\mathbf{S}$, using the photoelastic tensor $p_{ijkl}$ to write the change in permittivity

$$(\varepsilon(\mathbf{S}) - \varepsilon(0))_{ij} = -\frac{1}{\varepsilon_0}\varepsilon_{ik}p_{klmn}S_{mn}\varepsilon_{lj}, \tag{2.7}$$

summing over repeated indices.

This gives rise to the optomechanical coupling

$$\hbar g_{0,\mathrm{pe}} = \frac{1}{4}\int \mathrm{d}V\, \frac{1}{\varepsilon_0}E_i^*\varepsilon_{ik}p_{klmn}S_{mn}\varepsilon_{lj}E_j. \tag{2.8}$$

Here the strain field $\mathbf{S}$ is normalized to its zero-point amplitude (see Footnote 2), the electric field $\mathbf{E}$ is normalized to its single-photon amplitude (such that the time-averaged electric and magnetic field energy are each $\hbar\omega_{\mathrm{opt}}/2$), and the integral is over the mechanical solid volume. The coupling has been written as an energy, with normalization absorbed into the fields, to highlight the connection with the Hamiltonian.

For silicon, we have the isotropic index of refraction $n = \sqrt{\varepsilon_{11}/\varepsilon_0}$ and three independent photoelastic coefficients $p_{11} \equiv p_{1111}$, $p_{12} \equiv p_{1122}$, and $p_{44} \equiv p_{1212}$ given cubic

---

backactions of our photoelastic and moving boundary effects, now from the perspective of the optical field acting on the mechanics. (Though also be aware that elsewhere, reported coefficients for electrostriction are usually for the quadratic mechanical response to electric fields not optically but at microwave or lower frequency.) The two perspectives have recently converged, particularly with the development of nanophotonic SBS devices. A useful bridge between them is provided by Ref. [59]. A recent tutorial on the subject, with COMSOL model files hosted in a data repository, is provided by Ref. [63].

symmetry [67]. The product can be written out as[5]

$$\begin{aligned}\hbar g_{0,\mathrm{pe}} = \frac{\varepsilon_0 n^4}{4}\int_{\mathrm{Si}} \mathrm{d}V \Big( & |E_1|^2 \left(p_{11}S_{11} + p_{12}(S_{22}+S_{33})\right) \\ & + |E_2|^2 \left(p_{11}S_{22} + p_{12}(S_{11}+S_{33})\right) \\ & + |E_3|^2 \left(p_{11}S_{33} + p_{12}(S_{11}+S_{22})\right) \\ & + 4\mathrm{Re}[E_1E_2]p_{44}S_{12} \\ & + 4\mathrm{Re}[E_1E_3]p_{44}S_{13} \\ & + 4\mathrm{Re}[E_2E_3]p_{44}S_{23}\Big). \end{aligned} \tag{2.9}$$

The mechanical displacement also causes a change in the dielectric seen by the optical field at the boundaries of the mechanical resonator. To ensure we only deal with field components that are continuous across the boundary (and hence well defined on the boundary), we split the field into components parallel and perpendicular to the boundary, and define $\Delta\varepsilon = \varepsilon_1 - \varepsilon_2$ and $\Delta\varepsilon^{-1} = \varepsilon_1^{-1} - \varepsilon_2^{-1}$ as well as the unit surface normal $\hat{\mathbf{n}}$ pointing from the material with permittivity $\varepsilon_1$ to the material with $\varepsilon_2$. Then we can write the moving-boundary optomechanical coupling

$$\hbar g_{0,\mathrm{mb}} = -\frac{1}{4}\int \mathrm{d}A\, \mathbf{u}\cdot\hat{\mathbf{n}} \left(\Delta\varepsilon \left|\mathbf{E}_{\parallel}\right|^2 - \Delta\varepsilon^{-1}\left|\mathbf{D}_{\perp}\right|^2\right). \tag{2.10}$$

---

[5] The factor of 4 in the $p_{44}$ terms can be obtained by using Voigt notation and keeping careful track of the covariant and contravariant representations (see Ref. [23]), or by simply counting identical terms when summing over all indices for the original tensor product: $E_1^* p_{1212} S_{12} E_2 + E_2^* p_{2112} S_{12} E_1 = E_1^* p_{1221} S_{21} E_2 + E_2^* p_{2121} S_{21} E_1 = 2\mathrm{Re}[E_1E_2]p_{1212}S_{12}$ and so on. Since these terms are typically small, the correct multiplicity may be overlooked (and appears to have been overlooked in some references including Refs. [11, 12]). I thank Rhys Povey for pointing this out.

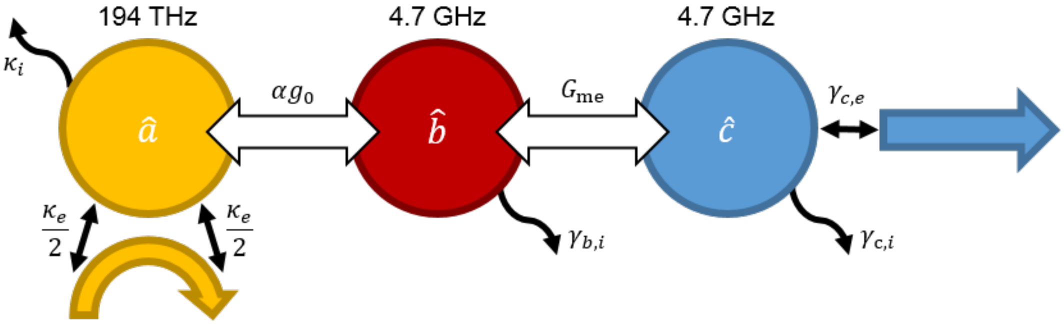

Figure 2.1: **Schematic representation of coupled optical, mechanical, and electromechanical modes.** The optical mode is shown with external coupling to both propagating directions in an evanescently coupled waveguide.

Again, the mechanical displacement and electric fields are normalized to give one half phonon and one photon of total energy in the respective modes. The integral is over the surface of the mechanical solid.

## 2.2 Electro-optomechanics

The electro-optomechanical model consists of the following modes and couplings, illustrated in Fig. 2.1:

- An optical mode with annihilation operator $\hat{a}$ at frequency $\omega_{\mathrm{opt}}$, with intrinsic loss rate $\kappa_i$ and extrinsic loss $\kappa_e/2$ to each of two propagation directions in an adjacent waveguide[6]
- A microwave-frequency mechanical mode $\hat{b}$ at $\Omega_{\mathrm{m}}$ with intrinsic loss rate $\gamma_{b,i}$

---

[6] This is sometimes called "two-sided coupling" in the text. This is meant in contrast to "one-sided" coupling, in which the optical mode emits into only one propagation direction at the end of a waveguide and must be probed in reflection. Because only one direction of propagation is used for sending and receiving signals, two-sided coupling generally results in the loss of half of the signal, but allows transmission measurements.

- A microwave-frequency electromechanical mode $\hat{c}$ at $\Omega_{\text{em}}$ (near $\Omega_{\text{m}}$) with intrinsic loss rate $\gamma_{c,i}$, and external coupling $\gamma_{c,e}$ to a microwave transmission line
- Single-photon optomechanical coupling $g_0$ between modes $\hat{a}$ and $\hat{b}$
- Fixed coupling $G_{\text{me}}$ between the mechanical and electromechanical modes $\hat{b}$ and $\hat{c}$, described by $\hat{H}_{\text{me}} = \hbar G_{\text{me}}(\hat{b}\hat{c}^\dagger + \hat{b}^\dagger \hat{c})$ to first order in the respective fields, keeping energy-conserving terms.

We also define total loss rates for ease of notation:

$$\kappa = \kappa_i + \kappa_e, \qquad \gamma_c = \gamma_{c,i} + \gamma_{c,e}. \tag{2.11}$$

We perform the same rotating-wave approximation and linearization of the optomechanical Hamiltonian as in Eqns. 2.3–2.6. Then the driven electro-optomechanical Hamiltonian can be written

$$\begin{aligned} \hat{H}_{\text{eom}} = {} & \hbar\Delta\hat{a}^\dagger\hat{a} + \hbar\Omega_{\text{m}}\hat{b}^\dagger\hat{b} + \hbar\Omega_{\text{em}}\hat{c}^\dagger\hat{c} + \hbar g_0\left(\alpha^*\hat{a} + \alpha\hat{a}^\dagger\right)(\hat{b} + \hat{b}^\dagger) \\ & + \hbar G_{\text{me}}(\hat{b}\hat{c}^\dagger + \hat{b}^\dagger\hat{c}) + \hat{H}_{\text{env}}. \end{aligned} \tag{2.12}$$

Here we include $\hat{H}_{\text{env}}$ to describe linear coupling to any bath or drive fields.[7] We also relabel $\delta\hat{a}$ as $\hat{a}$ to reduce clutter.

---

[7] See the appendices to Ref. [13] for an introduction to the treatment of these fields in input-output theory.

### 2.2.1 Input-output relations

Including input and bath fields coupled to each mode, the Hamiltonian (2.12) gives rise to equations of motion according to

$$\frac{\mathrm{d}}{\mathrm{d}t}\hat{O} = \frac{i}{\hbar}[\hat{H}, \hat{O}] \tag{2.13}$$

for each operator $\hat{O}$, yielding

$$\frac{\mathrm{d}\hat{a}}{\mathrm{d}t} = -\left(i\Delta + \kappa/2\right)\hat{a} - ig_0\alpha(\hat{b} + \hat{b}^\dagger) - \sqrt{\kappa_e/2}\left(\hat{a}_{\mathrm{in}\rightarrow} + \hat{a}_{\mathrm{in}\leftarrow}\right) - \sqrt{\kappa_i}\,\hat{a}_{\mathrm{in},i}, \tag{2.14}$$

$$\frac{\mathrm{d}\hat{b}}{\mathrm{d}t} = -\left(i\Omega_\mathrm{m} + \gamma_{b,i}/2\right)\hat{b} - ig_0\left(\alpha^*\hat{a} + \alpha\hat{a}^\dagger\right) - iG_\mathrm{me}\hat{c} - \sqrt{\gamma_{b,i}}\,\hat{b}_\mathrm{in}, \tag{2.15}$$

$$\frac{\mathrm{d}\hat{c}}{\mathrm{d}t} = -\left(i\Omega_\mathrm{em} + \gamma_c/2\right)\hat{c} - iG_\mathrm{me}\hat{b} - \sqrt{\gamma_{c,e}}\,\hat{c}_\mathrm{in} - \sqrt{\gamma_{c,i}}\,\hat{c}_{\mathrm{in},i}. \tag{2.16}$$

The factor of two in $\sqrt{\kappa_e/2}$ is due to the use of two-sided optical coupling.

For now, we are interested in classical operation of this system and will replace the field operators with time-varying amplitudes. We will also set aside questions of noise until §2.4 and drop the unused input terms.

As above, we deal with the system when pumped optically at a frequency $\omega_L = \omega_\mathrm{opt} - \Delta$ with input drive $a_{0,\mathrm{in}}$, producing a cavity amplitude of $a_0$ at that frequency. We also consider the first upper and lower sidebands $a_-$ and $a_+$ at $\omega_L + \Omega$ and $\omega_L - \Omega$, respectively (labeled such that $a_-$ is resonant with the cavity when $\Delta = \Omega$, i.e. in

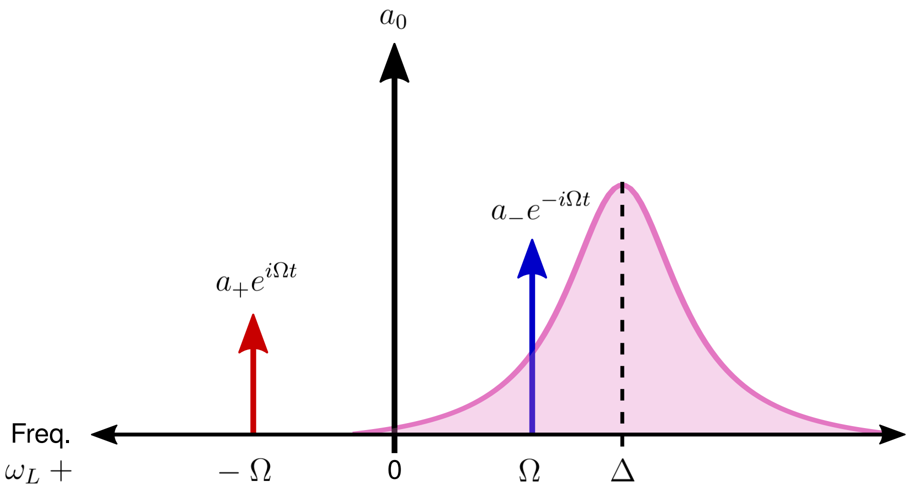

Figure 2.2: **Optical pump, sidebands, and cavity.** A red-detuned pump with amplitude $a_0$ is schematically represented with red sideband amplitude $a_+$ and blue sideband $a_-$. The blue sideband is near-resonant with the cavity (pink).

red-detuned operation).[8] The cavity amplitude in the rotating frame is

$$a(t) = a_0 + a_- e^{-i\Omega t} + a_+ e^{i\Omega t}. \tag{2.17}$$

These fields are represented schematically in Fig. 2.2.

We assume that the sideband fields are small compared to the pump, no matter what happens to them, so that we simply have $\alpha = a_0$ and average steady-state cavity photon number $n_{\text{opt}} = |a_0|^2$. We also assume higher-order sidebands are negligible. Similarly, we consider the microwave fields at signal frequency $\Omega$ as $b(t) = be^{-i\Omega t}$ and $c(t) = ce^{-i\Omega t}$. We then label the corresponding optical inputs and outputs in the forward direction $a_{\pm,\text{in}\rightarrow}$, $a_{\pm,\text{out}\rightarrow}$, and the microwave input and output $c_{\text{in}}$, $c_{\text{out}}$.

---

[8] The labeling of the sidebands may seem backwards, but like the sign of $\Delta$ it follows most (but not all) other references including Ref. [48]. One could take the sign to refer to the phase rotation in the rotating frame (that is, the sign of the exponent in Eqn. 2.17).

This leads to the input-output relations in the frequency domain

$$-i\Omega a_- = -\left(i\Delta + \kappa/2\right) a_- - i g_0 a_0 b - \sqrt{\kappa_e/2}\, a_{-,\mathrm{in}\rightarrow}, \tag{2.18}$$

$$-i\Omega a_+^* = -\left(-i\Delta + \kappa/2\right) a_+^* + i g_0 a_0^* b - \sqrt{\kappa_e/2}\, a_{+,\mathrm{in}\rightarrow}^*, \tag{2.19}$$

$$-i\Omega b = -\left(i\Omega_\mathrm{m} + \gamma_{b,i}/2\right) b - i g_0 \left(a_0^* a_- + a_0 a_+^*\right) - i G_\mathrm{me} c, \tag{2.20}$$

$$-i\Omega c = -\left(i\Omega_\mathrm{em} + \gamma_c/2\right) c - i G_\mathrm{me} b - \sqrt{\gamma_{c,e}}\, c_\mathrm{in}, \tag{2.21}$$

$$a_{\pm,\mathrm{out}\rightarrow} = a_{\pm,\mathrm{in}\rightarrow} - \sqrt{\kappa_e/2}\, a_\pm, \tag{2.22}$$

$$c_\mathrm{out} = c_\mathrm{in} - \sqrt{\gamma_{c,e}}\, c. \tag{2.23}$$

## 2.3 Electro-optomechanical transduction efficiency

We can now solve the above system of equations for the outputs in terms of the inputs to describe the transduction performed by the device.

We introduce the susceptibility[9] $\chi$ of each resonator, which relates each cavity field

---

[9] A more familiar definition of the mechanical susceptibility may be as the linear displacement response to a force with viscous damping; ours looks a bit different, since we are thinking in terms of the response to "input fields", which act on the first derivative of the amplitude rather than on the second derivative. Our description also makes the approximation that both mechanical quadratures are damped symmetrically, since the distinction is irrelevant near resonance when the damping is much slower than the oscillation frequency. For further discussion see Ref. [45].

to its input field in the absence of coupling, along with a normalized version $\Lambda$:[10]

$$\chi_{\text{opt}}^{-}(\Omega) \equiv \frac{1}{i\left(\Delta-\Omega\right)+\kappa/2}, \qquad \Lambda_{\text{opt}}^{-}(\Omega) \equiv \frac{\kappa}{2}\chi_{\text{opt}}^{-}(\Omega), \tag{2.24}$$

$$\chi_{\text{opt}}^{+}(\Omega) \equiv \frac{1}{i\left(\Delta+\Omega\right)+\kappa/2}, \qquad \Lambda_{\text{opt}}^{+}(\Omega) \equiv \frac{\kappa}{2}\chi_{\text{opt}}^{+}(\Omega), \tag{2.25}$$

$$\chi_{\text{m}}(\Omega) \equiv \frac{1}{i\left(\Omega_{\text{m}}-\Omega\right)+\gamma_{b,i}/2}, \qquad \Lambda_{\text{m}}(\Omega) \equiv \frac{\gamma_{b,i}}{2}\chi_{\text{m}}(\Omega), \tag{2.26}$$

$$\chi_{\text{em}}(\Omega) \equiv \frac{1}{i\left(\Omega_{\text{em}}-\Omega\right)+\gamma_{c}/2}, \qquad \Lambda_{\text{em}}(\Omega) \equiv \frac{\gamma_{c}}{2}\chi_{\text{em}}(\Omega). \tag{2.27}$$

Then a useful intermediate step is to write the mechanical amplitude $b$ in terms of inputs and outputs, with other fields in terms of $b$ and their own inputs:

$$a_{-} = \left(-ig_0 a_0 b - \sqrt{\kappa_e/2}\, a_{-,\text{in}\rightarrow}\right)\chi_{\text{opt}}^{-}(\Omega), \tag{2.28}$$

$$a_{+}^{*} = \left(ig_0 a_0^{*} b - \sqrt{\kappa_e/2}\, a_{+,\text{in}\rightarrow}^{*}\right)\left(\chi_{\text{opt}}^{+}(\Omega)\right)^{*}, \tag{2.29}$$

$$c = \left(-iG_{\text{me}} b - \sqrt{\gamma_{c,e}}\, c_{\text{in}}\right)\chi_{\text{em}}(\Omega), \tag{2.30}$$

$$\begin{aligned} b = {} & \frac{1}{i\left(\Omega_{\text{mech}}-\Omega\right)+\gamma_{b,i}/2+\left|a_0\right|^2 g_0^2\left(\chi_{\text{opt}}^{-}(\Omega)-\left(\chi_{\text{opt}}^{+}(\Omega)\right)^{*}\right)+G_{\text{me}}^2\chi_{\text{em}}(\Omega)} \\ & \times\left(ig_0\sqrt{\kappa_e/2}\,\left(a_0^{*}a_{-,\text{in}\rightarrow}\chi_{\text{opt}}^{-}(\Omega)+a_0 a_{+,\text{in}\rightarrow}^{*}\left(\chi_{\text{opt}}^{+}(\Omega)\right)^{*}\right)\right. \\ & \qquad \left. + iG_{\text{me}}\sqrt{\gamma_{c,e}}\, c_{\text{in}}\chi_{\text{em}}(\Omega)\right). \end{aligned} \tag{2.31}$$

The first term in the above expression for $b$ can be identified as an effective mechanical

---

[10] The norm squared of each $\Lambda$ is a Lorentzian with a maximum of 1 occurring on resonance, which can be a little more natural to reason about than a susceptibility. Note that $\Lambda_{\text{opt}}^{-}(\Omega)=1$ for positive $\Omega=|\Delta|$ when red detuned ($\Delta>0$), while $\Lambda_{\text{opt}}^{+}(\Omega)=1$ for positive $\Omega=|\Delta|$ when blue detuned ($\Delta<0$). These describe the cavity response for the corresponding frequency components of the optical field $a_{-}$ and $a_{+}$. I emphasize these details of notation because keeping them in mind makes many equations in the rest of this chapter easier to read and interpret.

susceptibility:

$$\begin{aligned}
\chi_{\mathrm{m,eff}}^{-1}(\Omega) &= \chi_{\mathrm{m}}^{-1}(\Omega) + |a_0|^2 g_0^2 \left(\chi_{\mathrm{opt}}^{-}(\Omega) - \left(\chi_{\mathrm{opt}}^{+}(\Omega)\right)^*\right) + G_{\mathrm{me}}^2 \chi_{\mathrm{em}}(\Omega) \\
&= i\left(\Omega_{\mathrm{m}} - \Omega\right) + \frac{\gamma_{b,i}}{2}\left(1 + \mathcal{C}_{\mathrm{om}}\left(\Lambda_{\mathrm{opt}}^{-}(\Omega) - \left(\Lambda_{\mathrm{opt}}^{+}(\Omega)\right)^*\right) + \mathcal{C}_{\mathrm{me}}\Lambda_{\mathrm{em}}(\Omega)\right) \qquad (2.32) \\
&\equiv \frac{\gamma_{b,i}}{2}\tilde{\Lambda}_{\mathrm{m,eff}}^{-1}(\Omega) \qquad (2.33)
\end{aligned}$$

where

$$\mathcal{C}_{\mathrm{om}} \equiv \frac{4\,|a_0|^2\, g_0^2}{\gamma_{b,i}\kappa}, \qquad \mathcal{C}_{\mathrm{me}} \equiv \frac{4G_{\mathrm{me}}^2}{\gamma_{b,i}\gamma_c} \tag{2.34}$$

are the optomechanical and mechano-electromechanical cooperativities, and we have placed a tilde on $\tilde{\Lambda}_{\mathrm{m,eff}}$ to remind us that unlike our other $\Lambda$ functions it may not be equal to 1 on resonance. (Moreover, its norm splits into multiple peaks at high cooperativities.) We can recognize the effective mechanical damping rate as

$$\gamma_{b,\mathrm{eff}} \equiv \gamma_{b,i}\mathrm{Re}\left[\left(1 + \mathcal{C}_{\mathrm{om}}\left(\Lambda_{\mathrm{opt}}^{-}(\Omega) - \left(\Lambda_{\mathrm{opt}}^{+}(\Omega)\right)^*\right) + \mathcal{C}_{\mathrm{me}}\Lambda_{\mathrm{em}}(\Omega)\right)\right]. \tag{2.35}$$

It is often useful to define the optomechanical or electromechanical damping rates for frequency-matched, sideband-resolved operation ($\Omega = \Omega_{\mathrm{m}} = \Omega_{\mathrm{em}} = \pm\Delta \gg \kappa$),

$$\gamma_{\mathrm{om}} \equiv \frac{4\,|a_0|^2\, g_0^2}{\kappa}, \qquad \gamma_{\mathrm{me}} \equiv \frac{4G_{\mathrm{me}}^2}{\gamma_c}, \tag{2.36}$$

and then think of the cooperativities as describing the competition between those rates and the intrinsic mechanical loss rate:

$$\mathcal{C}_{\mathrm{om}} = \frac{\gamma_{\mathrm{om}}}{\gamma_{b,i}}, \qquad \mathcal{C}_{\mathrm{me}} = \frac{\gamma_{\mathrm{me}}}{\gamma_{b,i}}. \tag{2.37}$$

Meanwhile, the $\Lambda$ functions (or susceptivities) in the denominator of $\tilde{\Lambda}^{-1}_{\mathrm{m,eff}}(\Omega)$ describe effective modifications of these interactions for off-resonant operation, whose complex parts lead to frequency shifts and whose real parts lead to an effective modification of the mechanical damping rate $\gamma_{b,i}$.

We thus see that the coupling to other modes induces a detuning-dependent self-interaction. In particular, the optical pump detuning (red or blue) changes the sign of the optomechanical damping term, leading to either damping (red) or anti-damping (blue), while the pump strength controls its magnitude through the factor of $|a_0|^2$.

### 2.3.1 Microwave-to-optical transduction

Driving only the microwave port ($a_{\pm,\mathrm{in}\rightarrow} = 0$) at frequency $\Omega$, we find the transmission to the upper and lower sidebands:

$$a_{-,\mathrm{out}\rightarrow} = -\frac{8a_0 g_0 G_{\mathrm{me}}}{\gamma_{b,i}\gamma_c\kappa}\sqrt{\gamma_{c,e}\kappa_e/2}\,\Lambda_{\mathrm{em}}(\Omega)\Lambda^{-}_{\mathrm{opt}}(\Omega)\tilde{\Lambda}_{\mathrm{m,eff}}(\Omega)\,c_{\mathrm{in}} \tag{2.38}$$

$$\left|\frac{a_{-,\mathrm{out}\rightarrow}}{c_{\mathrm{in}}}\right|^2 = \eta_{\mathrm{o}}\eta_{\mathrm{e}} \times 4\,\mathcal{C}_{\mathrm{om}}\mathcal{C}_{\mathrm{me}}\left|\Lambda_{\mathrm{em}}(\Omega)\Lambda^{-}_{\mathrm{opt}}(\Omega)\tilde{\Lambda}_{\mathrm{m,eff}}(\Omega)\right|^2, \tag{2.39}$$

$$a^*_{+,\mathrm{out}\rightarrow} = \frac{8a^*_0 g_0 G_{\mathrm{me}}}{\gamma_{b,i}\gamma_c\kappa}\sqrt{\gamma_{c,e}\kappa_e/2}\,\Lambda_{\mathrm{em}}(\Omega)\left(\Lambda^{+}_{\mathrm{opt}}(\Omega)\right)^*\tilde{\Lambda}_{\mathrm{m,eff}}(\Omega)\,c_{\mathrm{in}} \tag{2.40}$$

$$\left|\frac{a_{+,\mathrm{out}\rightarrow}}{c_{\mathrm{in}}}\right|^2 = \eta_{\mathrm{o}}\eta_{\mathrm{e}} \times 4\,\mathcal{C}_{\mathrm{om}}\mathcal{C}_{\mathrm{me}}\left|\Lambda_{\mathrm{em}}(\Omega)\Lambda^{+}_{\mathrm{opt}}(\Omega)\tilde{\Lambda}_{\mathrm{m,eff}}(\Omega)\right|^2 \tag{2.41}$$

where

$$\eta_{\mathrm{o}} \equiv \frac{\kappa_e/2}{\kappa}, \qquad \eta_{\mathrm{e}} \equiv \frac{\gamma_{c,e}}{\gamma_c} \tag{2.42}$$

are the optical and electrical external coupling ratios. (Note again the factor of 2 from the use of one optical port in two-sided coupling.)

Equations 2.39 and 2.41 describe the total microwave-to-optical transduction efficiency

$$\eta_{\mathrm{GHz}\to\mathrm{opt}} \equiv \left|\frac{a_{\pm,\mathrm{out}\to}}{c_{\mathrm{in}}}\right|^2_{a_{\mathrm{in}\to}=0} \tag{2.43}$$

$$= \eta_{\mathrm{o}}\eta_{\mathrm{e}} \times 4\,\mathcal{C}_{\mathrm{om}}\mathcal{C}_{\mathrm{me}}\left|\Lambda_{\mathrm{em}}(\Omega)\Lambda^{\pm}_{\mathrm{opt}}(\Omega)\tilde{\Lambda}_{\mathrm{m,eff}}(\Omega)\right|^2 \tag{2.44}$$

where we consider the near-resonant sideband to be the transmitted signal (that is, $a_{-,\mathrm{out}\to}$ when red detuned or $a_{+,\mathrm{out}\to}$ when blue detuned). For sideband-unresolved systems, there is also transmission into the off-resonant sideband, which depending on the detection scheme may cause interference in the actual detected signal (see §2.3.3).

We can also define an "internal" efficiency[11]

$$\eta_{\text{int}} \equiv \eta_{\text{GHz}\to\text{opt}}/(\eta_{\text{o}}\eta_{\text{e}}). \tag{2.45}$$

This efficiency is plotted as a function of cavity detuning and signal frequency in Fig. 2.3 for two different sets of device parameters.

In the case of frequency-matched mechanical and electromechanical modes with the optical pump red detuned by the mechanical frequency, while driving at that same frequency ($\Omega = \Omega_{\text{m}} = \Omega_{\text{em}} = \Delta$), the efficiency becomes

$$\eta_{\text{GHz}\to\text{opt}} = \eta_{\text{o}}\eta_{\text{e}} \times \frac{4\,\mathcal{C}_{\text{om}}\mathcal{C}_{\text{me}}}{\left|1 + \mathcal{C}_{\text{om}}\left(1 - \Lambda^{+}_{\text{opt}}(\Omega_{\text{m}})\right) + \mathcal{C}_{\text{me}}\right|^2}. \tag{2.46}$$

(In the experiment described in this thesis, our mechanical and electromechanical modes are separated by $\Omega_{\text{m}} - \Omega_{\text{em}} \approx \gamma_c$, so that $|\Lambda_{\text{em}}(\Omega_{\text{m}})|^2 \approx 0.2$, effectively reducing the peak efficiency by a factor of at least 5.)

If the system is also sideband-resolved ($\Omega_{\text{m}} \gg \kappa$), one can make the approximation

$$\eta_{\text{GHz}\to\text{opt}} \approx \eta_{\text{o}}\eta_{\text{e}} \times \frac{4\,\mathcal{C}_{\text{om}}\mathcal{C}_{\text{me}}}{(1 + \mathcal{C}_{\text{om}} + \mathcal{C}_{\text{me}})^2}. \tag{2.47}$$

---

[11] We should be careful in interpreting $\eta_{\text{int}}$. We can, as a straightforward matter of engineering, make $\eta_{\text{o}}$ and $\eta_{\text{e}}$ close to one by increasing the external coupling to the optical and electromechanical modes (and using one-sided optical coupling) so that $\kappa \approx \kappa_e$ and $\gamma_c \approx \gamma_{c,e}$. But the resulting increase in total damping $\kappa$ and $\gamma_c$ also affects $\eta_{\text{int}}$. Even if (as in our case) $\gamma_{c,e} \approx 0.01 \times \gamma_c$ so that the effect on total efficiency is mainly the increase in the coupling ratio $\eta_{\text{e}}$, the internal efficiency is not quite an idealized efficiency of a given device. Rather, it is a description of the "internal" part of efficiency that is dependent only on the rates of energy exchange between modes compared to total damping. It is still worth thinking about various idealizations of a device to determine directions for further work, but we will call the resulting efficiencies something else.

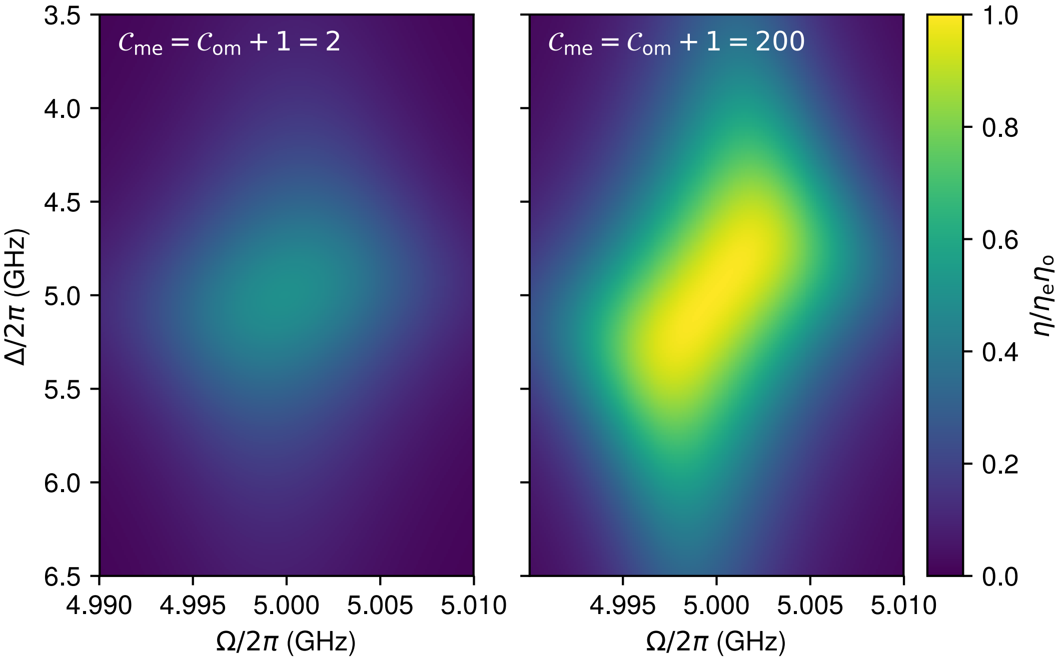

Figure 2.3: **Microwave-optical transduction efficiency.** Internal transduction efficiecy is plotted as a function of signal frequency $\Omega$ and cavity-laser detuning $\Delta > 0$ (red detuned). The model uses $\Omega_{\rm m} = \Omega_{\rm em} = 2\pi \times 5\,\text{GHz}$, $\gamma_c = 2\pi \times 25\,\text{MHz}$, $\kappa = 2\pi \times 1\,\text{GHz}$, $g_0 = 2\pi \times 1\,\text{MHz}$, and $G_{\rm me} = 2\pi \times 6.125\,\text{MHz}$. These parameters are somewhat better than those of the device measured in Chapter 5 but are intended to be realistically achievable. **Left:** $\gamma_{b,i} = 2\pi \times 3\,\text{MHz}$ and $n_{\rm opt} = 750$, so that $\mathcal{C}_{\rm me} = \mathcal{C}_{\rm om} + 1 = 2$, giving a maximum $\eta_{\rm int} = 0.5$ with a 3 dB bandwidth of around 10 MHz. **Right:** $\gamma_{b,i} = 2\pi \times 30\,\text{kHz}$ and $n_{\rm opt} = 1500$, so that $\mathcal{C}_{\rm me} = \mathcal{C}_{\rm om} + 1 = 200$, giving a maximum $\eta_{\rm int}$ near the ideal value of 1 with a 3 dB bandwidth slightly above 10 MHz. A 100-fold increase in mechanical $Q_i$ is chosen to be comparable to what has been achieved in a number of cryogenic silicon optomechanical experiments.

When considering this efficiency as a function of one cooperativity with the other fixed, we find the efficiency-maximizing cooperativities

$$\mathcal{C}_{\mathrm{om}}^{\star} = \mathcal{C}_{\mathrm{me}} + 1 \qquad \text{for fixed } \mathcal{C}_{\mathrm{me}} \text{ and} \tag{2.48}$$

$$\mathcal{C}_{\mathrm{me}}^{\star} = \mathcal{C}_{\mathrm{om}} + 1 \qquad \text{for fixed } \mathcal{C}_{\mathrm{om}}. \tag{2.49}$$

This can be thought of as an impedance matching condition in light of the effective mechanical susceptibility, such that the loading (increase in linewidth) of the mechanical mode induced by one coupling is equal to the intrinsic loss rate plus the loading by the other mode (see Eqns. 2.32–2.37). Thus for a given device (since $\mathcal{C}_{\mathrm{me}}$ is fixed), we want to set the pump power according to Eqn. 2.48; when designing the device, we consider Eqn. 2.49 along with the parameters we expect to be achievable (as in §3.2.1). In practice, heating of the cavity by the pump limits the $\mathcal{C}_{\mathrm{om}}$ we can (usefully) achieve, although this can be mitigated by operation with short pulses. At the optimum points given by these equations, the ideal efficiency is $0.5\eta_{\mathrm{o}}\eta_{\mathrm{e}}$ when the smaller cooperativity is 1, and it approaches $\eta_{\mathrm{o}}\eta_{\mathrm{e}}$ for cooperativities greater than 1. An overcoupled device in the high-cooperativity limit can thus approach the ideal efficiency of 1, with minimal added noise as described in §2.4 below.

For the equivalent blue-detuned case ($\Delta < 0$), we have the efficiency

$$\left|\frac{a_{+,\mathrm{out}\rightarrow}}{c_{\mathrm{in}}}\right|^2 \approx \eta_{\mathrm{o}}\eta_{\mathrm{e}} \times \frac{4\,\mathcal{C}_{\mathrm{om}}\mathcal{C}_{\mathrm{me}}}{(1-\mathcal{C}_{\mathrm{om}}+\mathcal{C}_{\mathrm{me}})^2} \tag{2.50}$$

as long as $1 - \mathcal{C}_{\mathrm{om}} + \mathcal{C}_{\mathrm{me}} > 0$ (otherwise, the mechanical mode enters a self-amplification regime and will ultimately be limited by some nonlinearity). We can thus achieve gain by operating with blue detuning, which comes at the cost of noise through amplification of the mechanical mode and enhanced shot-noise scattering of pump photons depositing energy into the mechanics (see §2.4).

**Transduction bandwidth**

The transduction bandwidth is also an important figure of merit, since it limits the speed at which transduction operations can be performed. The frequency dependence of the transduction efficiency comes from the responses of the various cavities near that frequency—specifically, from the term

$$\left|\Lambda_{\mathrm{em}}(\Omega)\Lambda_{\mathrm{opt}}^{\pm}(\Omega)\tilde{\Lambda}_{\mathrm{m,eff}}(\Omega)\right|^2 \tag{2.51}$$

in Eqns. 2.39 and 2.41. We can define the transduction bandwidth as the range of signal frequency $\Omega$ over which transduction efficiency is at least half of the maximum efficiency. This bandwidth will be maximized in red detuned operation, through the optomechanical effect on $\tilde{\Lambda}_{\mathrm{m,eff}}(\Omega)$.

The optical lineshape $\left|\Lambda_{\mathrm{opt}}^{-}(\Omega)\right|^2$ around $\Omega \sim \Omega_{\mathrm{m}}$ is relatively flat and will not affect the bandwidth much (that is, $\kappa \gg \gamma_c, \gamma_{b,\mathrm{eff}}$ in practice). At low cooperativity ($C_{\mathrm{om,me}} < 1$) we can see from the remaining terms that the transduction bandwidth will be smaller than $\gamma_c$ and $\gamma_{b,\mathrm{eff}} \approx \gamma_{b,i}$, since the efficiency is approximately proportional to the product of two Lorentzians with those linewidths. With some analysis, one can show that the red detuned, high-cooperativity limit ($\Delta = \Omega_m$, $C_{\mathrm{om}} \approx C_{\mathrm{me}} \gg 1$) gives a limiting maximum bandwidth of twice the electromechanical damping rate ($2\gamma_c$ in angular frequency units).

We can thus achieve high bandwidth by making the external electromechanical coupling $\gamma_{c,e}$ large (as long as large, matched cooperativities can still be obtained).[12] It is also possible to trade off maximum efficiency for more bandwidth, for example by operating above the optimal pump power.

Note that this bandwidth is directly related to time-domain operation in the usual way for the case of a continuous-wave pump with pulsed signals. In Chapter 5, we instead operate in the time domain by pulsing the optical pump power, making the equations of motion (2.14–2.16) explicitly time dependent through $\alpha(t)$.

### 2.3.2 Optical-to-microwave transduction

If we return to Eqns. 2.28–2.31 and consider optical-to-microwave transduction ($c_{\mathrm{in}} = 0$), we find the output microwave field

$$\begin{aligned} c_{\mathrm{out}} = &-\frac{8 g_0 G_{\mathrm{me}}}{\gamma_{b,i}\gamma_c\kappa}\sqrt{\gamma_{c,e}\kappa_e/2}\,\Lambda_{\mathrm{em}}(\Omega)\tilde{\Lambda}_{\mathrm{m,eff}}(\Omega) \\ &\times \left(a_0^* a_{-,\mathrm{in}\rightarrow}\Lambda_{\mathrm{opt}}^{-}(\Omega) + a_0 a_{+,\mathrm{in}\rightarrow}^{*}\left(\Lambda_{\mathrm{opt}}^{+}(\Omega)\right)^{*}\right). \end{aligned} \tag{2.52}$$

---

[12] This can be compared to the system described in Refs. [1, 24], which is similar to ours except that mode $c$ is optomechanically coupled to a much lower-frequency mechanical mode $b$. While it produces a similar functional form for transduction efficiency when the pumps for both the $c$ and $a$ modes are red detuned and sideband resolved, the bandwidth is limited in practice by the low mechanical frequency, since it sets the top of the frequency hierarchy below which electromagnetic linewidths and optomechanical couplings must sit [2].

When driving with a single sideband, this gives us the transmission

$$\left|\frac{c_{\text{out}}}{a_{\pm,\text{in}\rightarrow}}\right|^2 = \eta_{\text{o}}\eta_{\text{e}} \times 4\,\mathcal{C}_{\text{om}}\mathcal{C}_{\text{me}} \left|\Lambda_{\text{em}}(\Omega)\Lambda^{\pm}_{\text{opt}}(\Omega)\tilde{\Lambda}_{\text{m,eff}}(\Omega)\right|^2. \tag{2.53}$$

Taking the efficiency $\eta_{\text{opt}\rightarrow\text{GHz}}$ to be the transmission from the resonant sideband (that is, $a_{-,\text{in}\rightarrow}$ when red detuned or $a_{+,\text{in}\rightarrow}$ when blue detuned), we see that

$$\eta_{\text{opt}\rightarrow\text{GHz}} = \eta_{\text{GHz}\rightarrow\text{opt}} \equiv \eta. \tag{2.54}$$

### 2.3.3 Interference between sidebands

In our microwave-to-optical experimental setup, we detect the beat at frequency $\Omega$ between the transmitted pump and both sidebands with a fast photodiode (detection bandwidth $\sim 2\Omega_{\text{m}}$), whose output at $\Omega$ is

$$V_{\text{FPD}} = G_{\text{det}}\left(a^*_{0,\text{out}\rightarrow}a_{-,\text{out}\rightarrow} + a_{0,\text{out}\rightarrow}a^*_{+,\text{out}\rightarrow}\right) \tag{2.55}$$

with some total gain $G_{\text{det}}$ in the output chain. The gain may vary with power and wavelength, and is calibrated using a known input pump and phase-modulation-induced sidebands, together with the optical transfer function of the device chip as determined from other measurements. We then use our model to calculate the relative amplitudes and phases of the beat terms and infer the amplitude in the near-resonant sideband ($a_{+,\text{out}\rightarrow}$ when blue detuned).

For optical-to-microwave measurements, we drive an optical phase modulator at the signal frequency, generating upper and lower sidebands of equal amplitude. Each sideband is transduced with a different phase and amplitude, and the detected microwave signal is determined by their interference (Eqn. 2.52). Again, we can model this interference in order to calculate the efficiency of transduction from a single-sideband drive.[13]

Note that there is a factor of $\left(\Lambda^{-}_{\text{opt}}(\Omega) - \left(\Lambda^{+}_{\text{opt}}(\Omega)\right)^*\right)$ multiplying $\mathcal{C}_{\text{om}}$ in the denominator of the efficiency, coming from the effective mechanical susceptibility (Eqn. 2.32). This is also a kind of sideband-resolution factor (being approximately ±1 for resonant sideband-resolved operation), but there is not (and should not be) any correction for this, since it is intrinsic to the device rather than attributable to the detection or drive scheme.[14]

Since these procedures for correcting for sideband interference rely on the accuracy of the model, they are susceptible to systematic error, and this will be reflected in the calculated uncertainty ranges. For example, if the true value of $\kappa$ is near the lower end of its plausible range, that error will affect all calculations of microwave-to-optical efficiency in the same way by leading us to overestimate the effect of sideband interference. Similarly, if $\kappa$ increases at high power, there will be a power-dependent error.

---

[13] For both of the sideband correction factors, it is necessary to keep track of the phase of $a_0$, since the phase of the inputs, cavity amplitudes, and outputs are all interrelated. For this reason we did not assume $\alpha$ or $a_0$ were real at any point.

[14] To be clear, it is possible to configure a setup for driving with or detecting a single sideband. In some other experiments, the optical output is filtered using a narrow-bandwidth tunable filter centered on the signal sideband, allowing direct photodetection of the sideband power. A single-sideband input signal can also be produced, for example by using a second laser phase-locked to the pump laser.

## 2.4 Added noise

Noise not present in the signal may also be introduced by the device, mainly by unwanted scattering from the optical pump into the lower sideband or by thermal occupation of the mechanical mode.

A pedagogical introduction to quantum noise, measurement, and amplification may be found in Ref. [13].

For simplicity, consider the case of perfect one-sided coupling ($\kappa = \kappa_e, \gamma_c = \gamma_{c,e}$), where $\hat{a}_{\text{in}}$ is the vacuum and $\hat{b}_{\text{in}}$ and $\hat{c}_{\text{in}}$ are thermal baths. We consider the Fourier transformed operators,[15] which satisfy

$$\langle \hat{O}^\dagger_{\text{in}}(\Omega)\hat{O}_{\text{in}}(\Omega')\rangle = n_O\delta(\Omega+\Omega') \tag{2.56}$$

$$\langle \hat{O}_{\text{in}}(\Omega)\hat{O}^\dagger_{\text{in}}(\Omega')\rangle = (n_O+1)\delta(\Omega+\Omega') \tag{2.57}$$

where $n_O$ is the mean thermal occupancy of bath $\hat{O}_{\text{in}}$, expressed in terms of bath temperature as $n_O = 1/(e^{\hbar\Omega/k_BT}-1)$ at frequency $\Omega$.

The mechanical mode is then described by annihilation operator

$$\begin{aligned}\hat{b} = \Bigg(& ig_0\sqrt{\kappa}\left(a_0^*\hat{a}_{\text{in}}\chi^-_{\text{opt}}(\Omega) + a_0\hat{a}^\dagger_{\text{in}}\left(\chi^+_{\text{opt}}(\Omega)\right)^*\right) \\ &+ iG_{\text{me}}\sqrt{\gamma_c}\,\hat{c}_{\text{in}}\chi_{\text{em}}(\Omega) + \sqrt{\gamma_{b,i}}\,\hat{b}_{\text{in}}\Bigg) \times \chi_{\text{m,eff}}(\Omega),\end{aligned} \tag{2.58}$$

---

[15] We define $\hat{O}(\Omega) \equiv \frac{1}{\sqrt{2\pi}}\int_{-\infty}^{\infty} \mathrm{d}t\, e^{i\Omega t}\hat{O}(t)$ and write the transformed annihilation operator $\hat{O}^\dagger(\Omega) \equiv (\hat{O}(-\Omega))^\dagger = \frac{1}{\sqrt{2\pi}}\int_{-\infty}^{\infty} \mathrm{d}t\, e^{i\Omega t}\hat{O}^\dagger(t)$, generally following Ref. [13].

which gives us the correlator and spectral density[16]

$$\begin{aligned}\langle \hat{b}^\dagger(\Omega)\hat{b}(\Omega')\rangle = \Bigg( & |a_0|^2 g_0^2 \kappa\, \chi_{\mathrm{opt}}^{+}(-\Omega)\left(\chi_{\mathrm{opt}}^{+}(\Omega')\right)^* + G_{\mathrm{me}}^2 \gamma_c n_c \chi_{\mathrm{em}}^*(-\Omega)\chi_{\mathrm{em}}(\Omega') \\ & + \gamma_{b,i} n_b \Bigg) \times \delta(\Omega+\Omega')\chi_{\mathrm{m,eff}}^*(-\Omega)\,\chi_{\mathrm{m,eff}}(\Omega'), \end{aligned} \tag{2.59}$$

$$\begin{aligned} S_{bb}(\Omega) = \Bigg( & |a_0|^2 g_0^2 \kappa \left|\chi_{\mathrm{opt}}^{+}(-\Omega)\right|^2 + G_{\mathrm{me}}^2 \gamma_c n_c \left|\chi_{\mathrm{em}}(-\Omega)\right|^2 \\ & + \gamma_{b,i} n_b \Bigg) \left|\chi_{\mathrm{m,eff}}(-\Omega)\right|^2 . \end{aligned} \tag{2.60}$$

The spectral density of the annihilation operator peaks at negative frequency and can be viewed as describing the tendency of the mechanical mode to emit energy. The spectral density for the creation operator is similar but peaks at positive frequency and replaces $n_{[b,c]}$ with $n_{[b,c]} + 1$; it can be viewed as describing the tendency of the mechanical mode to absorb energy, which is not symmetrical with the tendency to emit energy near the quantum ground state.

If we remove the coupling to the electromechanical mode, we can recover an important result in quantum optomechanics: the quantum limit of optomechanical cooling [38, 64]. When red detuned ($\Omega_{\mathrm{m}} = \Delta$) in the resolved sideband regime ($\Omega_{\mathrm{m}} \gg \kappa$), integrating the spectral density (while assuming $\kappa \gg \gamma$) gives us the final mean phonon occupation

$$n_f = \frac{\gamma_{b,i}}{\gamma_{b,i} + \gamma_{b,\mathrm{om}}} n_b + \frac{\gamma_{b,\mathrm{om}}}{\gamma_{b,i} + \gamma_{b,\mathrm{om}}} \left(\frac{\kappa}{4\Omega_{\mathrm{m}}}\right)^2 \tag{2.61}$$

---

[16] The quantum spectral density is defined in analogy to the (two-sided) classical version: $S_{OO}(\Omega) \equiv \int_{-\infty}^{\infty} \mathrm{d}t\, e^{i\Omega t} \langle \hat{O}^\dagger(t)\hat{O}(0)\rangle = \frac{1}{2\pi}\int_{-\infty}^{\infty} \mathrm{d}\Omega' \, \langle \hat{O}^\dagger(\Omega)\hat{O}(\Omega')\rangle$. Unlike the classical version, it is not necessarily symmetric in frequency.

where $\gamma_{b,\mathrm{om}} = 4\left|a_0\right|^2 g_0^2/\kappa$ is the optomechanical damping rate (Eqn. 2.36). The first term represents the thermal population under the cooling effect from optomechanical damping, while the second comes from optical backaction, in which cavity pump photons scatter into the off-resonant sideband in a shot-noise process, depositing energy into the mechanical mode. For $\gamma_{b,\mathrm{om}} \gg \gamma_{b,i}$ the occupation approaches the lower limit

$$n_{\min} = \left(\frac{\kappa}{4\Omega_{\mathrm{m}}}\right)^2. \tag{2.62}$$

This backaction and mechanical thermal noise then appears at each output port, following Eqns. 2.18–2.23. This produces correlations between the noise at different ports; Ref. [24] uses similar correlations (with noise from a mechanical mode at 1.5 MHz) in a feed-forward scheme to reduce the effective noise added by their device. In addition, the noise at the output port due to an input's backaction on the mechanics will produce correlations with the transmitted or reflected input noise, potentially resulting in squeezing, as demonstrated with a low-frequency mode of a silicon zipper optomechanical cavity in Ref. [49].

We can also simply consider the noise added by the device at each port. At the microwave output port, we calculate the added photon number[17] $N_{\mathrm{o}}$ due to shot-noise

---

[17] The added noise for a network scattering process with "gain" $G$ (not necessarily $> 1$), such as amplification, is often described as a number $N = \bar{S}_{\mathrm{out}}(\Omega)/\hbar\Omega G$ of added photons. Here $\bar{S}_{\mathrm{out}}$ denotes the one-sided noise power spectral density due to noise not present in the input signal. This should be taken to mean that this excess noise power in the output at the signal frequency $\Omega$, "referred to the input" (that is, divided by the gain, to get the power at the input that would produce this power at the output), is $N\hbar\Omega$ per second in a 1 Hz bandwidth. Typical signal and detection bandwidths are much narrower than the bandwidth of the noise processes, so that the noise power spectral density is constant over the detection bandwidth. In this way we can talk about added noise as a single number, as though a thermal source with mean occupation $N$ had been added on top of the input. (The equivalent "noise

scattering events from the pump and $N_\mathrm{m}$ due to the mechanical thermal motion:

$$\begin{aligned} N_\mathrm{o}(\Omega_\mathrm{m}) &\approx \frac{1}{\eta} G_\mathrm{me}^2 \gamma_{c,e} \left|a_0\right|^2 g_0^2 \kappa \left|\chi_\mathrm{opt}^+(\Omega_\mathrm{m})\chi_\mathrm{m,eff}(\Omega_\mathrm{m})\chi_\mathrm{me}(\Omega_\mathrm{m})\right|^2 \\ &= \frac{1}{\eta_\mathrm{o}} \left|\frac{\Lambda_\mathrm{opt}^+(\Omega_\mathrm{m})}{\Lambda_\mathrm{opt}^-(\Omega_\mathrm{m})}\right|^2, \qquad (2.63) \\ N_\mathrm{m}(\Omega_\mathrm{m}) &\approx \frac{1}{\eta} G_\mathrm{me}^2 \gamma_{c,e} \gamma_{b,i} n_b \left|\chi_\mathrm{m,eff}(\Omega_\mathrm{m})\chi_\mathrm{me}(\Omega_\mathrm{m})\right|^2 \\ &= \frac{1}{\eta_\mathrm{o}} \frac{n_b}{\mathcal{C}_\mathrm{om}} \frac{1}{\left|\Lambda_\mathrm{opt}^-(\Omega_\mathrm{m})\right|^2}. \qquad (2.64) \end{aligned}$$

Meanwhile, at the optical signal output port we have

$$N_\mathrm{o}(\Omega_\mathrm{m}) \approx \frac{1}{\eta_\mathrm{e}} \frac{\mathcal{C}_\mathrm{om}}{\mathcal{C}_\mathrm{me}} \left|\frac{\Lambda_\mathrm{opt}^+(\Omega_\mathrm{m})}{\Lambda_\mathrm{em}(\Omega_\mathrm{m})}\right|^2, \qquad (2.65)$$

$$N_\mathrm{m}(\Omega_\mathrm{m}) \approx \frac{1}{\eta_\mathrm{e}} \frac{n_b}{\mathcal{C}_\mathrm{me}} \frac{1}{\left|\Lambda_\mathrm{em}(\Omega_\mathrm{m})\right|^2}. \qquad (2.66)$$

Note that these results are valid for both red and blue detuning, and show that blue-detuned operation (when $\left|\Lambda_\mathrm{opt}^+(\Omega_\mathrm{m})\right|^2 \approx 1$) has worse noise performance.

For red-detuned, resonant, sideband-resolved operation with high cooperativities, the added noise is still bounded below (for the same reason as with the identical cooling limit

---

temperature" is also often used.)

of Eqn. 2.62) by

$$\begin{aligned} N_{\mathrm{min}} &\approx \left|\Lambda^{+}_{\mathrm{opt}}(\Omega_{\mathrm{m}})\right|^2 \\ &= \frac{(\kappa/2)^2}{4\Omega_{\mathrm{m}}^2 + (\kappa/2)^2} \\ &\approx \left(\frac{\kappa}{4\Omega_{\mathrm{m}}}\right)^2 . \end{aligned} \tag{2.67}$$

There is also thermal noise in the microwave electromechanical mode; the effect on transduction can be analyzed in the same way. We generally expect that mode to be better thermalized to a cryogenic environment than the mechanical resonance, both because of larger thermal conductance to the environment in a quasi-2D geometry and because it is not directly heated by the optical pump.

# Chapter 3

# The optomechanical element

In the next two chapters, we discuss the design and analysis of the individual components of our electro-optomechanical device, beginning in this chapter with the optomechanical element. This element consists of a nanobeam design similar to that used in many on-chip optomechanical experiments, with some important modifications to that design in order to allow a mechanical signal to be coupled in and out without sacrificing the desired properties of the nanobeam.

## 3.1 Optomechanical crystal devices

An overview of optomechanical crystal devices is provided by Ref. [50], while Ref. [27] is an excellent textbook on photonic crystals.

### 3.1.1 Band structure

Electromagnetic and acoustic waves are each governed by a master equation that takes the form of an eigenproblem $\hat{\Theta}\mathbf{u} = \alpha\mathbf{u}$ for the appropriate differential operator $\hat{\Theta}$, field $\mathbf{u}$, and eigenvalue $\alpha$. For the electromagnetic problem with spatially-varying dielectric constant $\varepsilon(\mathbf{r})$, we obtain an equation for the magnetic field $\mathbf{H}$ from Maxwell's equations:

$$\nabla \times \left( \frac{1}{\varepsilon(\mathbf{r})} \nabla \times \mathbf{H}(\mathbf{r}) \right) = \left( \frac{\omega}{c} \right)^2 \mathbf{H}(\mathbf{r}). \tag{3.1}$$

For the mechanical problem with displacement $\mathbf{u}$ (in an infinite solid)

$$\nabla \cdot \mathbf{T}(\mathbf{r}) = -\rho\Omega^2 \mathbf{u}(\mathbf{r}), \qquad \text{where} \tag{3.2}$$

$$T_{ij}(\mathbf{r}) = c_{ijkl} \frac{1}{2} \left( \frac{\partial u_k}{\partial r_l} + \frac{\partial u_l}{\partial r_k} \right). \tag{3.3}$$

The mass $\rho$ and stiffness $c_{ijkl}$ may vary spatially. In our cases of interest, they are uniform in a finite volume; our control over the problem enters instead through an additional system of equations specifying zero normal stress at the boundaries. The discussion below applies just as well to our mechanical problem, using the entire system including the eigenvalue equation and boundary conditions together.

Waves in periodic structures can be described as the product of a plane wave and a function with the periodicity of the structure; this result is known as Bloch's theorem. The essential idea of Bloch's theorem is that we can find a set of solutions to our original eigenproblem that are also eigenvectors of the discrete translation symmetry of the differential operator $\hat{\Theta}$. We can thus express such a solution as a superposition of plane waves all related by the reciprocal lattice vector, or equivalently as a plane wave times a function with the periodicity of the lattice.

These solutions can then be indexed by wavevector; the corresponding eigenvalues and lattice-periodic functions vary continuously with wavevector and can be grouped into "bands" characterized by the lattice-periodic function. The "band structure", which summarizes the relationships between band index, wavevector, and frequency, can be tailored by designing an appropriate unit cell that repeats with translations by the lattice vector. Such structures, when designed with optical (or acoustic) band structure in mind, are known as photonic (or phononic) crystals.

Unlike in a homogeneous continuum, there does not necessarily exist a mode of a given polarization at all frequencies. In fact, we can design a structure to have a "bandgap" around our frequency of interest in which no waves of the target polarization propagate.

### One-dimensional Bloch's theorem

As a specific example, we consider electromagnetic waves in an infinite structure with one-dimensional periodicity with lattice constant $a$ in the $x$ direction. We write the lattice vector $\mathbf{a} = a\hat{\mathbf{x}}$ and reciprocal lattice vector $\mathbf{k_a} = 2\pi a^{-1}\hat{\mathbf{x}}$. We take the structure to be infinite and homogeneous in the $y$ and $z$ directions; the master equation is separable and gives us solutions with plane-wave dependence in those coordinates. The dielectric constant $\varepsilon(\mathbf{r})$ has a discrete translation symmetry, whose translation operator we call $\hat{T}_{\mathbf{a}}$:

$$\hat{T}_{\mathbf{a}}\varepsilon(\mathbf{r}) = \varepsilon(\mathbf{r}+\mathbf{a}) = \varepsilon(\mathbf{r}). \tag{3.4}$$

The translation operator $\hat{T}_{\mathbf{a}}$ and differential operator $\hat{\Theta}$ then commute, meaning that we can write down a set of solutions $\mathbf{H}$ where each is a superposition of degenerate eigenvectors of $\hat{T}_{\mathbf{a}}$.[1] These latter eigenvectors are plane waves with wavevector $\mathbf{k} \equiv k_x\hat{\mathbf{x}} + k_y\hat{\mathbf{y}} + k_z\hat{\mathbf{z}}$ and eigenvalue $e^{i\mathbf{k}\cdot\mathbf{a}}$:

$$\mathbf{H}_{\mathbf{k}}(\mathbf{r}) = \mathbf{H}_0 e^{i\mathbf{k}\cdot\mathbf{r}}, \tag{3.5}$$

$$\hat{T}_{\mathbf{a}}\mathbf{H}_{\mathbf{k}}(\mathbf{r}) = e^{i\mathbf{k}\cdot\mathbf{a}}\mathbf{H}_{\mathbf{k}}(\mathbf{r}). \tag{3.6}$$

Since $e^{i\mathbf{k}_{\mathbf{a}}\cdot\mathbf{a}} = 1$, plane waves whose wavevector can be written $\mathbf{k}+m\mathbf{k}_{\mathbf{a}}$ for a given $\mathbf{k}$ and some integer $m$ have the same eigenvalue $e^{i\mathbf{k}\cdot\mathbf{a}}$. With that in mind, we characterize these degenerate sets by their unique such $\mathbf{k}$ with $-\pi/a < k_x \leq \pi/a$.

We can write each solution to the master equation expanded in one of these sets of

---

[1] This is a basic result in quantum mechanics; see e.g. Ref. [51].

plane waves, indexed by wavevector:

$$
\begin{aligned}
\mathbf{H}_{\mathbf{k},n}(\mathbf{r}) &= e^{i(k_y y + k_z z)} \sum_m \mathbf{c}_{\mathbf{k},m,n} e^{i(\mathbf{k}+m\mathbf{k_a})\cdot\mathbf{r}} \\
&= e^{i\mathbf{k}\cdot\mathbf{r}} \sum_m \mathbf{c}_{\mathbf{k},m,n} e^{i(m\mathbf{k_a})\cdot\mathbf{r}} \\
&= e^{i\mathbf{k}\cdot\mathbf{r}} \mathbf{u}_{\mathbf{k},n}(\mathbf{r}). \qquad (3.7)
\end{aligned}
$$

This is the result usually called Bloch's theorem (or at least a version with one-dimensional periodicity). We have defined the so-called Bloch functions $\mathbf{u}_{\mathbf{k},n}(\mathbf{r})$ to be the sum in the second line, noting that they are periodic with the periodicity of the lattice. In fact, for each wavevector $\mathbf{k}$, there are infinitely many solutions, each belonging to a family or "band" (which we have labeled with band index $n$), within which the frequency and Bloch function vary continuously with $\mathbf{k}$.

Structures that are periodic or finite in other directions, like our quasi-1D nanobeams, can be analyzed similarly. In our case, optical modes with $\omega > ck_x$ ("above the light line" as drawn in a band structure diagram) must propagate outside of the nanobeam, while modes with $\omega < ck_x$ can be index guided, decaying exponentially away from the nanobeam.

### 3.1.2 Bandgaps

As mentioned above, bands of a given polarization are often separated by a bandgap in photonic and phononic crystals.[2] To understand this a little further, we consider optical modes in a periodic dielectric waveguide with elliptical holes, using the unit cell in Fig. 3.1.

The resulting band structure is shown in Fig. 3.2a. Since modes with the same wavevector must be distinguished by their Bloch function, we should look to the part of the mode that shares the periodicity of the lattice to gain some intuition for the origin of the bandgap. This will be clearest when $k_x = \pi/a$, where the plane-wave envelope of the eigenfunction gives a wavelength of two unit cells.

We see in Fig. 3.2b that the lower-frequency band has a maximum of electric-field energy density in the dielectric between holes, while the higher-frequency band has its energy distribution centered in the hole. (These are conventionally called the dielectric and air bands, respectively, for this reason.)

These modes would be degenerate in the absence of periodic patterning. The frequency difference between them can be understood from the perspective of the varia-

---

[2] Our quasi-1D photonic and phononic crystals do not have simultaneous bandgaps for modes of all polarizations or symmetries. The bandgaps should thus be described as "incomplete", and the defect modes are protected from decay into guided modes at the same frequency by the symmetry of the unit cell. Any asymmetries, such as angled sidewalls or random perturbations introduced during fabrication, can introduce coupling to these guided modes. Moreover, radiative optical modes exist at all frequencies for small enough $k_x$; all localized modes will have some radiative loss via these modes. (And more tightly localized modes will have a larger spread in reciprocal space, thus decreasing $Q$.) It turns out that complete phononic bandgaps can be achieved in quasi-2D designs, allowing very high quality factors if other sources of loss are eliminated, as with the acoustic mode of Ref. [35]. In this thesis, if not otherwise specified, the term "bandgap" should be taken to mean an incomplete bandgap for the modes under discussion.

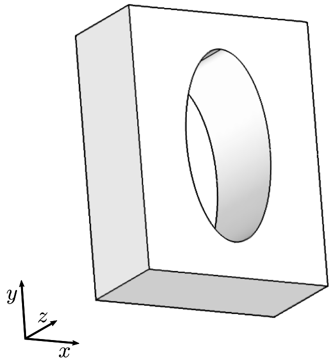

Figure 3.1: **Optomechanical nanobeam "mirror" unit cell,** with width in the $y$ direction $w = 566\,\text{nm}$, thickness $t = 220\,\text{nm}$, and elliptical hole diameters $d_x = 197\,\text{nm}$, $d_y = 413\,\text{nm}$, which repeats with periodicity $a$ in the $x$ direction.

tional formulation of the electromagnetic problem, in which the concentration of energy in low- or high-dielectric regions is related to the variational cost of these two ways of drawing the electric field while respecting Maxwell's equations and the symmetry of the unit cell (see Ref. [27] for more detail). One can also verify in simulation that increasing the effective dielectric contrast between the high-index and low-index parts of the unit cell (for example, by enlarging the hole) increases the size of the bandgap relative to its center frequency.[3]

The mechanical band structure of the same unit cell is shown in Fig. 3.3, with a bandgap for fully symmetric modes between 2.6 and 5 GHz.

---

[3] Another way of thinking about the origin of the bandgap in a periodic medium is from the perspective of the medium as an effective Bragg mirror. In this picture, originating in the analysis of a stack of layers of alternating dielectric constant, an incident wave will partially reflect off of each interface. For certain frequency ranges, these partial reflections interfere constructively, producing a nearly complete reflection. Although we describe photonic and phononic crystals in terms of band structures, the Bragg-mirror picture can also be useful for complementary intuition. In this picture, for example, increasing contrast widens the reflective bandwidth by increasing the reflection at each interface, thus decreasing the overall penetration depth into the mirror; since the nearer reflections become more important, and the phase accumulated by these reflections is less sensitive to the frequency, the constructive-interference condition becomes more lenient with respect to frequency.

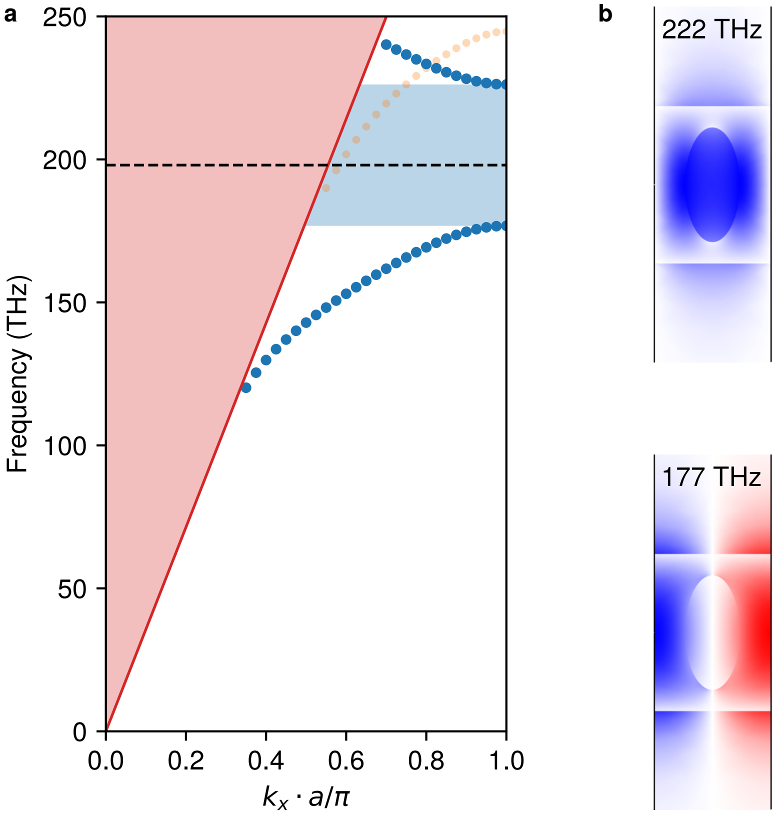

Figure 3.2: **Simulated optical band structure of the unit cell in Fig. 3.1. a,** Optical band structure diagram showing the two lowest-frequency TE-like modes with $y$-inversion symmetry in the electric field, with an incomplete bandgap between 177 and 222 THz (blue shaded region). The lowest-frequency TM-like band is shown in orange. The black dotted line denotes the frequency of a "defect mode" that can be localized by a defect in the photonic crystal (see §3.1.3). The "light line" (red) marks the boundary between the bands of guided modes and the continuum of extended radiating modes (shaded red). (Guided modes very close to the light line are not captured by the finite simulation volume.) **b,** The electric field in the $y$ direction, for the $k_x = \pi/a$ mode in the dielectric (lower) and air (upper) bands.

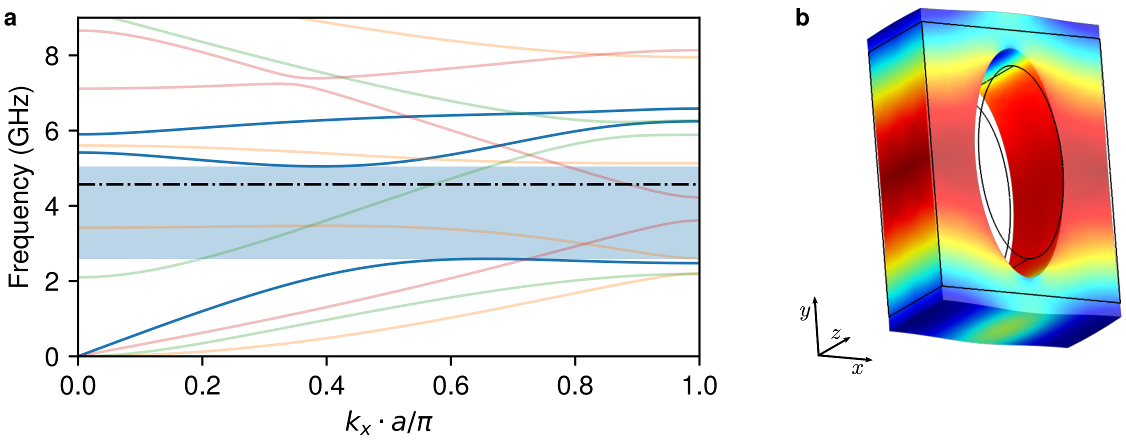

Figure 3.3: **Simulated mechanical band structure of the unit cell in Fig. 3.1. a,** Band structure diagram with fully symmetric modes in blue, showing a bandgap between 2.6 and 5 GHz (shaded blue region). Modes of other symmetries are shown in other colors and de-emphasized. The black dashed line marks the frequency of a mode that can be localized by a defect in the phononic crystal (see §3.1.3). **b,** Volumetric strain of the $k_x = 0$ mode in the band at the top edge of the bandgap, with exaggerated deformation.

### 3.1.3 Defect modes

Together with a photonic and phononic bandgap, the standard optomechanical crystal device must include a localized optical mode. This is accomplished with a "defect" in the photonic crystal, designed such that a mode may exist there that lies in the bandgap of the photonic crystal on either side, with the field profile decaying exponentially into the bandgapped regions. This can also be thought of as a sort of mirror cavity, with "mirrors" formed by the bandgapped regions. If the same defect also localizes a mechanical mode in the same way, these two modes can interact according to the coupling described in §2.1.1. Such a device may be called an optomechanical crystal.

A finite-element simulation of such an optomechanical crystal device is shown in

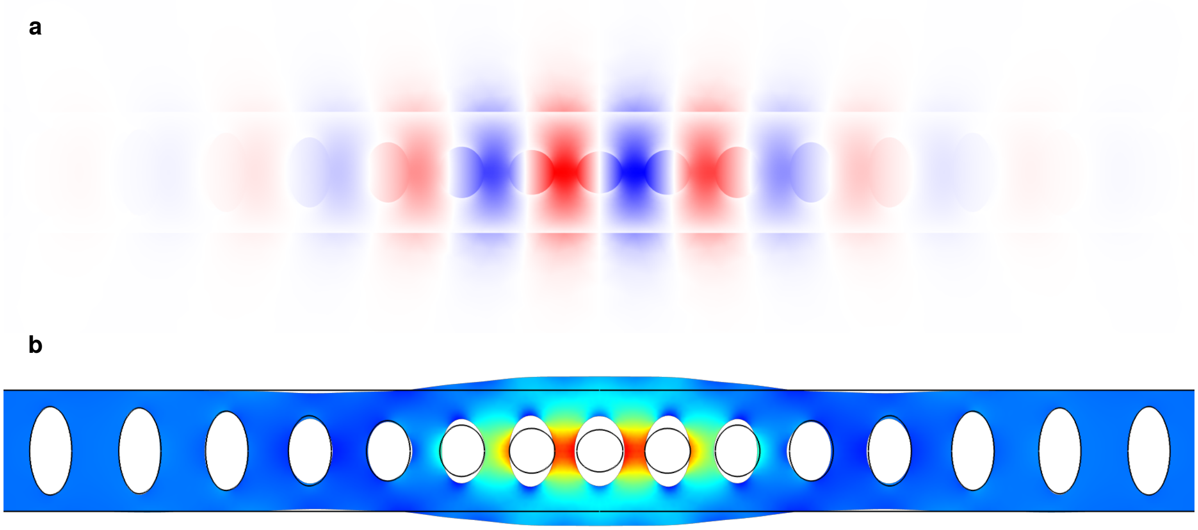

Figure 3.4: **Finite element simulation of a silicon optomechanical crystal nanobeam.** The “mirror” unit cell of Fig. 3.1 repeats for many periods beyond the edges of the plotted region. **a,** Electric field in the $y$ direction for the fundamental optical defect mode. **b,** Volumetric strain of the fundamental mechanical defect mode, with exaggerated “breathing-mode” deformation.

Fig. 3.4. The simulated single-photon optomechanical coupling is $g_0/2\pi \approx 1.1\,\mathrm{MHz}$, almost entirely due to the photoelastic effect. Typical devices that we have fabricated exhibit optical $Q_i > 10^5$, mechanical linewidth $\gamma/2\pi \approx 3\,\mathrm{MHz}$, and $g_0/2\pi$ between 700 and 900 kHz.

## 3.2 Engineered phonon leakage

In order to couple the localized mechanical mode of the nanobeam to a distant electromechanical transducer, we must allow mechanical energy to exit the nanobeam. If this energy leaks into a bath, it appears as an extrinsic increase $\gamma_{b,e}$ in the total mechanical loss rate

$$\gamma_b = \gamma_{b,i} + \gamma_{b,e}. \tag{3.8}$$

Patel et al. [42] introduce such “phonon loading” to a nanobeam optomechanical resonator by offsetting the holes from the nanobeam axis, coupling the symmetric mechanical resonator mode to an antisymmetric guided mode at the same frequency. By increasing this offset to 40 nm the mechanical $Q$ is tuned from an unperturbed value above $10^5$ to less than $10^4$, implying a loading of 0.643 MHz. The optical $Q$ is unaffected, and the optomechanical coupling $g_0$ is reduced by 10% at the largest offset, in agreement with a simulated reduction of 8%. There is also variation in the measured mechanical $Q$ between nominally identical devices by up to a factor of 10, which is attributed to fabrication disorder in hole dimensions and position with evidence from simulation.

A different strategy was identified in the previous generation of this experiment [58]. The optical bandgap is most sensitive to the period and filling fraction of the unit cell. Meanwhile, the mechanical mode of interest is most sensitive to the effective “stiffness” of the unit cell transverse to the nanobeam axis, which is primarily affected by the nanobeam width and hole width (in the $y$ direction as labeled in Fig. 3.1). The standard nanobeam design was modified to take advantage of this ability to control the mechanical and optical band structures somewhat independently. The defect modes were localized by unit cells with photonic and phononic band gaps, as usual, beyond which the unit cells transitioned into a “leaky” cell with a photonic bandgap and a guided acoustic mode.

These devices achieved a double-sided phonon loading of 1.5 MHz, as estimated by the increase in linewidth over that of devices with no leaky cells, while also leading to an increase in optical intrinsic loss rate of 25%.

### 3.2.1 How much is enough?

Recall the impedance-matching condition Eqn. 2.49, which tells us that the optimal mechano-electromechanical cooperativity for a fixed optomechanical cooperativity (when sideband resolved, with frequency-matched modes) is

$$\mathcal{C}_{\mathrm{me}}^{\star} = \mathcal{C}_{\mathrm{om}} + 1. \tag{3.9}$$

At room temperature, we have reached optomechanical cooperativity above 1 with some devices (with no electromechanical element). Using typical values for the loss in our mechanical and electromechanical resonances, we estimate

$$\mathcal{C}_{\mathrm{me}}^{(\mathrm{typical})} = \frac{4(G_{\mathrm{me}}/2\pi)^2}{(25\,\mathrm{MHz})(3\,\mathrm{MHz})}. \tag{3.10}$$

Thus the impedance matching condition suggests we should aim for $G_{\mathrm{me}} \sim 2\pi \times 6\,\mathrm{MHz}$, if we can do this without disturbing the optical $Q$ or optomechanical coupling.

For an eventual phonon-shielded device at cryogenic temperatures, we expect to see mechanical and electromechanical $Q$ improve, increasing both cooperativities; this could allow us to operate with fewer photons as well as smaller $G_{\mathrm{me}}$ (for smaller perturbations to the optomechanics) or larger $\gamma_{c,e}$ (for larger bandwidth; see §2.3.1) while maintaining cooperativities above 1.

In any case, we would like to be able to design a resonator to have phonon loading above 1 MHz and up to 10 MHz depending on the parameters achieved in the hybrid device. It would be possible to do this by exaggerating the offset design in Ref. [42], but as the offset increases, $g_0$ continues to suffer. Making a large leakage one-sided while preserving $g_0$ and optical $Q$ is also challenging, for both the offset and leaky-cell designs. Moreover, we ultimately want to couple the acoustic leakage to a symmetric mode of a membrane for transduction with an IDT (see §4.2), so we would prefer to couple to a guided nanobeam mode that is symmetric across the nanobeam axis, as with the leaky-cell but not the offset design.

## 3.3 A new design

Our new design accordingly modifies the leaky-cell design, introducing a smoother taper and continuous design parameters for tuning a one-sided mechanical loading while preserving optical $Q$ and optomechanical coupling.

The design parameters of the nanobeam describe three unit cells each with some elliptical hole shape and lattice constant:

- A "mirror" cell with a photonic and phononic bandgap for modes of the desired symmetry, which repeats on the side of the nanobeam far from the electromechanical membrane;

- A "waveguide" cell supporting a symmetric guided acoustic mode but retaining a photonic bandgap, which repeats on the side near the membrane;
- A "defect" cell at the center of the nanobeam.

Moving from the defect away from the membrane, the unit cells smoothly transition between the defect and mirror cells, following a polynomial taper. Moving from the defect toward the waveguide, a phononic barrier is formed by partially transitioning the defect cell into a mirror cell, followed by a transition to the waveguide cell. The extent of the partial transition is controlled by a "barrier height" parameter, allowing continuous tuning in design of the coupling between the localized mechanical mode and the mechanical waveguide. The distance of the barrier from the defect is optimized together with the barrier height to preserve the co-localization of the mechanical and optical modes despite the asymmetry of the nanobeam.

The optical and mechanical band structures of the waveguide cell are shown in Fig. 3.5 (while the mirror band structures are identical to that from Figs. 3.2 and 3.3). The simulated nanobeam is shown in Fig. 3.6. The key parameters extracted from simulation (phonon loading $\gamma_{b,e}$, optical $Q_i$, and optomechanical coupling $g_0$) are plotted in Fig. 3.7 for a sweep of barrier heights at two different barrier distances.

We find that this scheme allows us to design a nanobeam resonator with an engineered phonon leakage rate above 1 MHz without reducing optomechanical coupling $g_0$ or optical $Q_i$ (in both simulation and experiment) from that of the corresponding design with mirror cells on both sides.

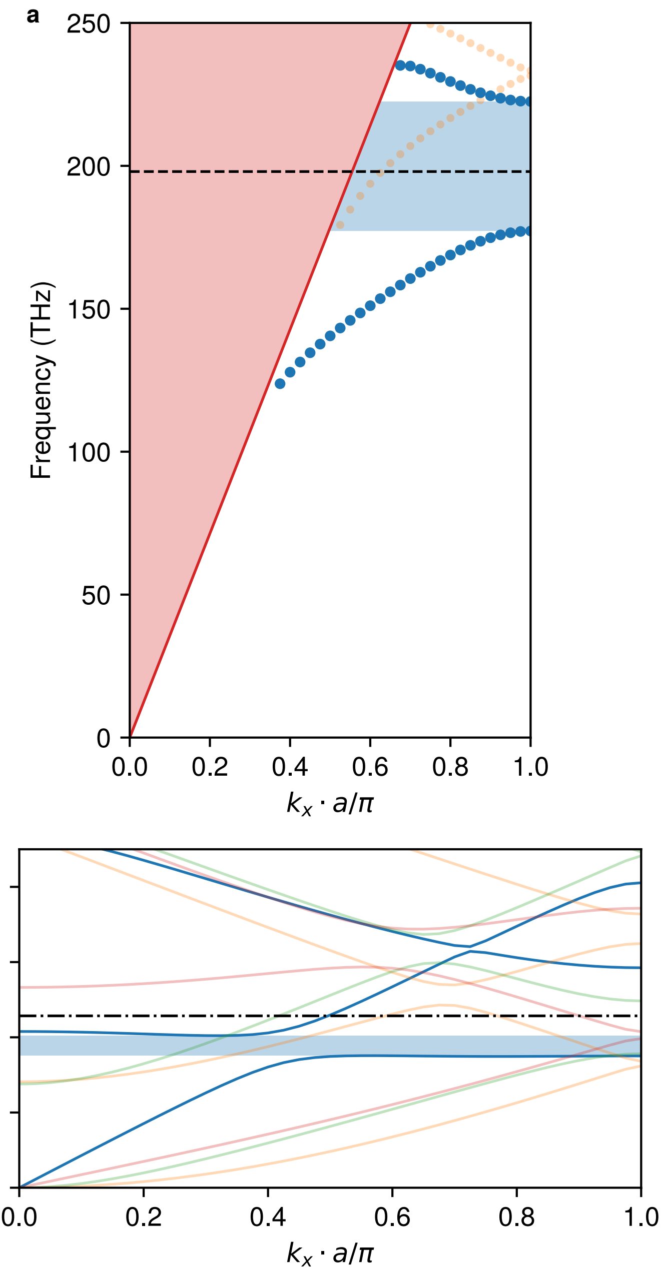

Figure 3.5: **Band structure of the nanobeam "waveguide" unit cell. a,** Optical band structure, showing a bandgap for the two lowest-frequency TE-like modes with $y$-inversion symmetry similar to that of the mirror cell (Fig. 3.2). The resonant frequency of the defect mode (black dashed line) still falls in the bandgap. **b,** Mechanical band structure, showing a guided mode of the correct symmetry at the defect-mode frequency.

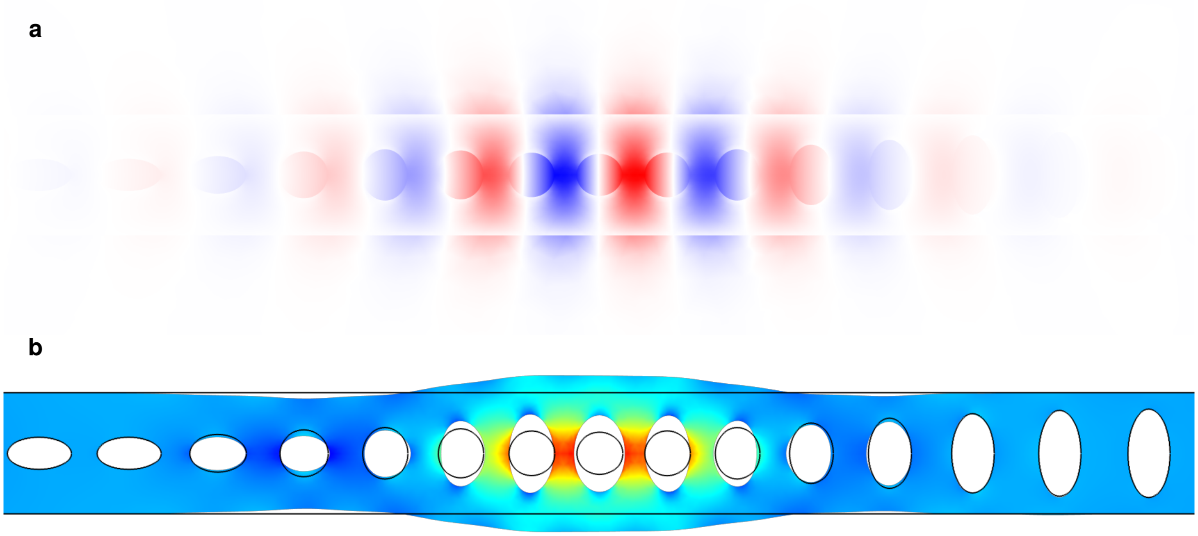

Figure 3.6: **Finite element simulation of a leaky silicon optomechanical crystal nanobeam.** The mirror unit cell of Fig. 3.1 repeats for many periods beyond the right edge of the plotted region, while the waveguide unit cell repeats on the left. **a,** Electric field in the $y$ direction for the fundamental optical defect mode. **b,** Volumetric strain of the fundamental mechanical defect mode, with exaggerated "breathing" deformation.

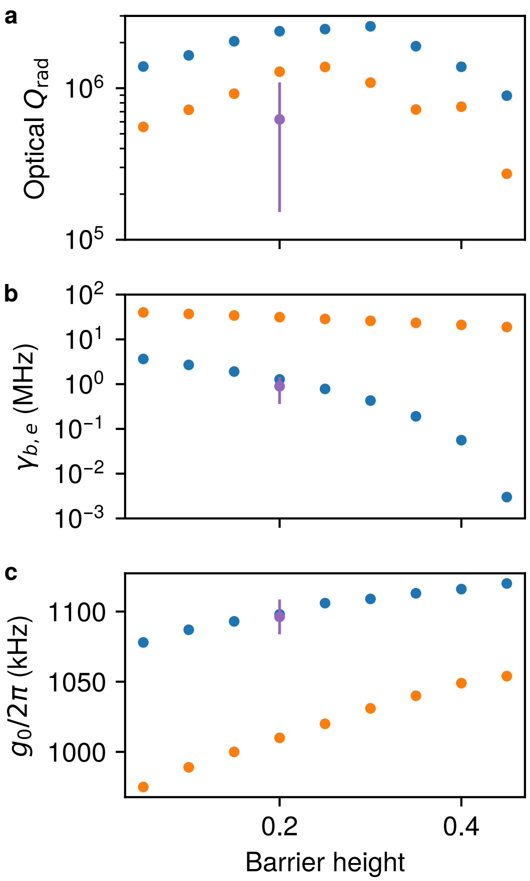

Figure 3.7: **Key figures of merit for the modified nanobeam.** The barrier height is varied for a barrier-peak distance of 3 unit cells (blue dots) and 2 unit cells (orange dots) from the defect. Random geometric errors in hole positions and diameters, normally distributed with $\sigma = 1\,\mathrm{nm}$, are also simulated for barrier height 0.2 and distance 3 unit cells, with median and 90% range shown in purple. **a,** Simulated optical $Q$ (including only radiative loss) is mainly affected by the mechanical loading at a level beyond our practically achievable $Q_i \sim 3 \times 10^5$, as desired. As with the non-leaky nanobeam, random geometric errors still have a large effect. **b,** Mechanical loading can be tuned from below 0.1 MHz to over 30 MHz, with some variation due to random errors in geometry. **c,** Optomechanical coupling is worse for leakier mechanics, but for a barrier height 0.2 and distance 3 unit cells it is the same as for the corresponding non-leaky nanobeam, at $g_0/2\pi = 1.1\,\mathrm{MHz}$.

### 3.3.1 Random geometric perturbations

The simulated optical $Q$, which accounts only for radiative loss, remains over $2 \times 10^6$ for selected parameters. As with our non-leaky nanobeams, this $Q$ is well above our maximum measured $Q_i$ of $3 \times 10^5$. However, if we include in our simulations a random variation in hole position and diameter, normally distributed with standard deviation 1 nm (realistic or slightly optimistic compared to variation measured by SEM), the optical $Q$ significantly suffers. The purple ranges in Fig. 3.7 show the 5th through 95th percentile of an ensemble of simulated devices. This suggests that our measured $Q_i$ may in fact be affected by radiation.[4] Some variation is also introduced to the mechanical loading and optomechanical coupling.

Additionally, the dimensions of features in the actual device have some geometric bias relative to the nominal pattern, introduced during exposure, development, or etching. This bias can be measured by scanning electron microscopy and is typically on the order of 5 nm. It may drift on a timescale of months due to aging resist or changes in the electron-beam lithography tool. Once characterized, the bias can be corrected in the pattern, or the biased pattern can be simulated itself, resulting in a correction to expected frequencies, quality factors, and $g_0$.

The measured room-temperature mechanical quality factor of several nominally iden-

---

[4] This then indicates process development or design efforts to reduce such errors or their effects would be worthwhile. A key technique for reducing edge roughness and critical dimension nonuniformity in e-beam lithography is multipass writing, where the same pattern is exposed multiple times at different positions in the write field, averaging out errors. Unfortunately, our attempts to do this with our electron-beam lithography tool have so far failed, apparently due to hardware problems causing misalignment on successive passes.

tical leaky nanobeams (with different unit cells than what was simulated for Fig. 3.7) varies between 400 and 1600, where $\gamma_{c,e} \approx 2\pi \times 3\,\mathrm{MHz}$ was targeted and $Q_i = 1600$ or an intrinsic linewidth around 3 MHz is typical of a non-leaky nanobeam at room temperature. It may be possible to make the design more robust against fabrication disorder by additionally tapering the nanobeam width. Controlling the mechanical band structure with continuous geometric variation may average out the effects of errors more effectively than this design, which relies on a small number of discrete hole shapes and positions.

### 3.3.2 The double nanobeam

The phonon loading of this design can also be tested by attaching the waveguide end to a mirror-image nanobeam. In simulation, this produces hybridized mechanical modes with a frequency splitting equal to twice the loss rate of the nanobeam leaking into a membrane, as expected for two identical resonators with a coupling equal to that loss rate. These resulting modes are shown in Fig. 3.8a.

We should then be able to address each of these mechanical modes optically through a waveguide coupled to only one nanobeam. Each mode would have an optomechanical coupling reduced from the single-nanobeam optomechanical coupling by a factor of $\sqrt{2}$, as well as a mechanical linewidth equal to that of a nanobeam with mirrors on both sides. In practice, variation in fabrication often causes frequency differences between nominally identical modes larger than the splitting expected from the coupling between them. In such cases the hybridized modes are unequal superpositions of the modes local to each

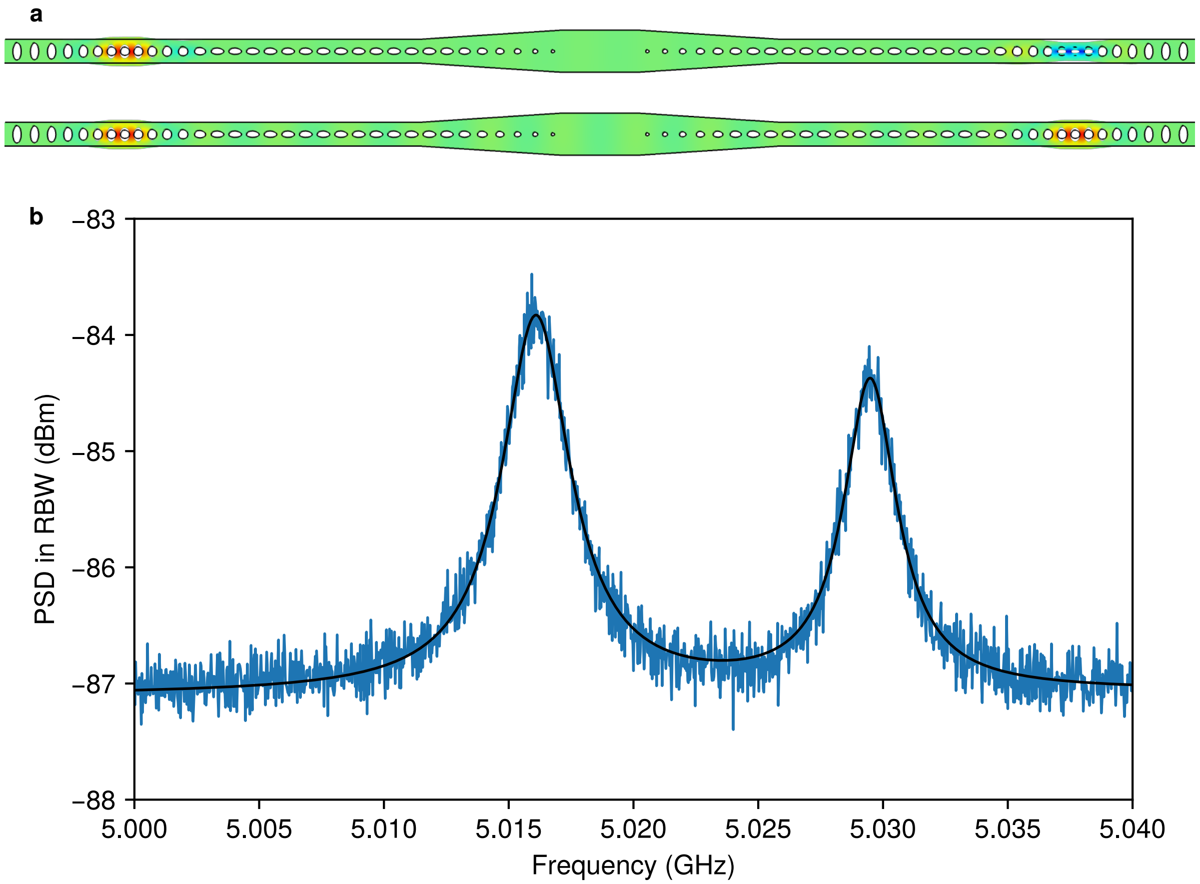

Figure 3.8: **Double nanobeam configuration. a,** Volumetric strain of the antisymmetric and symmetric hybridized modes of two coupled nanobeams, with a frequency splitting twice the coupling between nanobeams. **b,** Noise peaks (fit to Lorentzians) in the RF power spectrum of light transmitted through the right nanobeam optical cavity, due to interaction with the thermal mechanical motion of each mode, showing a splitting of $\Delta f = 13\,\mathrm{MHz}$.

nanobeam, and by probing one nanobeam we see one mode much more strongly than the other.

In some measured double-nanobeam devices we do see a fairly equal splitting, as with one device with a mode at 5.016 GHz and another at 5.029 GHz. The optomechanical couplings are $g_0 \approx 2\pi \times (490\,\mathrm{kHz}, 335\,\mathrm{kHz})$, while damping rates are $\gamma_b \approx 2\pi \times (2.8\,\mathrm{MHz}, 2.2\,\mathrm{MHz})$, obtained from fits to the RF power spectrum of transmitted light (Fig. 3.8b; see Ref. [20]). The splitting is not quite equal, indicating some bare frequency difference combined with coupling between modes slightly less than $\Delta f/2 = 6.5\,\mathrm{MHz}$. An equivalent single nanobeam had $g_0 \approx 2\pi \times 723\,\mathrm{kHz}$ (more than the expected factor of $\sqrt{2}$ larger) and a linewidth of 7.5 MHz implying a loading of 5 MHz. Roughly balanced splittings up to $\Delta f = 20\,\mathrm{MHz}$ were measured in other devices. This indicates that we can reach larger phonon loadings with this design without merely dumping phonons into a bath, although more reliable fabrication processes and designs more robust to error will still be valuable.

# Chapter 4

# The electromechanical element

In the previous chapter, we described the design of the optomechanical component of our device. This design included a means to allow microwave-frequency mechanical waves to leak into or out of an optomechanical nanobeam, so that a separate component could couple that mechanical information with microwave-frequency electromagnetic fields. In this chapter, we describe this electromechanical component, which consists of an interdigital Lamb wave transducer on a piezoelectric bilayer membrane.

With our optomechanical design, we took advantage of the fact that the ratio of the speed of sound and light in silicon is comparable to the ratio of the desired mechanical and optical frequencies, allowing the wavelength-scale co-localization of the two modes. In the absence of such matching of wavelengths, we rely on a new set of ideas for the electromechanical transducer coupled to the optomechanical nanobeam.

## 4.1 Piezoelectricity

In §2.1.1, we described the origin of the optomechanical coupling in the photoelastic and moving dielectric boundary effects. Both of these are quadratic in the electromagnetic fields; any strain-field interaction linear in the optical field would be averaged to zero on the timescale of the deformation of the dielectric. While silicon also exhibits such quadratic interactions at microwave frequencies (for essentially the same reasons), they are weaker than is practical for our aims, particularly without the ability to enhance the interaction by tightly co-localizing the modes.

Working with microwave-frequency electromagnetic fields, however, means that the crystal lattice is able to deform on the same timescale as the electric field oscillations, rather than requiring a microwave-frequency beat between two optical tones. We can thus take advantage of potentially much stronger linear interactions between the electric field and material strain.[1]

The first-order coupling between strain and electric field is known as the piezoelectric effect, and is described by the constitutive relations [4]

$$D_i = \varepsilon_{ij}^{T} E_j + d_{ijk} T_{jk}, \tag{4.1}$$

$$S_{ij} = d_{ijk} E_k + s_{ijkl}^{E} \varepsilon_{kl}^{T}. \tag{4.2}$$

---

[1] In general, we expect first-order terms to dominate higher-order nonlinearities, as long as they arise from the same physical perturbation and the first-order effect is not prohibited by symmetry. Both the piezoelectric and electrostrictive (photoelastic-analogue) effects can be seen as arising from a redistribution of charge under lattice deformations, changing the electric polarization density and susceptibility (polarization response to applied field) of the crystal, respectively. On symmetry, see the next footnote.

Here $\mathbf{D}, \mathbf{E}$, and $\varepsilon$ are the electric displacement field, electric field, and permittivity; $\mathbf{T}, \mathbf{S}$, and $\mathbf{s}$ are the stress, strain, and compliance; and $\mathbf{d}$ is the piezoelectric tensor in "strain-charge" form. The superscripts $T$ and $E$ denote coefficients determined at constant stress and electric field, respectively, so that we can use these equations to directly calculate $\mathbf{D}$ and $\mathbf{S}$ with $\mathbf{E}$ and $\mathbf{T}$ as the independent variables. For $\mathbf{d} = 0$ we recover the usual stress-strain and electric displacement relations. The addition of piezoelectricity allows an electric field to produce strain or for stress to produce polarization. (These equations can be rearranged for other choices of independent variables.)

Silicon itself exhibits no piezoelectric effect.[2] Instead, we combine the silicon we use for optomechanics with the piezoelectric material aluminum nitride (AlN), depositing the AlN with a sputter tool and removing it everywhere except the region where the electromechanical resonator is defined. This electromechanical region is eventually mechanically released along with the nanobeam by etching away a buried oxide layer, forming an AlN/Si bilayer membrane.

## 4.2 Surface acoustic wave devices

Surface acoustic waves (SAWs) propagate along the surface of a solid with a displacement field profile that decays exponentially into the bulk. Although the electromechanical part

---

[2] This can be understood in terms of its crystal symmetry. Specifically, the (diamond cubic) crystal lattice (and hence the tensor describing the piezoelectric response) is symmetric under inversion (sending position $\mathbf{x}$ to $-\mathbf{x}$). An electric field changes sign under inversion, while a strain does not. Applying inversion to both sides of Eqn. 4.2 with zero stress implies the strain resulting from any applied field must be equal to its opposite, so $\mathbf{d} = 0$. More simply, in a one-dimensional picture, the linear piezoelectric effect wants the crystal to expand for a field pointing up and contract for a field pointing down. But those fields are the same to an inversion-symmetric crystal.

of our device, which involves a thin, mechanically suspended membrane rather than a semi-infinite substrate, is not strictly a SAW device, its design and analysis inherits a great deal from work on the physics and engineering of surface acoustic wave devices.

SAW devices are commonly used in signal processing applications (for example, as radio-frequency filters). The low speed of sound compared to that of light allows very compact elements with good control over frequency response through simple designs. Much more detail on SAW devices can be found in the texts [15, 22, 39], which are all useful references and complement one another in both material covered and perspective. Recent experiments have also investigated the use of SAWs for quantum applications as well as SAWs themselves in the quantum regime [53, 16, 7, 21, 36, 54].

### 4.2.1 Membrane acoustic waves

A infinite plate, uniform in the $y$ direction and with some thickness $d$ in the $z$ direction, supports two families of $x$-propagating waves, which we label $S_i, A_i$ $(i \geq 0)$ [31]. These are known as Lamb waves, where $S$ (symmetric) and $A$ (antisymmetric) denote their out-of-plane-axis inversion symmetry.[3]

The $S_0$ and $A_0$ modes exist at all frequencies. A useful parameter when thinking about their behavior is the ratio of thickness to wavelength, or an equivalent scale parameter independent of the mode choice. We consider the thickness-frequency product $d \cdot \Omega$

---

[3] There are also membrane shear modes, which have nonzero displacement amplitude in the $y$ direction. For the most part, we can ignore these, since our electromechanical component is effectively uniform in the in-plane direction transverse to wave propagation, although they may appear where the membrane and nanobeam are joined.

compared to a typical wave speed, using the bulk shear velocity $v_s$ for concreteness.

When $d \cdot \Omega / v_s$ is large, the $S_0$ and $A_0$ waves approach symmetric and antisymmetric superpositions of traditional surface acoustic waves (Rayleigh waves) on the top and bottom of the plate.

When $d \cdot \Omega / v_s$ becomes small, the $S_0$ wave propagates at a higher velocity and becomes non-dispersive. It looks more like a bulk longitudinal wave with out-of-plane breathing motion than a Rayleigh wave (which is more like a bulk shear wave). Meanwhile, the $A_0$ wave becomes like a flexural mode, and its phase velocity falls toward zero. The higher-order modes also each have a cutoff at low enough $d \cdot \Omega / v_s$.

In a bilayer membrane, there are analogous fundamental modes which we will still call the $S_0$ and $A_0$ Lamb waves (Fig. 4.1). We are below the cutoff for all other modes at the thickness and frequencies we work with.

### 4.2.2 Interdigital transducers

A SAW or Lamb wave in a piezoelectric substrate has an associated electrical component, which can be addressed using electrodes patterned on the surface of the substrate. An interdigital transducer (IDT) is an array of signal and ground electrodes matched to the acoustic wavelength at a certain frequency, acting like an array antenna for such a wave (Fig. 4.2). Electrically driving the IDT at that frequency will generate outgoing acoustic waves in each direction, while the IDT will pick up an electrical signal from incoming acoustic waves. An IDT is sometimes described by its wavelength or period

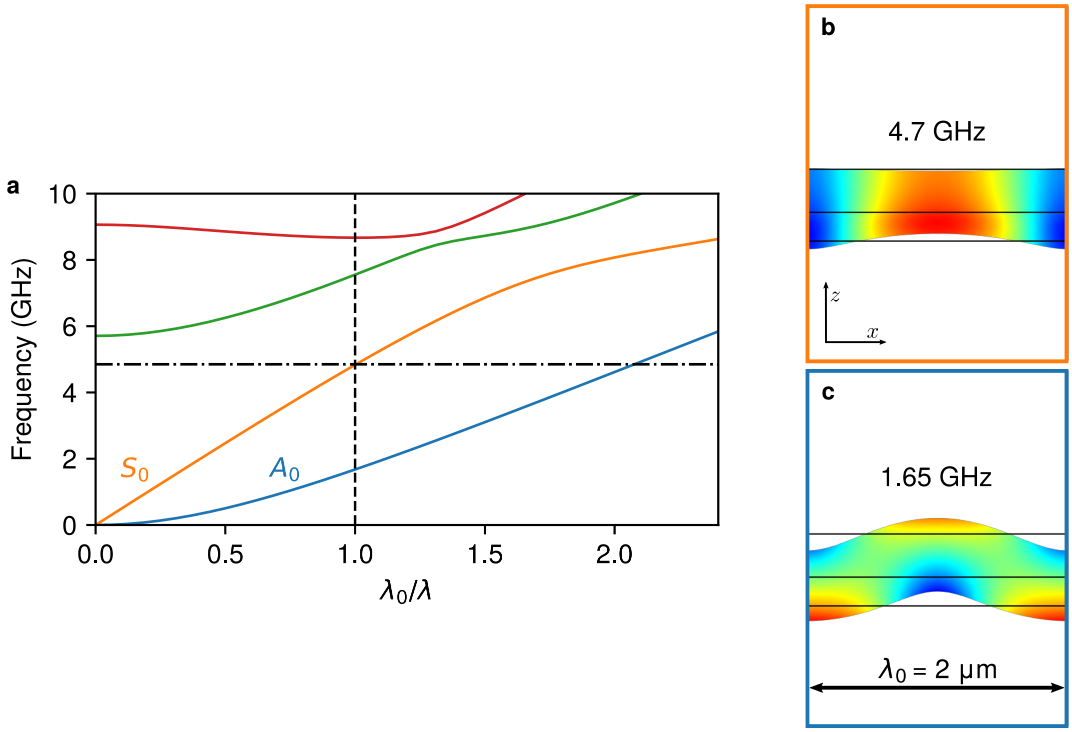

Figure 4.1: **Lamb waves in a bilayer membrane,** for 330 nm AlN on 220 nm Si. **a,**: Dispersion diagram for Lamb waves in a 330 nm/220 nm AlN/Si membrane. The horizontal axis is scaled by $\lambda_0 = 2\,\mu\text{m}$. At 4.7 GHz (horizontal dash-dot line), only the $A_0$ and $S_0$ modes are present. For wavelength $\lambda_0$ (vertical dashed line), the $S_0$ and $A_0$ modes are around 4.7 GHz and 1.65 GHz. **b,** Volumetric strain profile of $S_0$ Lamb wave with $\lambda = \lambda_0$. **c,** Strain of $A_0$ Lamb wave.

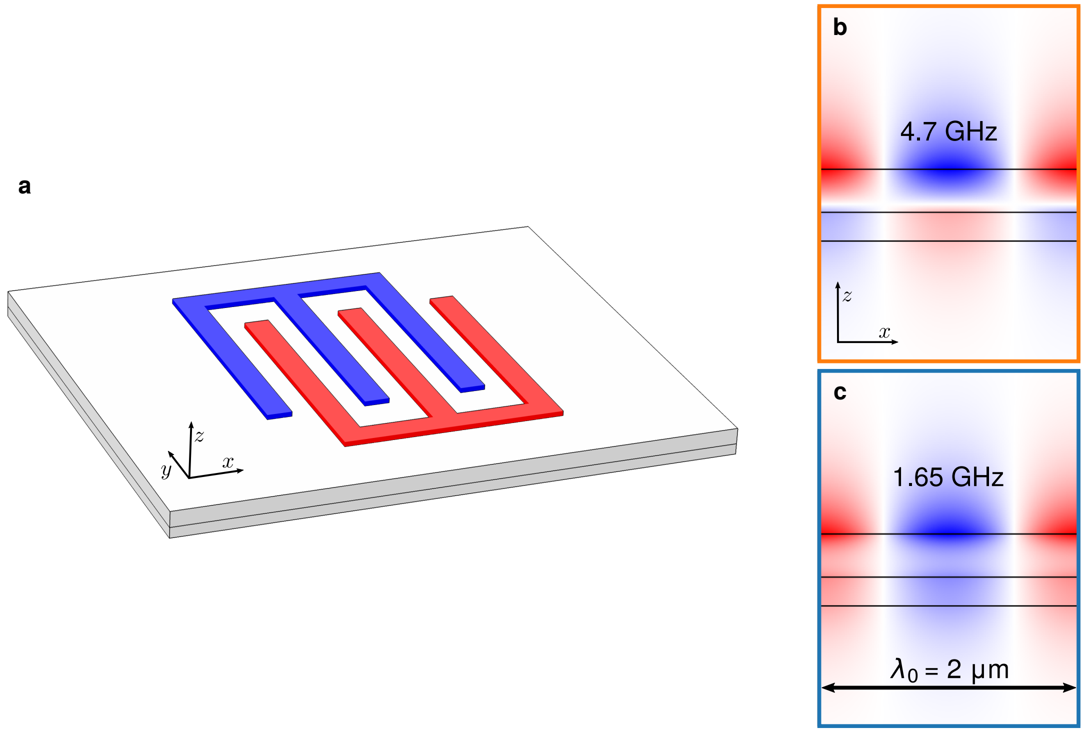

Figure 4.2: **Interdigital Lamb wave transducer. a,** 3D schematic of interdigital signal and ground electrodes on a bilayer membrane. **b,** 2D cross section of voltage for one wavelength of the $S_0$ Lamb wave of Fig. 4.1b. **c,** Voltage of $A_0$ Lamb wave.

(length of the repeating signal-ground unit cell) or pitch (center-center distance between adjacent electrodes); for our 'regular' IDT with equally spaced alternating signal and ground electrodes, the pitch is half the period (and the electrode width is half the pitch).

We design our device to couple to the $S_0$ mode. As with standard SAW devices, an IDT will transduce a wave in a piezoelectric substrate when the acoustic wavelength is matched such that it produces an in-phase response at the signal electrodes. This now includes both $A_0$ and $S_0$ waves at different frequencies.

Any energy in the $A_0$ mode is expected to be lost before it is transduced, since at the $S_0$ operating frequency the $A_0$ mode is not phase-matched to the IDT. In our membrane, with an IDT period around 2 μm, the $S_0$ wavelength is matched around 4.7 GHz while the $A_0$ wave is matched around 1.65 GHz.[4]

The $S_0$ and $A_0$ waves are coupled by asymmetric perturbations to the membrane, including the IDT electrodes and a non-vertical sidewall at the membrane boundary. The IDT electrodes should be made as thin as possible, and the sidewall as vertical as possible, to reduce this unwanted coupling.

Besides the presence of the $A_0$ and potentially other Lamb waves (and the absence of bulk modes to scatter into), the analysis of a Lamb wave transducer is essentially analogous to that of a standard SAW device. The main further modification is that the membrane thickness introduces an intrinsic length scale, as seen in Fig. 4.1: unlike Rayleigh waves, Lamb waves are dispersive, being affected by the ratio of thickness to wavelength.[5] This leads to some additional design considerations, which we defer until §4.3.

### 4.2.3 Equivalent circuits

An IDT can be described by an equivalent circuit consisting of the interdigital capacitance $C_0$ due to the electrode geometry in parallel with a frequency-dependent acoustic admittance $Y_a(f)$ (Fig. 4.3). Power dissipated by the real part of the acoustic admittance

---

[4] Waves can also be phase-matched to a regular IDT with an odd number of wavelengths per IDT period. Fortunately, the $A_0$ wave at 4.7 GHz with approximately two wavelengths per IDT period is nearly invisible to the IDT, since that wave applies the same electrical drive to both the signal and ground electrodes.

[5] In practice all SAW devices have some finite electrode thickness, which also introduces scale dependence. In particular, SAW devices that rely on the mechanical reflectivity of the electrodes (or metal-strip Bragg mirrors) cannot easily be scaled from MHz to GHz frequencies by shrinking the electrode lithographic pattern without considering the electrode thickness compared to the wavelength.

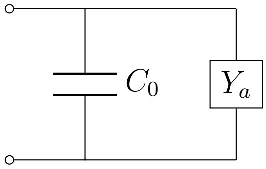

Figure 4.3: **Equivalent circuit for an interdigital transducer,** consisting of a geometric capacitance $C_0$ in parallel with an acoustic admittance $Y_a(f)$.

corresponds to power radiated as acoustic waves.

The frequency response of an IDT can be understood intuitively as related to the discrete Fourier transform of the time-domain sampling of a SAW passing under it (the "tapped delay line" picture). With regularly spaced, equally weighted fingers, we are sampling a rectangle function in the time domain. This becomes a sinc function in the frequency domain, whose width is inversely proportional to the number of IDT periods.

We are thus not surprised to find that $\mathrm{Re}[Y_a]$ has a $\mathrm{sinc}^2$ frequency dependence around the frequency $f_0$ of the fundamental wave matched to the IDT period; we quote the result from Ref. [39]:

$$\mathrm{Re}[Y_a(f)] \approx \mathrm{Re}[Y_a(f_0)] \left( \frac{\sin\left(\pi N_p (f - f_0)/f_0\right)}{\pi N_p (f - f_0)/f_0} \right)^2 \tag{4.3}$$

Here $N_p$ is the number of periods in the IDT, and the fractional bandwidth of the response is seen to be roughly the inverse of $N_p$. The peak conductance $\mathrm{Re}[Y_a(f_0)]$ grows with the IDT capacitance, number of periods, and effective piezoelectric strength.[6]

---

[6] The piezoelectric strength is usually described by a number $k^2_{\mathrm{eff}}$, which can roughly be interpreted as the fraction of total (strain and electromagnetic) energy in the electric field for a deformation of the piezoelectric material, and it depends on the mode and thickness-frequency product for a Lamb wave transducer (see §4.3).

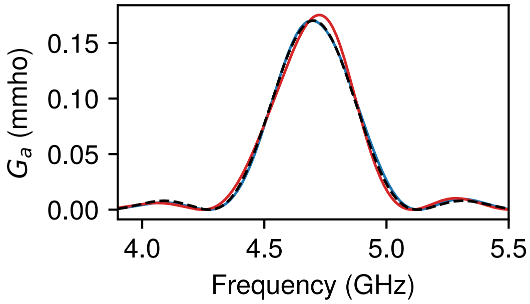

Figure 4.4: **Acoustic conductance $G_a(f) = \mathbf{Re}[Y_a(f)]$ of an interdigital Lamb wave transducer.** The 2D (plane-strain approximation) finite element simulation of an IDT with 10 periods and 30 µm aperture (solid blue line) agrees well with the simple model for a traditional SAW device quoted in Eqn. 4.3 (black dashed line). When including 20 nm aluminum electrodes in the mechanical simulation, there is some distortion of the response due to internal reflections in the IDT (solid red line).

This can be used to model a Lamb-wave IDT just as well as a Rayleigh-wave IDT in the absence of reflections by the IDT electrodes (Fig. 4.4).[7]

### 4.2.4 IDTs in resonators

An IDT can be placed in a “mirror cavity” that supports acoustic resonances, in analogy to an optical Fabry-Perot resonator. In traditional SAW devices, each mirror is formed by a distributed Bragg reflector, usually consisting of one-dimensionally periodic strips of metal that create a bandgap for SAWs (see §3.1.2 and Footnote 3 in the previous chapter). A useful tool for calculating the electrical and acoustic response for such a device is the $P$-matrix, which allows the combined modeling of IDTs, mirrors, and other elements by relating acoustic and electrical ports with a hybrid admittance/scattering

---

[7] These reflections internal to the IDT can still be modeled, for example using the coupling-of-modes equations presented in Ref. [39].

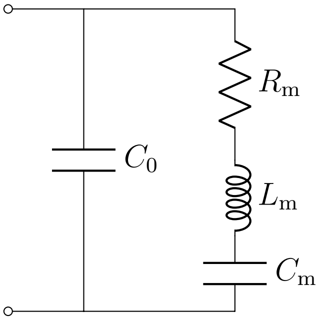

Figure 4.5: **Equivalent circuit for an IDT-coupled electromechanical resonance,** consisting of a geometric capacitance $C_0$ in parallel with an $RLC$ resonance.

matrix [39].

For a device on a membrane, an acoustic mirror may be conveniently formed by simply terminating the membrane. For a short enough cavity, if the IDT is correctly placed, it will couple strongly to a single resonance of the cavity. The acoustic admittance (which describes a steady-state response) near resonance is sharpened and enhanced according to the number of passes made by a traveling wave under the transducer before it decays. In the high-$Q$ limit, it turns out one can model the resulting electromechanical equivalent circuit near resonance as $C_0$ in parallel with a series $RLC$ resonator; the energy stored in the mechanical inductance $L_\mathrm{m}$ or capacitance $C_\mathrm{m}$ is the electromechanical energy, and power dissipated in the mechanical resistance $R_\mathrm{m}$ corresponds to acoustic power lost.

### 4.2.5 External coupling and impedance matching

The coupling of a series $RLC$ resonator to a load has a simple description in terms of the real impedances of the resonator and the load, which dictate where energy is dissipated in the circuit as a whole [43]. The resonator has intrinsic damping and external coupling

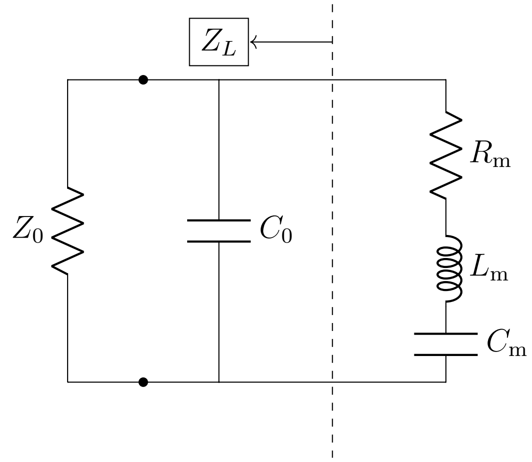

Figure 4.6: **Equivalent circuit for an IDT-coupled electromechanical resonance, loaded by some external impedance.** The external load may really be at the end of a matched transmission line. The series $RLC$ sees the impedance of the load and $C_0$ in parallel as $Z_L$, whose real part compared to $L_\mathrm{m}$ determines the extrinsic loss rate of the resonance.

rates

$$\gamma_i = \frac{R}{L}, \qquad \gamma_e = \frac{R_L}{L} \tag{4.4}$$

where $R_L$ is the real part of the load impedance seen from the resonator. In the case of the electromechanical $RLC$, which is connected over the geometric capacitance $C_0$ to a transmission line matched to a load with real impedance $Z_0$ (Fig. 4.6), the external coupling rate is

$$\begin{aligned}\gamma_e &= \frac{1}{L_\mathrm{m}}\mathrm{Re}\left(\frac{1}{1/Z_0 + i2\pi f_0 C_0}\right) \\ &= \frac{1}{L_\mathrm{m}}\frac{Z_0}{1+(2\pi f_0 C_0 Z_0)^2}.\end{aligned} \tag{4.5}$$

The actual device impedance will be more complicated, including for example embedding impedances from on-chip microwave lines or wire bonds. The acoustic and electrical parts can still be determined from electrical reflection measurements, producing an equivalent circuit amenable to the same analysis.

Of particular note is that this external coupling can be made large by changing the load resistance $R_L$ seen by the $RLC$. One may do this by inserting an impedance matching network between the IDT and load, designed following procedures described in Ref. [43].[8]

## 4.3 The piezoelectric bilayer membrane

When AlN is grown on silicon with the sputter tool, it grows in grains on a 10 nm scale (order-of-magnitude, determined by AFM) whose *c*-axes are approximately aligned normal to the wafer and whose in-plane orientation we expect to be random [9, 34]. Misalignment of *c*-axes, which can be quantified by x-ray diffraction, reduces the effective piezoelectric effect relative to that of single-crystal AlN. Our sputtered AlN, with (002) XRD peak full width at half maximum $< 2°$ in rocking curve measurements, appears to produce $k^2_{\text{eff}}$ (see Footnote 6) around a factor of 2 smaller than the value simulations predict for our IDT with ideal crystalline AlN.

Thicker AlN can significantly increase the effective electromechanical coupling of an

---

[8] It is similarly possible to match a non-resonant IDT to a source or load over some frequency range, so that all incident electrical power is converted into acoustic power, or half of the power incident on one acoustic port is converted to electrical power (for a bidirectional IDT). The required inductance and capacitance, given the non-resonant acoustic admittance for a device like ours, should be feasible with on-chip superconducting elements.

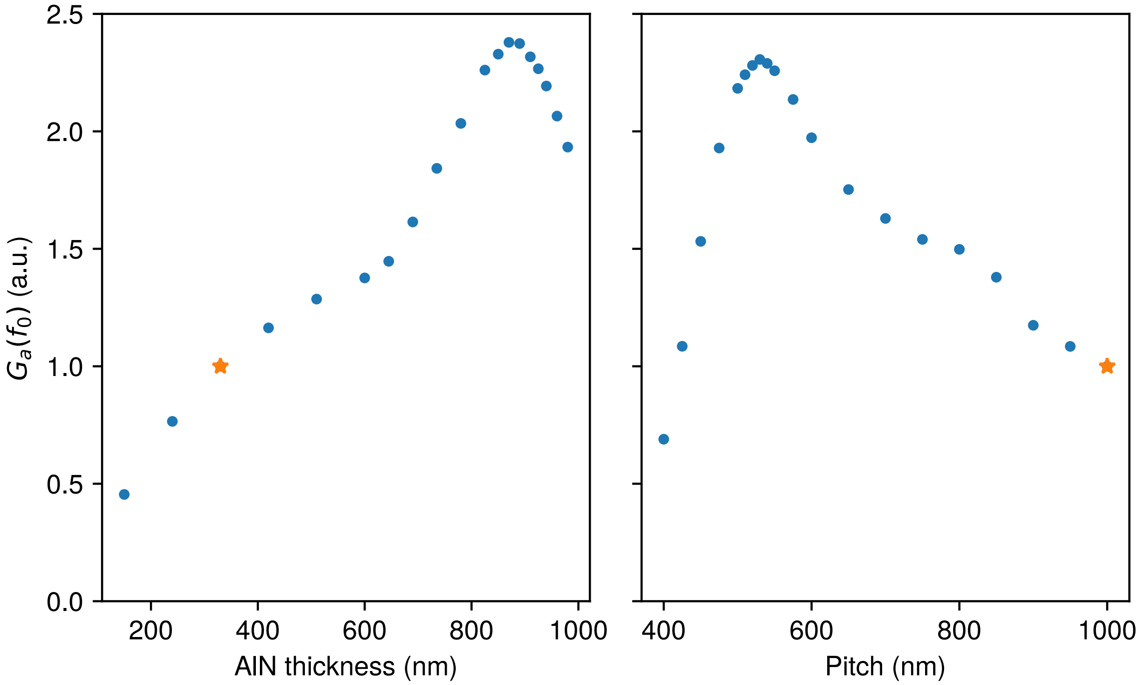

Figure 4.7: **Wavelength-thickness ratio tuning.** Peak acoustic conductance is plotted from 2D plane-strain finite element simulation using a rectangular IDT with 10 finger pairs. Actual device parameters are marked with a star. Effective electromechanical coupling at the center frequency is enhanced as the thickness approaches one half wavelength (although the center frequency is not held constant). **Left**: Varying AlN thickness with fixed 1 µm electrode pitch. **Right**: Varying electrode pitch with fixed 330 nm AlN thickness.

IDT, both because of better *c*-axis alignment at higher thicknesses and because of a resonance-like effect as the membrane thickness approaches roughly half the IDT wavelength. Simulation predicts that increasing the AlN thickness to 880 nm would increase the maximum real admittance of an IDT, via the latter effect, by roughly a factor of 2.5 (Fig. 4.7). Alternatively, moving to a shorter acoustic wavelength with IDT pitch 0.55 µm could increase the peak admittance by a factor of 2.5 while increasing the frequency to around 7.5 GHz.

In practice, the thickness is constrained because thicker AlN places greater demands on the (timed) etch process and also presents a challenge for the transition between bare silicon and the AlN/Si bilayer (see §4.4.1). A 330 nm thickness was chosen for its consistency with processes developed for prior experiments using AlN on $SiO_2$ while still satisfying the new fabrication demands for AlN on Si.

While pushing the AlN thickness higher may be difficult, decreasing the IDT pitch would be feasible, since our electrode width of 500 nm (for a 2 µm wavelength) is well above the limits of electron beam lithography.

## 4.4 Putting it together

Two final problems arise in mode-matching the interface between the nanobeam and the membrane. The nanobeam uses only the silicon layer, while the IDT lives on the bilayer; we need to be able to transmit waves between the two regions while minimizing scattering into unwanted modes. Then, in addition to the difference in substrate, there is a natural geometric mismatch between the quasi-1D nanobeam and the quasi-2D membrane. The acoustic waves must be focused or tapered by some means.

### 4.4.1 The membrane bilayer transition

Our solution to the first problem is to make the transition between the bilayer and bare silicon as gradual as possible. To this end, we etch the AlN using a photoresist reflow process, creating a “ramp” between the bilayer and the bare silicon (Fig. 4.8.

We consider a bilayer $S_0$ wave generated by an IDT and incident on the ramp, where the wave in the other direction is assumed to be lost. We can calculate the conversion of power into the outgoing silicon $S_0$ mode through simulation. Some amplitude may be reflected, which can actually lead to an increase or decrease in transmitted power depending on the phase of the reflected wave at the IDT (so varying with frequency when the distance between the IDT and ramp is fixed). To be pessimistic, we quote the maximum decrease in transmitted power, but in an actual device the ramp could be positioned to minimize its effect on the membrane resonance. Additionally, some power will be converted to the silicon $A_0$ mode. This conversion is not strongly frequency-dependent.

We can consistently make the ramp around 1 µm long. In this case the maximum reflection is about 13% of the power transmitted into an infinite bilayer, and of the transmitted power, another 11% is converted into the $A_0$ mode (Fig. 4.9).

The fabrication of the ramp requires an AlN etch, which means it introduces a new problem by potentially etching the silicon. An etch stop layer between the AlN and the entire wafer could prevent that, but this has its own difficulties: the AlN etch consists of a strong physical etch component, so that selectivity is generally low; we would also later have to remove the etch stop over the photonics region (with high selectivity relative to Si) without delaminating the AlN. (In particular, this would mean that $SiO_2$ could not be used, as the final vapor HF release would undercut the AlN; we would have to introduce an entirely new material to our process.)

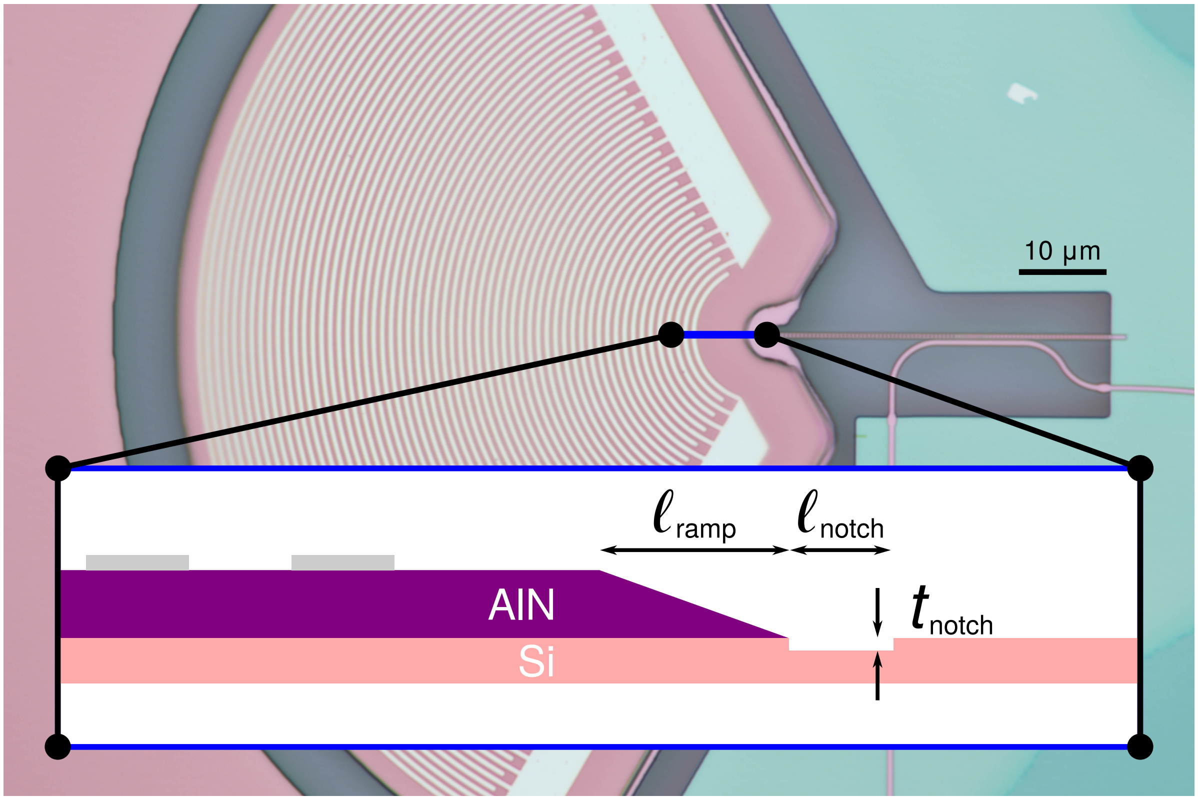

Figure 4.8: **Ramp and notch in membrane.** Optical microscope image of the interdigital transducer on the bilayer membrane. Inset: Schematic (not to scale) of 2D cross-section along blue line, showing the AlN "ramp" arising from etching with a reflowed photoresist mask and Si "notch" arising from a gap between the protected Si and the AlN during that etch.

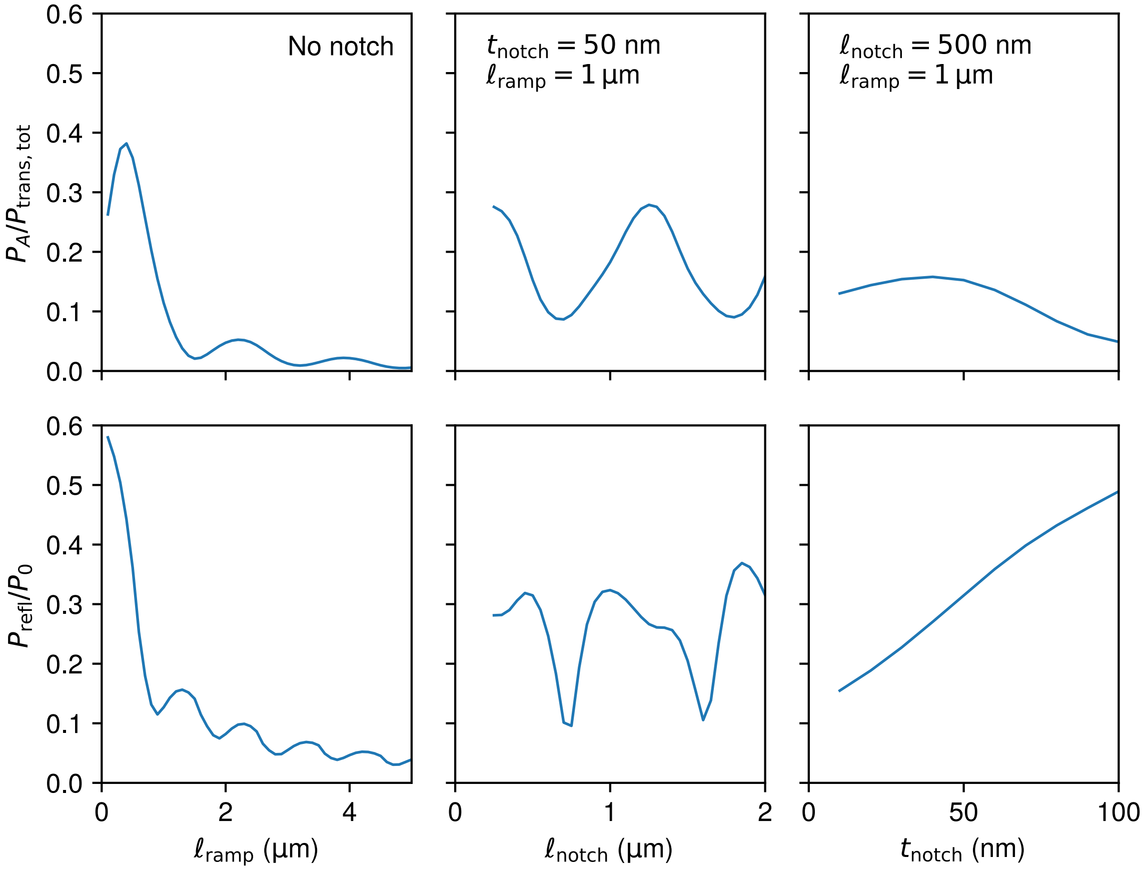

Figure 4.9: **Scattering of bilayer $S_0$ wave incident on transition to Si.** Results from finite-element simulation, varying ramp length $\ell_{\text{ramp}}$ with no notch (left), notch length $\ell_{\text{notch}}$ with a 50 nm depth and 1 µm ramp (middle), and notch depth $t_{\text{notch}}$ with a 500 nm length and 1 µm ramp (right). **Top**: Fraction of transmitted power in the $A_0$ Lamb mode. **Bottom**: Maximum reflected power, as a fraction of power transmitted in the absence of scattering.

The alternative that we select is to protect only the photonics region with an $SiO_2$ etch stop layer between the silicon and AlN. To prevent the end of the ramp from delaminating when the stop layer is removed, there is a gap between the edge of the stop layer and the end of the ramp. The silicon in this gap is etched, creating a “notch”. The notch depth can be limited by timing the AlN etch as well as possible. (The device in Ref. [57] had a similar notch, where the photonics region was protected during the etch defining the IDT fingers.) Again, we can determine from simulation the effect on the transmission of an $S_0$ wave.

The notch parameters depend on the timed AlN etch and the alignment of the various layers, so there is always some variation, but a typical notch is around 500 nm wide and 50 nm deep. Together with a 1 µm ramp, the notch only slightly increases the conversion to $A_0$ to 15%, but increases the maxiumum reflected power to 31% of transmitted power. The conversion and reflection depend sensitively on the notch length, which is near the $A_0$ wavelength of 700 nm (in a 220 nm silicon membrane at 4.7 GHz). At the minimum point we find below 10% each of reflection and conversion, which is actually slightly better than the ramp alone.

This is not ideal, but it is acceptable. To the extent that the power in unwanted modes or directions is lost before it can be transduced, this conversion does limit the $Q$ of resonances in the bilayer membrane; it also effectively turns some of the acoustic loading of the nanobeam mechanics into damping rather than coupling to the electromechanical resonance. There are specific reasons to remain optimistic. High efficiency can be obtained in the presence of loss (including coherent conversion to unwanted modes), as long as high cooperativities are still possible. Even so, we hope to increase the $Q$ of all modes in the entire suspended structure by surrounding it with a phononic crystal with a full bandgap and operating at cryogenic temperatures [35]. We also may not need to rely on a high $Q$ for the membrane, as long as the nanobeam can achieve high $Q$ and the membrane mode can be overcoupled to its microwave input by impedance matching. Still, these problems should be addressed as much as possible through design or process development.

### 4.4.2 Acoustic focusing

Our solution to the dimensionality problem consists mainly of using a curved IDT design as in Ref. [57]. That is, we choose to focus to a small spot (roughly the nanobeam width) rather than adiabatically taper the membrane width over a long distance. To this end we use a circular (or nearly circular) IDT finger pattern and a matching back mirror, by analogy to the hemispherical mirror cavity in Gaussian optics (with the nanobeam end as the flat mirror). We then modify this design in two significant ways to improve its performance.

#### Membrane anisotropy

The bilayer membrane has the property of in-plane acoustic anisotropy. While the AlN is isotropic in-plane due to random orientation of small grains, the (100)-cut crystalline silicon has a slightly higher sound speed in the <110> direction than in the <100>

direction. We can simulate the anisotropy of the bilayer membrane by approximating the AlN stiffness tensor as the stiffness averaged over in-plane rotations,[9] and find that the sound speed of the $S_0$ wave at 4.7 GHz varies by around 3% depending on propagation direction.

This directly spreads out the acoustic response over a 3% larger range of frequencies. Since the 3 dB bandwidth of an IDT with 30 finger pairs is also around 3% of the center frequency, the reduction in peak admittance will be less than 3 dB. There is also an effect on acoustic focusing and diffraction, as well as a complicated modification of the resonant mode pattern if the back edge of the membrane is not matched to wavefront of radiation from the nanobeam.

We can correct for both of these effects by adjusting the local IDT pitch to match the half-wavelength of a wave with phase-velocity vector in the direction of the focus; this has the effect that the waves generated at the design frequency from all sectors of the device interfere constructively at the focus, and that the IDT response to a radiating spot is phase-synchronous at all angles [32]. In Fig. 4.10 we show the anisotropic radiation pattern, marking the signal electrode curves for an IDT uncorrected or corrected for anisotropy.

A further small correction can be added for an area of bare silicon between the focus spot and the bilayer as in the actual device.

---

[9] This averaging procedure uses what is known as the Voigt model of polycrystalline materials, which assumes uniform strain throughout the grains. Averaging the compliance (the Reuss model, assuming uniform stress) gives a different approximation, and true elastic properties generally lie between the two [25]. Wurtzite AlN does not have especially dramatic acoustic anisotropy in this plane, so the method of approximation is not critical.

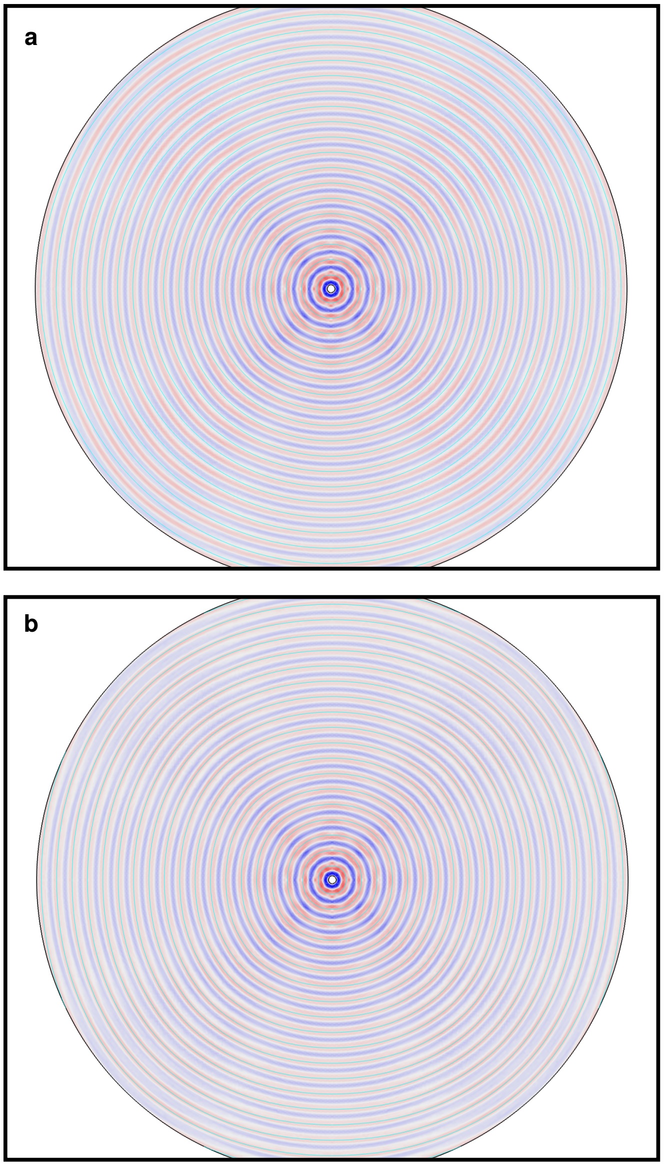

Figure 4.10: **Anisotropic acoustic radiation.** A circular spot on the bilayer membrane is excited, and the out-of-plane strain on the surface due to the $S_0$ Lamb wave is plotted. **Top**: Circular cyan contours every 2 µm. After about 15 wavelengths from the spot, the wave in <100> a direction (horizontal) is out of phase with the <110> (45°) wave on the contour. **Bottom:** Contours adjusted for anisotropic wave speed. IDT electrodes along these contours will respond to the radiation pattern from the spot with in-phase contributions from all angles, or generate a wave with constructive interference at the spot.

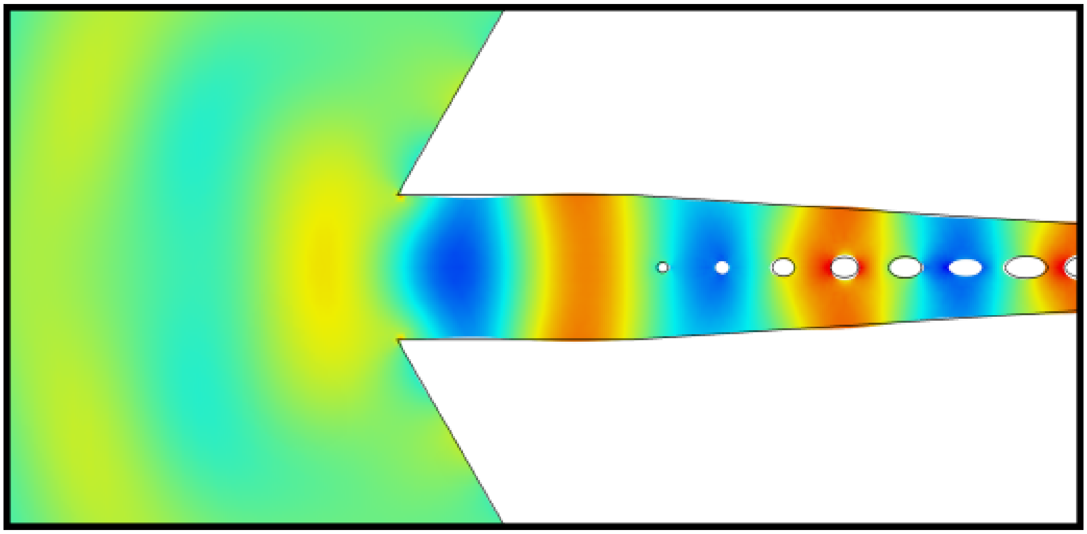

Figure 4.11: **Membrane-nanobeam connection.** The nanobeam is tapered to an unpatterned, wider geometry, then connected to the membrane with a large opening angle. Volumetric strain of the leakage from the nanobeam resonance of Fig. 3.6 is plotted, showing mostly the desired wave radiating into the membrane.

### The nanobeam-membrane boundary

For our design using an abrupt transition between the nanobeam and membrane, we can think of an outgoing wave in the nanobeam as scattering into some superposition of waves transmitted into the membrane and reflected into the nanobeam, determined by the overlap of the various mode shapes near the nanobeam-membrane boundary. The guided mode in the nanobeam mostly has the same shape as a focused $S_0$ Lamb wave, but it may also couple to in-plane shear modes in the membrane or modes guided along the edge of the membrane. These extraneous couplings are optimized in finite-element simulation by widening the nanobeam slightly before it meets the membrane and by connecting to the membrane with an opening angle of 240° (Fig. 4.11).

# Chapter 5

# Continuous and time-domain microwave-optical transduction

We have fabricated the device described in the previous chapters, combining an aluminum-nitride-based interdigital transducer (IDT) with a silicon-based one-dimensional optomechanical resonator. These elements together promise the necessary optomechanical and electromechanical coupling rates that would allow us to efficiently convert signals between infrared light and microwave electrical signals. We demonstrate bidirectional conversion of signals with internal efficiency above 1% and bandwidth above 3 MHz with a continuous blue-detuned pump. We then demonstrate time-domain microwave-to-optical transduction using a pulsed pump at both red and blue detunings.

## 5.1 Model of transduction

We model the transducer as described in Chapter 2, briefly restated here. The system consists of an optical mode and microwave-frequency mechanical and electromechanical modes, respectively labeled o, m, and e, each with their respective intrinsic loss and external coupling rates. The optical and mechanical modes are coupled by the optomechanical coupling $G_{\mathrm{om}} = \alpha g_0$, where $\alpha$ is the optical mode amplitude and $g_0$ is the single-photon optomechanical coupling. The mechanical and electromechanical modes are coupled with a fixed coupling $G_{\mathrm{me}}$.

The classical operation of this system can be described with input-output theory. We model our sideband-unresolved device with the system of input-output relations including the first sidebands on each side of the pump.

The microwave-to-optical transduction efficiency is defined as the ratio between the average output optical photon rate in the near-resonant sideband and the average input microwave photon rate, where the output refers the optical on-chip waveguide after the resonator, and the input refers to the microwave cable before the chip. The optical-to-microwave efficiency is defined in the reverse manner; we expect it to be equal to the microwave-to-optical efficiency at the same operating parameters.

The resulting on-chip efficiency is modeled by Eqn. 2.44, reproduced here:

$$\eta = \eta_{\mathrm{o}}\eta_{\mathrm{e}} \times 4\,\mathcal{C}_{\mathrm{om}}\mathcal{C}_{\mathrm{me}} \left|\Lambda_{\mathrm{em}}(\Omega)\Lambda^{\pm}_{\mathrm{opt}}(\Omega)\tilde{\Lambda}_{\mathrm{m,eff}}(\Omega)\right|^2, \tag{5.1}$$

using the definitions of Chapter 2. The sign is chosen to correspond to the near-resonant sideband (+ when blue detuned, − when red detuned).

In this experiment, we couple light onto and off of the device chip using focusing grating couplers with a per-coupler efficiency of 25%, resulting in an "external" efficiency $\eta_{\text{ext}} = 0.25\eta$.[1]

## 5.2 Device design and fabrication

The device, shown in Fig. 5.1b, is fabricated on a silicon-on-insulator substrate with 2 µm oxide and 220 nm device layer. A thin film of $SiO_2$ is deposited and patterned to protect the regions of silicon that will be used for photonic components. A 330 nm film of aluminum nitride is deposited then patterned using a photoresist reflow process and a timed etch. The protective $SiO_2$ acts as an etch stop over the photonic regions, so that bare silicon is only etched in a small gap between the AlN and protected region, with the overetch controlled by the etch time. The protective layer is then removed, and the nanobeam and grating coupler circuit are patterned by etching the silicon layer using a hydrogen silsesquioxane (HSQ) mask defined in electron-beam lithography. The IDT is patterned in a second electron-beam lithography step, using a poly(methyl methacrylate) (PMMA) bilayer as a liftoff mask. A release window is patterned in the silicon with photolithography, and the nanobeam and IDT membrane are then mechanically released

---

[1] The microwave port of the device is also connected to a microwave cable using a high-frequency probe with $< 1\,\text{dB}$ insertion loss and a resistive on-chip coplanar waveguide, but we do not factor these losses out in this distinction between on-chip and external efficiency.

by etching the buried oxide layer in hydrogen fluoride vapor.

The optomechanical nanobeam is designed as described in §3.3 to have an engineered phonon leakage rate above 1 MHz without reducing simulated optomechanical coupling $g_0$ from that of the corresponding non-leaky design.

An interdigital transducer with finger pitch approximately 1 µm is designed to couple to symmetric Lamb-like waves in the bilayer membrane around 4.7 GHz. The pitch is adjusted by up to 2% as a function of in-plane angle to correct for the acoustic anisotropy of the membrane [32].

The phononic waveguide is connected to the electromechanical membrane according to a design that reduces coupling to unwanted modes in the membrane. To reduce coupling to membrane shear and edge-guided modes, the nanobeam is widened to 1 µm and attaches to the membrane with a large opening angle. To reduce coupling to the antisymmetric Lamb-like mode of the bilayer membrane, the aluminum nitride is patterned using a reflow process to create a 1 µm-long ramp between the bilayer and bare silicon. From finite-element simulation we estimate that 15% of the power radiating into the membrane from the nanobeam is converted into these unwanted modes.

## 5.3 Experimental results

Measurements were performed in ambient conditions, with the experimental setup following the schematic in Fig. 5.1a.

From DC optical transmission as a function of wavelength, we find an optical mode

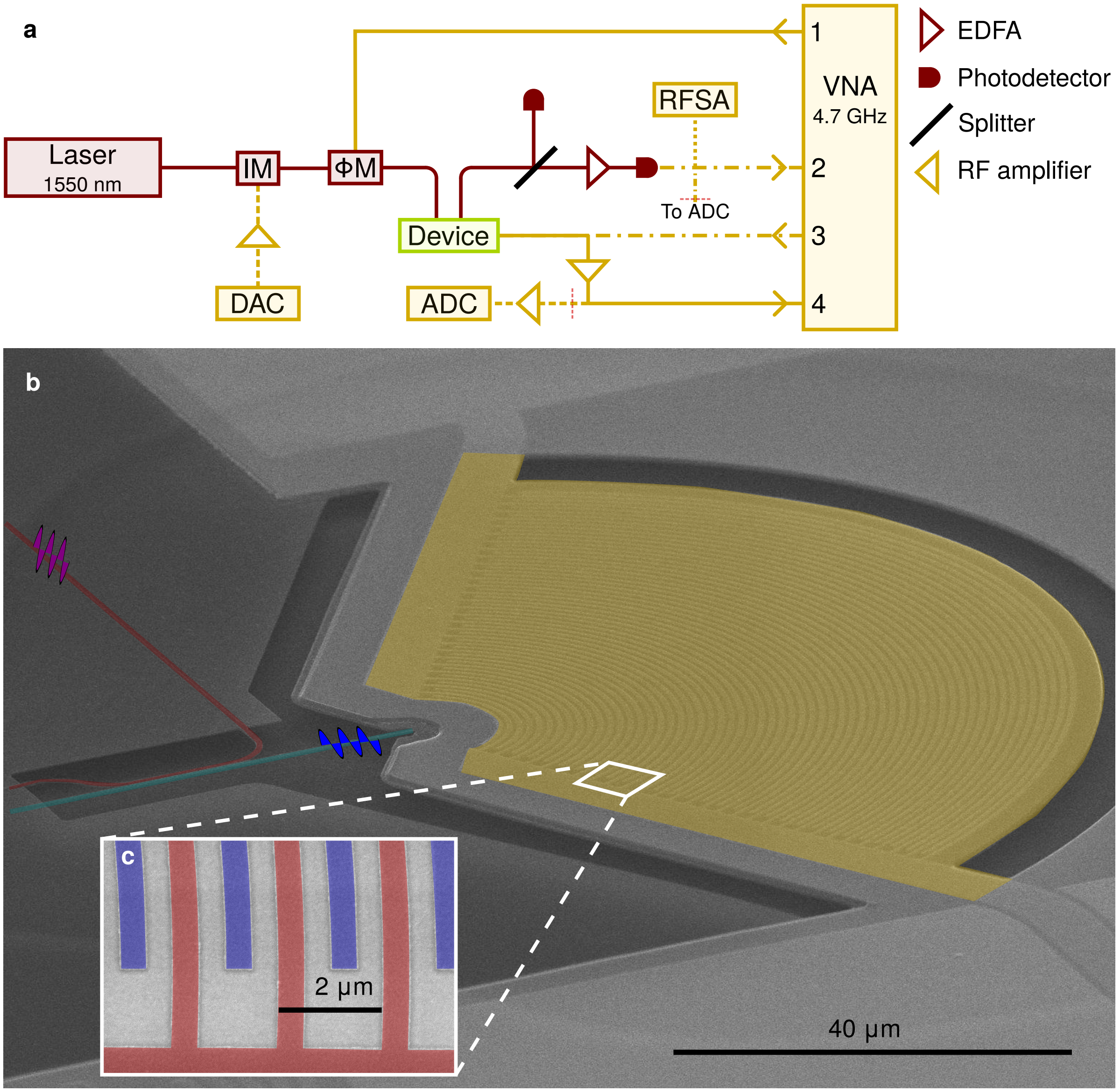

Figure 5.1: **Experimental setup and device. a,** Simplified measurement schematic, with microwave components in yellow and optical components in red. Solid lines are used for continuous optical-to-microwave transduction, and dashed or dotted lines are additional signal pathways used for other measurements. **b,** False-color SEM of a microwave-optical transducer, including photonic waveguide (red), optomechanical nanobeam (blue), and interdigital transducer (yellow). Inset **c,** magnified image of electromechanical transducer, showing signal (red) and ground (blue) electrodes.

at 1548 nm with intrinsic loss rate $\kappa_i = 2\pi \times (3.8 \pm 0.4)$ GHz and extrinsic loss rate $\kappa_e = 2\pi \times (6.5 \pm 0.3)$ GHz. From the noise peak in the RF power spectrum of the transmitted optical beat between the pump and mechanics-induced sidebands, we measure a mode at 4.737 GHz with full width at half maximum $(6.2 \pm 0.1)$ MHz and single-photon optomechanical coupling $g_0 = 2\pi \times (734 \pm 31)$ kHz. The electromechanical mode is characterized using microwave reflection measurements at the IDT. We obtain a fit to an equivalent circuit model including a resonance at 4.709 GHz with total loss rate $\gamma_\mathrm{e} = (24.6 \pm 0.5)$ MHz and external coupling rate to a $50\,\Omega$ transmission line $\gamma_{\mathrm{e},e} = (310 \pm 10)$ kHz. The remaining model parameter is the coupling rate $G_{me}$ between the nanobeam mechanical resonance and the membrane electromechanical resonance. This is not directly accessible; our model uses the simulated value of $G_{me} = 2\pi \times 1.15$ MHz.

### 5.3.1 Continuous-wave operation

We characterize the bidirectional conversion efficiency using a continuous pump and signal. For microwave-to-optical transduction, we drive the IDT with a microwave signal swept across the device's operating frequency, and we detect the beat in transmitted optical power using a fast photodiode. At low pump powers we can sweep the laser wavelength across the optical resonance, observing symmetric transduction for red and blue detuning in agreement with theory (Fig. 5.2), with a 3 dB bandwidth of 8.1 MHz.

The signal pathway is calibrated to convert this measurement into a peak "external" photon number efficiency $\eta_\mathrm{ext}$, defined as the ratio between the average output optical

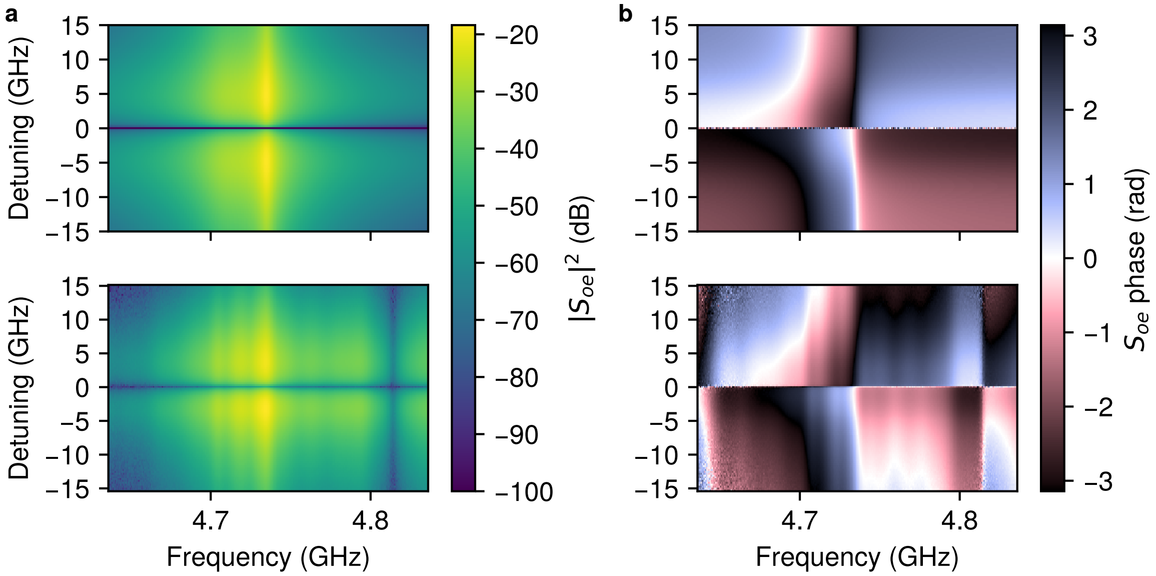

Figure 5.2: **Low-power microwave-to-optical transduction.** Top: theory, using independently fit parameters. Bottom: experiment. **a,** Amplitude. **b,** Phase.

photon rate in the resonant sideband and the average input microwave photon rate, where the output refers the optical fiber above the chip, and the input refers to the microwave cable before the chip. The resulting $\eta_{\text{ext}}$ is plotted in Fig. 5.3a as a function of pump power. Power-dependent redshifting of the optical resonance prevents red-detuned operation with a continuous pump at high powers, so $\eta_{\text{ext}}$ is calculated in blue-detuned operation. We achieve a maximum efficiency of $\eta_{\text{ext}} = (2.5 \pm 0.4) \times 10^{-5}$ (on-chip $\eta = (1.0 \pm 0.16) \times 10^{-4}$) with 168 µW in the input waveguide, with a 3 dB bandwidth of 3.4 MHz. (Internal efficiency is discussed in §5.4 below.)

For optical-to-microwave transduction, we create sidebands on the input light using a phase modulator driven at the device's operating frequency, and we detect microwave power coupled out by the IDT. External photon number efficiency $\eta_{\text{ext}}$ is calculated as

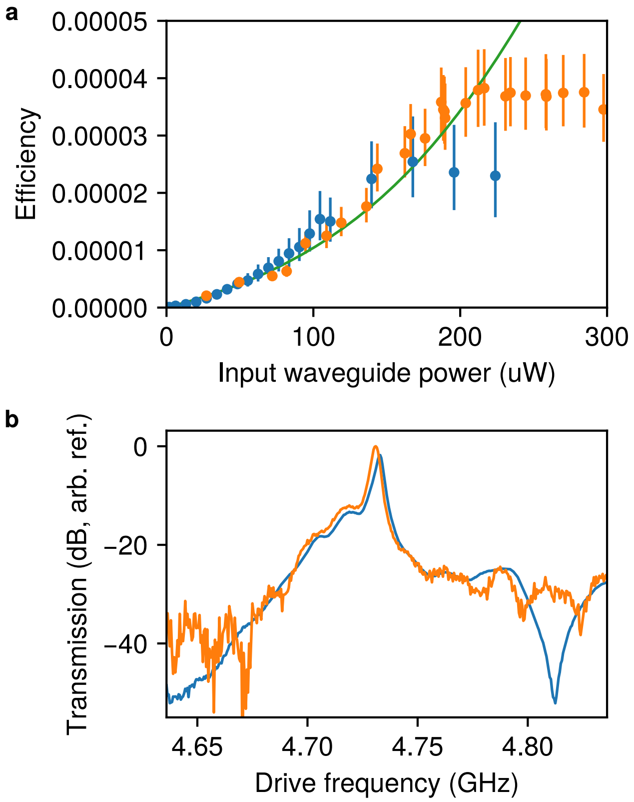

Figure 5.3: **Continuous-wave microwave-to-optical transduction.** **a,** Pump-power dependence of measured microwave-to-optical (blue) and optical-to-microwave (orange) external transduction efficiency. Error bars are 90% confidence intervals; green curve is theoretical efficiency using independently determined model parameters. **b,** Microwave-to-optical (blue) and optical-to-microwave (orange) transduction at the optimized pump powers.

the ratio of the photon rate in the microwave output cable to the photon rate in one optical sideband in the fiber above the chip, and is plotted in Fig. 5.3a as a function of pump power. We achieve a maximum of $\eta_{\text{ext}} = (3.8 \pm 0.4) \times 10^{-5}$ (on-chip $\eta = (1.5 \pm 0.16) \times 10^{-4}$) at 231 µW, with a 3 dB bandwidth of 3.8 MHz. The signal-frequency dependent efficiency at the optimal detuning is compared to that of microwave-to-optical transduction in Fig. 5.3b.

The relative uncertainty is smaller than for the microwave-to-optical efficiency, which calculation suffers additional potential systematic and random errors mainly through the calibration of the optical detection chain. The optical-to-microwave efficiency as a function of power roughly agrees with both the microwave-to-optical efficiency and our theoretical model, up to a pump power at which the experimental efficiency appears to saturate early. The theoretical model uses the parameters as determined above with no additional fitting.

### 5.3.2 Time-domain operation

In order to perform microwave-to-optical transduction in the time domain, the DC port of an optical intensity modulator (IM) is biased to the maximum extinction point, effectively turning the pump off. The RF port of the IM is then driven by a pulse, generated by amplifying the output of a custom DAC, in order to turn the pump on and off. This produces a 20 ns rectangular pulse with rise and fall times of 5 ns and an on-off ratio of 23 dB in optical pump power. The IDT is driven continuously with a microwave source, and an ADC demodulates the transmitted pulse in optical beat power detected with a fast photodiode. The signal is digitally filtered to remove interference from 10 MHz clock harmonics originating elsewhere in the setup; this spurious signal is small enough to be mostly removed from the microwave-to-optical signal, but limits the reliability of optical-to-microwave measurements in the time domain.

By repeating this measurement for laser wavelengths around the low-power-equilibrium

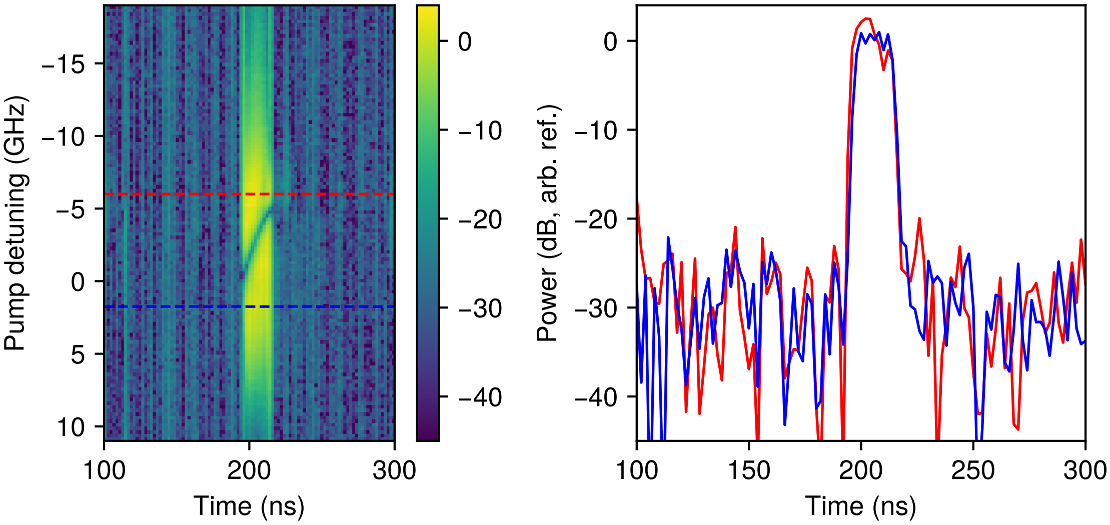

Figure 5.4: **Time-domain microwave-to-optical transduction. Left,** Detected power over time for a range of initial pump detunings. **Right,** Time traces for initially red and blue detuned pulses, using the corresponding dashed cut lines. The maximum input waveguide power during the pulse is 87 µW, with and rise and fall times of 5 ns, and a length of 20 ns between midpoints of the rise and fall.

resonant wavelength (Fig. 5.4), we can observe the time-dependent redshifting of the resonance, marked by the zero in transmission when the pump is resonant and the sidebands interfere destructively. For pump power around 87 µW on the red side of the cavity, the optical mode shifts by roughly 5 GHz in 20 ns. Despite not operating at the optimal detuning for the duration of a 20 ns pulse, we can observe both red-detuned and blue-detuned transduction. By converting the detected signal to a single-sideband photon rate in the fiber after the device, we calculate that approximately $1.6 \times 10^{-6}$ $(1.3 \times 10^{-6})$ of the input microwave photons in 20 ns are transduced when red (blue) detuned. If we considered the blue-detuned continuous-wave efficiency in our model as a function of power and simply integrated that efficiency over the pulse, we would expect a total external efficiency of $8.1 \times 10^{-6}$. The lower efficiency for time-domain operation may be attributed to the time-varying detuning, the finite transduction bandwidth of the device, and operation faster than mechanical amplification by the blue-detuned pump.

Time domain optical-to-microwave transduction can be performed by applying the signal to the phase modulator and demodulating the amplified output of the IDT. An averaged time trace is shown in Fig. 5.5. The measurement suffers from the fact that even a relatively strong optical signal corresponds to a relatively low photon rate, limiting the signal power (or signal-to-noise ratio) available for detection as compared with the microwave-to-optical measurement. Phase information is also transduced in the time domain in both directions (Fig. 5.6).

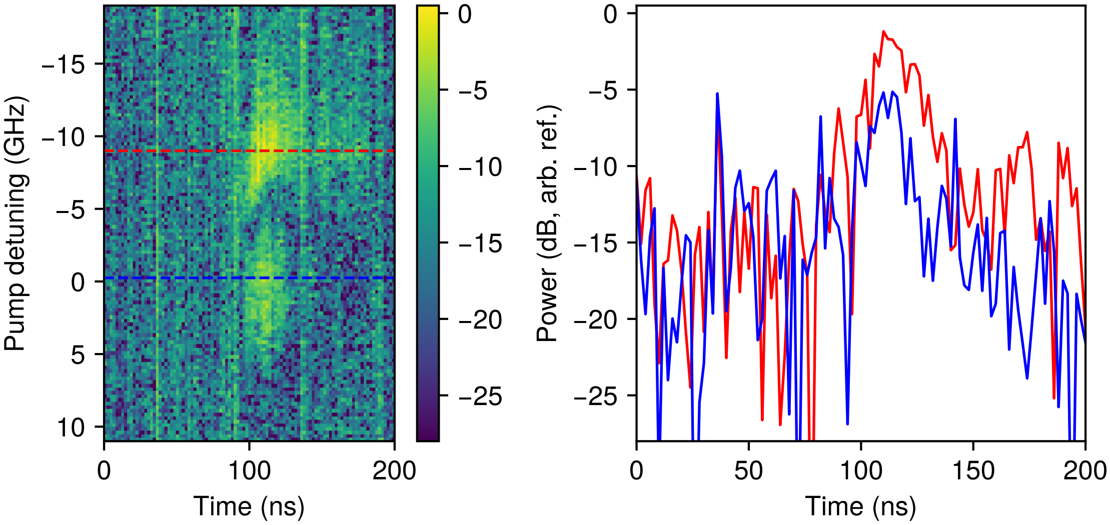

Figure 5.5: **Time-domain optical-to-microwave transduction. Left,** Detected power over time for a range of initial pump detunings. **Right,** Time traces for initially red and blue detuned pulses, using the corresponding dashed cut lines. The maximum input waveguide power during the pulse is 183 µW, with and rise and fall times of 5 ns, and a length of 20 ns between midpoints of the rise and fall.

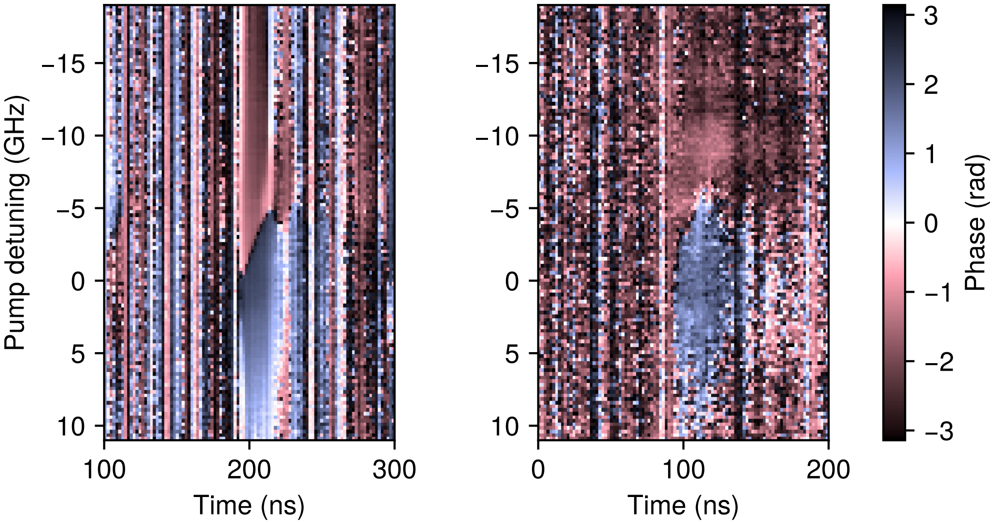

Figure 5.6: **Phase information in time-domain transduction. Left,** Microwave-to-optical phase, corresponding to Figure 5.4. **Right,** Optical-to-microwave phase, corresponding to Figure 5.5.

## 5.4 Internal efficiency

A major factor limiting the external efficiency is the poor impedance matching of the IDT to a $50\,\Omega$ transmission line, which gives a ratio of external coupling to total loss in the electromechanical resonator of $\eta_{\mathrm{e}} = 0.013$. This ratio can be made close to 1 by modifying the impedance seen from the transducer using a lumped-element resonator or impedance matching network [43]. We further note that impedance matching, while relevant in the context of our classical continuous-wave experiment where the electromechanical resonance is addressed by a transmission line, will be replaced by a different challenge when coupled to a resonator or qubit. For example, in order for a qubit to emit its state as a phonon, the electromechanical interaction must be made to dominate other qubit loss pathways.

We can consider a "semi-internal" efficiency that describes the on-chip performance compared to an ideal electrically-overcoupled transducer by factoring out the electrical coupling ratio and the 25% efficiency of the grating couplers. We obtain maximum semi-internal efficiencies of 0.77% and 1.2% for microwave-to-optical and optical-to-microwave transduction, respectively. Since two-sided optical coupling is used for the convenience of measuring in transmission at the cost of a factor of 2 in efficiency, the comparable ideal transducer has an efficiency of 50%. To obtain the internal efficiency as defined in Eqn. 2.45, we also factor out the optical coupling ratio $\eta_{\mathrm{o}} = (\kappa_e/2)/\kappa = 0.32$, yielding $\eta_{\mathrm{int}}$ of 2.4% and 3.75% in the two directions.

# Chapter 6

# Conclusion

In this thesis we have presented the design and operation of a new microwave-optical transducer combining silicon optomechanics with aluminum-nitride based electromechanics. The use of silicon, which has a stronger photoelastic effect than aluminum nitride, together with a detailed revision of the design of the optomechanical and electromechanical elements, has allowed us to demonstrate external conversion efficiencies of $\eta_{\text{ext}} = (2.5 \pm 0.4) \times 10^{-5}$ (microwave to optical) and $\eta_{\text{ext}} = (3.8 \pm 0.4) \times 10^{-5}$ (optical to microwave), corresponding to internal efficiencies above 1%. This device also has a larger bandwidth than previous efficient microwave-optical transducers, allowing us to operate in the time domain as well with 20 ns pulses.

This kind of device could be extended to operate in the quantum regime. Future experiments could focus on cryogenic operation, further improvements to efficiency, and coupling to superconducting qubits.

## 6.1 Improving efficiency

The model of efficiency previously shown in Fig. 2.3 used parameters chosen to be realistic, though among our best measured individual device parameters. With that model, we expect internal efficiency of 0.5 for typical room-temperature mechanical $Q$, approaching unit internal efficiency for mechanical $Q$ achievable at low temperatures. In order to reach these efficiencies in practice, improvements must be made to a number of different aspects of the device, some requiring more engineering effort than others. Examining the optics, one-sided optical coupling would directly recover a factor of 2 in external efficiency, besides allowing operation with lower total $\kappa$. Light could also be coupled to an on-chip waveguide more efficiently than with focusing grating couplers, for example using a lensed tapered fiber as in Ref. [14]. The device used also had an anomalously low optical $Q_i$; we have measured a nanobeam with nominally identical dimensions with optical $Q_i \sim 300,000$ at low temperature ($3\,\mathrm{K}$), as well as devices integrated with the electromechanical element with optical $Q_i \sim 200,000$. This would allow critically coupled (one-sided) operation with a total $\kappa < 2\pi \times 2\,\mathrm{GHz}$, increasing $\mathcal{C}_{\mathrm{om}}$ directly and providing good sideband resolution. The mechanical-electromechanical coupling $G_{\mathrm{me}}$ should be tailored to match cooperativities at the target operating cavity photon number. The frequencies of the electromechanical and mechanical modes can be matched by two-dimensional scaling of one of the geometries, recovering a factor of 5 in efficiency. The electromechanical membrane resonance has a low intrinsic $Q$, possibly owing to the large supports connecting it to the rest of the chip as well as a back mirror defined photolithographically using a direct-write system with a relatively large step size. Patterning the supports with a full-bandgap phononic crystal could reduce clamping losses. The clamping $Q$ of the nanobeam mechanical mode could similarly be improved. Operating at low temperature is also expected to reduce intrinsic mechanical losses.

## 6.2 Outlook

The possibility of quantum operation of an efficient microwave-optical transducer is illuminated by recent work in our lab and others. Optical quantum control of silicon optomechanics has previously been demonstrated, including entanglement of remote mechanical oscillators [47] and light-matter entanglement violating a Bell inequality [37]. If the microwave port of our system can be coupled to a superconducting qubit, that qubit could be read out or excited optically, with the goal of generating an entangled state involving the microwave qubit and a single optical photon. That entanglement would be an essential ingredient for long-distance communication using superconducting qubits.

Recent work on hybrid quantum devices and microwave quantum communication suggests possible paths to interfacing our design with a qubit. An electromechanical resonator was directly coupled to a superconducting qubit on aluminum nitride in Ref. [41], allowing the demonstration of mechanical ground-state cooling and single photon-phonon swaps despite short mechanical and qubit lifetimes. A qubit could be fabricated on the silicon region of the same chip, possibly offering better performance; a silicon-on-insulator qubit was demonstrated in Ref. [29]. A separate qubit chip could also be integrated using a flip-chip method [52]; this method was used to couple surface acoustic waves to qubits in Refs. [53, 7]. Finally, recent work has demonstrated quantum state transfer and entanglement generation between remote superconducting qubits, with methods which could be extended to create a hybrid system with a qubit in a different package at the end of a microwave transmission line in the same refrigerator (for example see Refs. [33, 68]).

Looking beyond the specifics of our device, we hope that the methods of this work may contribute to the wider field of hybrid quantum systems. Surface acoustic waves have emerged as a promising platform for experiments in quantum electromechanics, where Lamb-wave devices may also find a place by eliminating scattering into bulk modes and suppressing clamping losses with complete phononic bandgaps. Optomechanical crystal devices are also a powerful platform for a range of interesting physics, with new possibilities arising from efficient electromechanical driving and detection. Mechanical motion serves as a sort of universal interface between different kinds of systems, from microwaves or optics to semiconductor defect spins, through their sensitivity to physical proximity or microscopic strain of materials. This work has attempted to extend the potential of that interface for whatever applications arise.

# Bibliography

[Citing pages are listed after each reference.]

[1] R. W. Andrews, R. W. Peterson, T. P. Purdy, K. Cicak, R. W. Simmonds, C. A. Regal, and K. W. Lehnert. Bidirectional and efficient conversion between microwave and optical light. *Nature Physics*, 10(4):321–326, April 2014. [Cited on pages 8, 13, and 33.]

[2] Reed W. Andrews. *Quantum signal processing with mechanical oscillators*. PhD thesis, University of Colorado, 2015. [Cited on page 33.]

[3] Markus Aspelmeyer, Tobias J. Kippenberg, and Florian Marquardt. Cavity optomechanics. *Reviews of Modern Physics*, 86(4):1391–1452, December 2014. [Cited on page 14.]

[4] B. A. Auld. *Acoustic Fields and Waves in Solids*, volume 1. Wiley-Interscience, 1973. [Cited on page 63.]

[5] Krishna C. Balram, Marcelo Davanco, Jin Dong Song, and Kartik Srinivasan. Coherent coupling between radio frequency, optical, and acoustic waves in piezo-optomechanical circuits. *Nature Photonics*, 10(5):346–352, May 2016. arXiv: 1508.01486. [Cited on page 9.]

[6] Krishna C. Balram, Marcelo I. Davanco, B. Robert Ilic, Ji-Hoon Kyhm, Jin Dong Song, and Kartik Srinivasan. Acousto-optic and opto-acoustic modulation in piezo-optomechanical circuits. *Physical Review Applied*, 7(2), February 2017. arXiv: 1609.09128. [Cited on page 9.]

[7] A. Bienfait, K. J. Satzinger, Y. P. Zhong, H.-S. Chang, M.-H. Chou, C. R. Conner, É Dumur, J. Grebel, G. A. Peairs, R. G. Povey, and A. N. Cleland. Phonon-mediated quantum state transfer and remote qubit entanglement. *Science*, 364(6438):368–371, April 2019. arXiv: 1903.05672. [Cited on pages 65 and 101.]

[8] Joerg Bochmann, Amit Vainsencher, David D. Awschalom, and Andrew N. Cleland. Nanomechanical coupling between microwave and optical photons. *Nature Physics*, 9(11):712–716, November 2013. [Cited on page 10.]

[9] Seth E. Boeshore. *Aluminum Nitride Thin Films on Titanium: Piezoelectric Transduction on a Metal Substrate*. PhD thesis, University of California, Santa Barbara, 2006. [Cited on page 74.]

[10] H.-J. Briegel, W. Dür, J. I. Cirac, and P. Zoller. Quantum repeaters: The role of imperfect local operations in quantum communication. *Phys. Rev. Lett.*, 81:5932–5935, Dec 1998. [Cited on page 4.]

[11] Jasper Chan. *Laser cooling of an optomechanical crystal resonator to its quantum ground state of motion*. PhD thesis, California Institute of Technology, 2012. [Cited on pages 18 and 19.]

[12] Jasper Chan, Amir H. Safavi-Naeini, Jeff T. Hill, Seán Meenehan, and Oskar Painter. Optimized optomechanical crystal cavity with acoustic radiation shield. *Applied Physics Letters*, 101(8):081115, August 2012. [Cited on page 19.]

[13] A. A. Clerk, M. H. Devoret, S. M. Girvin, Florian Marquardt, and R. J. Schoelkopf. Introduction to quantum noise, measurement, and amplification. *Reviews of Modern Physics*, 82(2):1155–1208, April 2010. [Cited on pages 21 and 36.]

[14] Justin D Cohen. *Fiber-optic integration and efficient detection schemes for optomechanical resonators*. PhD thesis, California Institute of Technology, 2015. [Cited on page 99.]

[15] Supriyo Datta. *Surface Acoustic Wave Devices*. Prentice-Hall, 1986. [Cited on page 65.]

[16] É Dumur, K. J. Satzinger, G. A. Peairs, Ming-Han Chou, A. Bienfait, H.-S. Chang, C. R. Conner, J. Grebel, R. G. Povey, Y. P. Zhong, and A. N. Cleland. Unidirectional Distributed Acoustic Reflection Transducers for Quantum Applications. *Applied Physics Letters*, 114(22):223501, June 2019. arXiv: 1905.03155. [Cited on page 65.]

[17] Benjamin J. Eggleton, Christopher G. Poulton, and Ravi Pant. Inducing and harnessing stimulated Brillouin scattering in photonic integrated circuits. *Advances in Optics and Photonics*, 5(4):536, December 2013. [Cited on page 17.]

[18] Linran Fan, Chang-Ling Zou, Risheng Cheng, Xiang Guo, Xu Han, Zheng Gong, Sihao Wang, and Hong X. Tang. Superconducting cavity electro-optics: A platform for coherent photon conversion between superconducting and photonic circuits. *Science Advances*, 4(8):eaar4994, August 2018. [Cited on page 7.]

[19] Moritz Forsch, Robert Stockill, Andreas Wallucks, Igor Marinkovic, Claus Gärtner, Richard A. Norte, Frank van Otten, Andrea Fiore, Kartik Srinivasan, and Simon Gröblacher. Microwave-to-optics conversion using a mechanical oscillator in its quantum groundstate. *arXiv:1812.07588 [cond-mat, physics:physics, physics:quant-ph]*, December 2018. arXiv: 1812.07588. [Cited on page 9.]

[20] M. L. Gorodetsky, A. Schliesser, G. Anetsberger, S. Deleglise, and T. J. Kippenberg. Determination of the vacuum optomechanical coupling rate using frequency noise calibration. *Optics Express*, 18(22):23236, October 2010. [Cited on page 61.]

[21] M. V. Gustafsson, T. Aref, A. F. Kockum, M. K. Ekstrom, G. Johansson, and P. Delsing. Propagating phonons coupled to an artificial atom. *Science*, 346(6206):207–211, October 2014. [Cited on page 65.]

[22] Ken-ya Hashimoto. *Surface Acoustic Wave Devices in Telecommunications*. Springer, 2000. [Cited on page 65.]

[23] Peter Helnwein. Some remarks on the compressed matrix representation of symmetric second-order and fourth-order tensors. *Computer Methods in Applied Mechanics and Engineering*, 190(22):2753 – 2770, 2001. [Cited on page 19.]

[24] A. P. Higginbotham, P. S. Burns, M. D. Urmey, R. W. Peterson, N. S. Kampel, B. M. Brubaker, G. Smith, K. W. Lehnert, and C. A. Regal. Harnessing electro-optic correlations in an efficient mechanical converter. *Nature Physics*, 14(10):1038–1042, October 2018. [Cited on pages 8, 13, 33, and 38.]

[25] R Hill. The elastic behaviour of a crystalline aggregate. *Proceedings of the Physical Society. Section A*, 65(5):349–354, may 1952. [Cited on page 82.]

[26] Sungkun Hong, Ralf Riedinger, Igor Marinkovic, Andreas Wallucks, Sebastian G. Hofer, Richard A. Norte, Markus Aspelmeyer, and Simon Gröblacher. Hanbury Brown and Twiss interferometry of single phonons from an optomechanical resonator. *Science*, 358(6360):203–206, October 2017. arXiv: 1706.03777. [Cited on page 8.]

[27] John D. Joannopoulos, Steven J. Johnson, Joshua N. Winn, and Robert D. Meade. *Photonic Crystals: Molding the Flow of Light*. Princeton University Press, 2nd edition, 2008. [Cited on pages 18, 41, and 47.]

[28] Steven G. Johnson, M. Ibanescu, M. A. Skorobogatiy, O. Weisberg, J. D. Joannopoulos, and Y. Fink. Perturbation theory for Maxwell's equations with shifting material boundaries. *Physical Review E*, 65(6), June 2002. [Cited on page 18.]

[29] Andrew J. Keller, Paul B. Dieterle, Michael Fang, Brett Berger, Johannes M. Fink, and Oskar Painter. Al transmon qubits on silicon-on-insulator for quantum device integration. *Applied Physics Letters*, 111(4):042603, July 2017. [Cited on page 100.]

[30] H. J. Kimble. The quantum internet. *Nature*, 453:1023, June 2008. [Cited on page 3.]

[31] Horace Lamb. On waves in an elastic plate. *Proceedings of the Royal Society of London. Series A, Containing papers of a mathematical and physical character*, 93(648):114–128, 1917. [Cited on page 65.]

[32] Vincent Laude, Davy Gérard, Naima Khelfaoui, Carlos F. Jerez-Hanckes, Sarah Benchabane, and Abdelkrim Khelif. Subwavelength focusing of surface acoustic waves generated by an annular interdigital transducer. *Applied Physics Letters*, 92(9):094104, March 2008. [Cited on pages 82 and 88.]

[33] N. Leung, Y. Lu, S. Chakram, R. K. Naik, N. Earnest, R. Ma, K. Jacobs, A. N. Cleland, and D. I. Schuster. Deterministic bidirectional communication and remote entanglement generation between superconducting qubits. *npj Quantum Information*, 5(1):18, February 2019. [Cited on pages 3 and 101.]

[34] Vanni Lughi. *Aluminum Nitride Thin Films for MEMS Resonators: Growth and Characterization*. PhD thesis, University of California, Santa Barbara, 2006. [Cited on page 74.]

[35] Gregory S. MacCabe, Hengjiang Ren, Jie Luo, Justin D. Cohen, Hengyun Zhou, Alp Sipahigil, Mohammad Mirhosseini, and Oskar Painter. Phononic bandgap nano-acoustic cavity with ultralong phonon lifetime. *arXiv:1901.04129 [cond-mat, physics:quant-ph]*, January 2019. arXiv: 1901.04129. [Cited on pages 8, 46, and 81.]

[36] R. Manenti, M. J. Peterer, A. Nersisyan, E. B. Magnusson, A. Patterson, and P. J. Leek. Surface acoustic wave resonators in the quantum regime. *Physical Review B*, 93(4), January 2016. [Cited on page 65.]

[37] Igor Marinkovic, Andreas Wallucks, Ralf Riedinger, Sungkun Hong, Markus Aspelmeyer, and Simon Gröblacher. An optomechanical Bell test. *Physical Review Letters*, 121(22), November 2018. arXiv: 1806.10615. [Cited on pages 8 and 100.]

[38] Florian Marquardt, Joe P. Chen, A. A. Clerk, and S. M. Girvin. Quantum Theory of Cavity-Assisted Sideband Cooling of Mechanical Motion. *Physical Review Letters*, 99(9), August 2007. [Cited on page 37.]

[39] David Morgan. *Surface Acoustic Wave Filters*. Elsevier, 2nd edition, 2007. [Cited on pages 65, 70, 71, and 72.]

[40] Sreraman Muralidharan, Jungsang Kim, Norbert Lütkenhaus, Mikhail D. Lukin, and Liang Jiang. Ultrafast and fault-tolerant quantum communication across long distances. *Phys. Rev. Lett.*, 112:250501, Jun 2014. [Cited on page 5.]

[41] A. D. O'Connell, M. Hofheinz, M. Ansmann, Radoslaw C. Bialczak, M. Lenander, Erik Lucero, M. Neeley, D. Sank, H. Wang, M. Weides, J. Wenner, John M. Martinis,

and A. N. Cleland. Quantum ground state and single-phonon control of a mechanical resonator. *Nature*, 464:697, March 2010. [Cited on page 100.]

[42] Rishi N. Patel, Christopher J. Sarabalis, Wentao Jiang, Jeff T. Hill, and Amir H. Safavi-Naeini. Engineering phonon leakage in nanomechanical resonators. *Physical Review Applied*, 8(4), October 2017. arXiv: 1705.07869. [Cited on pages 51 and 53.]

[43] David M. Pozar. *Microwave Engineering*. Wiley, 4th edition, 2012. [Cited on pages 72, 74, and 97.]

[44] Ji-Gang Ren, Ping Xu, Hai-Lin Yong, Liang Zhang, Sheng-Kai Liao, Juan Yin, Wei-Yue Liu, Wen-Qi Cai, Meng Yang, Li Li, Kui-Xing Yang, Xuan Han, Yong-Qiang Yao, Ji Li, Hai-Yan Wu, Song Wan, Lei Liu, Ding-Quan Liu, Yao-Wu Kuang, Zhi-Ping He, Peng Shang, Cheng Guo, Ru-Hua Zheng, Kai Tian, Zhen-Cai Zhu, Nai-Le Liu, Chao-Yang Lu, Rong Shu, Yu-Ao Chen, Cheng-Zhi Peng, Jian-Yu Wang, and Jian-Wei Pan. Ground-to-satellite quantum teleportation. *Nature*, 549:70, August 2017. [Cited on page 4.]

[45] Ralf Riedinger. *Single Phonon Quantum Optics*. PhD thesis, University of Vienna, 2018. [Cited on page 24.]

[46] Ralf Riedinger, Sungkun Hong, Richard A. Norte, Joshua A. Slater, Juying Shang, Alexander G. Krause, Vikas Anant, Markus Aspelmeyer, and Simon Gröblacher. Non-classical correlations between single photons and phonons from a mechanical oscillator. *Nature*, 530(7590):313–316, January 2016. [Cited on page 8.]

[47] Ralf Riedinger, Andreas Wallucks, Igor Marinkovic, Clemens Löschnauer, Markus Aspelmeyer, Sungkun Hong, and Simon Gröblacher. Remote quantum entanglement between two micromechanical oscillators. *Nature*, 556(7702):473–477, April 2018. arXiv: 1710.11147. [Cited on pages 8 and 100.]

[48] Amir H. Safavi-Naeini, Thiago P. Mayer Alegre, Jasper Chan, Matt Eichenfield, Martin Winger, Qiang Lin, Jeffrey T. Hill, Darrick Chang, and Oskar Painter. Electromagnetically Induced Transparency and Slow Light with Optomechanics. *Nature*, 472(7341):69–73, April 2011. arXiv: 1012.1934. [Cited on page 23.]

[49] Amir H. Safavi-Naeini, Simon Gröblacher, Jeff T. Hill, Jasper Chan, Markus Aspelmeyer, and Oskar Painter. Squeezed light from a silicon micromechanical resonator. *Nature*, 500(7461):185–189, August 2013. [Cited on page 38.]

[50] Amir H. Safavi-Naeini and Oskar Painter. Optomechanical Crystal Devices. In Markus Aspelmeyer, Tobias J. Kippenberg, and Florian Marquardt, editors, *Cavity Optomechanics*, pages 195–231. Springer Berlin Heidelberg, Berlin, Heidelberg, 2014. [Cited on pages 8 and 41.]

[51] J.J. Sakurai and J. Napolitano. *Modern Quantum Mechanics*. Cambridge University Press, 2017. [Cited on page 44.]

[52] K. J. Satzinger, C. R. Conner, A. Bienfait, H.-S. Chang, Ming-Han Chou, A. Y. Cleland, É. Dumur, J. Grebel, G. A. Peairs, R. G. Povey, S. J. Whiteley, Y. P. Zhong, D. D. Awschalom, D. I. Schuster, and A. N. Cleland. Simple non-galvanic flip-chip integration method for hybrid quantum systems. *Applied Physics Letters*, 114(17):173501, April 2019. [Cited on page 101.]

[53] K. J. Satzinger, Y. P. Zhong, H.-S. Chang, G. A. Peairs, A. Bienfait, Ming-Han Chou, A. Y. Cleland, C. R. Conner, E. Dumur, J. Grebel, I. Gutierrez, B. H. November, R. G. Povey, S. J. Whiteley, D. D. Awschalom, D. I. Schuster, and A. N. Cleland. Quantum control of surface acoustic wave phonons. *Nature*, 563(7733):661–665, November 2018. arXiv: 1804.07308. [Cited on pages 65 and 101.]

[54] L. R. Sletten, B. A. Moores, J. J. Viennot, and K. W. Lehnert. Resolving Phonon Fock States in a Multimode Cavity with a Double-Slit Qubit. *Physical Review X*, 9(2), June 2019. [Cited on page 65.]

[55] Xiankai Sun, Xufeng Zhang, Carsten Schuck, and Hong X. Tang. Nonlinear optical effects of ultrahigh-Q silicon photonic nanocavities immersed in superfluid helium. *Scientific Reports*, 3(1), December 2013. [Cited on page 7.]

[56] Hiroki Takesue, Shellee D. Dyer, Martin J. Stevens, Varun Verma, Richard P. Mirin, and Sae Woo Nam. Quantum teleportation over 100 km of fiber using highly efficient superconducting nanowire single-photon detectors. *Optica*, 2(10):832–835, Oct 2015. [Cited on page 4.]

[57] Amit Vainsencher, K. J. Satzinger, G. A. Peairs, and A. N. Cleland. Bi-directional conversion between microwave and optical frequencies in a piezoelectric optomechanical device. *Applied Physics Letters*, 109(3):033107, July 2016. [Cited on pages 10, 11, 80, and 81.]

[58] Amit S. Vainsencher. *Building an Optomechanical Interface for Superconducting Qubits*. PhD thesis, University of California, Santa Barbara, 2016. [Cited on page 51.]

[59] Raphaël Van Laer, Roel Baets, and Dries Van Thourhout. Unifying Brillouin scattering and cavity optomechanics. *Physical Review A*, 93(5), May 2016. arXiv: 1503.03044. [Cited on page 18.]

[60] Ying-Dan Wang and Aashish A Clerk. Using dark modes for high-fidelity optomechanical quantum state transfer. *New Journal of Physics*, 14(10):105010, October 2012. [Cited on page 14.]

[61] Ying-Dan Wang and Aashish A. Clerk. Using Interference for High Fidelity Quantum State Transfer in Optomechanics. *Physical Review Letters*, 108(15), April 2012. [Cited on page 14.]

[62] G Wendin. Quantum information processing with superconducting circuits: a review. *Reports on Progress in Physics*, 80(10):106001, sep 2017. [Cited on pages 2 and 9.]

[63] Gustavo S Wiederhecker, Paulo Dainese, and Thiago P Mayer Alegre. Brillouin optomechanics in nanophotonic structures. *APL Photonics*, page 30, 2019. [Cited on page 18.]

[64] I. Wilson-Rae, N. Nooshi, W. Zwerger, and T. J. Kippenberg. Theory of Ground State Cooling of a Mechanical Oscillator Using Dynamical Backaction. *Physical Review Letters*, 99(9), August 2007. [Cited on page 37.]

[65] W. K. Wootters and W. H. Zurek. A single quantum cannot be cloned. *Nature*, 299(5886):802–803, October 1982. [Cited on page 4.]

[66] Marcelo Wu, Emil Zeuthen, Krishna Coimbatore Balram, and Kartik Srinivasan. Microwave-to-optical transduction using coupled piezoelectric and optomechanical resonators. *arXiv:1907.04830 [cond-mat, physics:physics, physics:quant-ph]*, July 2019. arXiv: 1907.04830. [Cited on page 13.]

[67] Amnon Yariv and Pochi Yeh. *Optical Waves in Crystals*. Wiley-Interscience, 1984. [Cited on page 19.]

[68] Y. P. Zhong, H.-S. Chang, K. J. Satzinger, M.-H. Chou, A. Bienfait, C. R. Conner, É. Dumur, J. Grebel, G. A. Peairs, R. G. Povey, D. I. Schuster, and A. N. Cleland. Violating Bell's inequality with remotely connected superconducting qubits. *Nature Physics*, 15(8):741–744, August 2019. [Cited on pages 3 and 101.]